Pathogenic mutations in the chromokinesin KIF22 disrupt anaphase chromosome segregation

Alex F. Thompson[1], Patrick R. Blackburn[2,3], Noah S. Arons[1], Sarah N. Stevens[1], Dusica Babovic-Vuksanovic[2,4], Jane B. Lian[5], Eric W. Klee[6], Jason K. Stumpff[1*]

[1]Molecular Physiology and Biophysics, University of Vermont, Burlington, VT
[2]Laboratory Medicine and Pathology, Mayo Clinic, Rochester, MN
[3]Pathology, St. Jude Children's Research Hospital, Memphis, TN
[4]Clinical Genomics, Mayo Clinic, Rochester, MN
[5]Biochemistry, University of Vermont, Burlington, VT
[6]Biomedical Informatics, Mayo Clinic, Rochester, MN
*Corresponding author, jason.stumpff@uvm.edu

ABSTRACT

The chromokinesin KIF22 generates forces that contribute to mitotic chromosome congression and alignment. Mutations in the α2 helix of the motor domain of KIF22 have been identified in patients with abnormal skeletal development, and we report the identification of a patient with a novel mutation in the KIF22 tail. We demonstrate that pathogenic mutations do not result in a loss of KIF22's functions in early mitosis. Instead, mutations disrupt chromosome segregation in anaphase, resulting in reduced proliferation, abnormal daughter cell nuclear morphology, and, in a subset of cells, cytokinesis failure. This phenotype could be explained by a failure of KIF22 to inactivate in anaphase. Consistent with this model, constitutive activation of the motor via a known site of phosphoregulation in the tail phenocopied the effects of pathogenic mutations. These results suggest the motor domain α2 helix may be an important site for regulation of KIF22 activity at the metaphase to anaphase transition. In support of this conclusion, mimicking phosphorylation of α2 helix residue T158 also prevents inactivation of KIF22 in anaphase. These findings demonstrate the importance of both the head and tail of the motor in regulating the activity of KIF22 and offer insight into the cellular consequences of preventing KIF22 inactivation and disrupting force balance in anaphase.

INTRODUCTION

Mitosis requires mechanisms that mechanically control chromosome movements to ensure equal segregation of chromosomes to daughter cells. Forces that move mitotic chromosomes are generated by microtubule dynamics within the mitotic spindle and by molecular motor proteins. The chromokinesin KIF22 (or Kid, kinesin-like DNA-binding protein) is a plus-end directed member of the kinesin-10 family (Yajima et al., 2003). KIF22 and its orthologs, including

39 Nod (*Drosophila melanogaster*) (Zhang, Knowles, Goldstein, & Hawley, 1990) and Xkid (*Xenopus*
40 *laevis*) (Antonio et al., 2000; Funabiki & Murray, 2000; Takagi, Itabashi, Suzuki, & Ishiwata, 2013),
41 generate forces that move chromosomes away from the spindle poles. Structurally, KIF22
42 contains a conserved kinesin motor domain responsible for ATP hydrolysis and microtubule
43 binding (Tokai et al., 1996; Yajima et al., 2003), a second microtubule binding domain in the tail
44 (Shiroguchi, Ohsugi, Edamatsu, Yamamoto, & Toyoshima, 2003), a predicted coiled-coil domain
45 (Shiroguchi et al., 2003), and a C-terminal DNA binding domain, which includes a helix-hairpin-
46 helix motif (Tokai et al., 1996) **(Figure 1A)**. Precisely how KIF22's force generating activity is
47 regulated in mitotic cells and how this regulation contributes to spindle function and cell viability
48 remain incompletely understood.

49 In interphase, KIF22 localizes to the nucleus (Levesque & Compton, 2001; Tokai et al.,
50 1996). As cells enter mitosis, chromosomes condense and KIF22 binds along chromosome arms
51 (Levesque & Compton, 2001; Tokai et al., 1996). In prometaphase, chromosomes must congress
52 and align at the center of the spindle. The interactions of the KIF22 motor domain with spindle
53 microtubules and the KIF22 tail with chromosome arms allows the motor to generate polar
54 ejection forces (Bieling, Kronja, & Surrey, 2010; Brouhard & Hunt, 2005), which push the arms of
55 chromosomes away from the spindle poles and towards the center of the spindle (Marshall,
56 Marko, Agard, & Sedat, 2001; Rieder & Salmon, 1994; Rieder, Davison, Jensen, Cassimeris, &
57 Salmon, 1986), contributing to chromosome congression in prometaphase (Iemura & Tanaka,
58 2015; Levesque & Compton, 2001; Wandke et al., 2012), as well as chromosome arm orientation
59 (Levesque & Compton, 2001; Wandke et al., 2012). In metaphase, polar ejection forces also
60 contribute to chromosome oscillation and alignment (Antonio et al., 2000; Funabiki & Murray,
61 2000; Levesque & Compton, 2001; Levesque, Howard, Gordon, & Compton, 2003; Stumpff,
62 Wagenbach, Franck, Asbury, & Wordeman, 2012; Takagi et al., 2013; Tokai-Nishizumi, Ohsugi,
63 Suzuki, & Yamamoto, 2005). Purified KIF22 is monomeric (Shiroguchi et al., 2003; Yajima et al.,
64 2003), and the forces generated by KIF22 on chromosomes arms may represent the collective
65 action of many monomers. In anaphase, KIF22 is inactivated to reduce polar ejection forces and
66 allow chromosomes to segregate towards the spindle poles (Soeda, Yamada-Nomoto, & Ohsugi,
67 2016; Su et al., 2016; Wolf, Wandke, Isenberg, & Geley, 2006)

68 The generation of polar ejection forces by KIF22 is regulated by the activity of cyclin-
69 dependent kinase 1 (CDK1)/cyclin B, which is high in prometa- and metaphase, and drops sharply
70 at the metaphase to anaphase transition when cyclin B is degraded (Hershko, 1999; Morgan,
71 1995). KIF22 is phosphorylated by CDK1/cyclin B at T463, a residue in the tail of the motor
72 between the second microtubule binding and coiled-coil domains. Phosphorylation of T463 is

73 required for polar ejection force generation in prometa- and metaphase, and dephosphorylation
74 of T463 is necessary for the suspension of polar ejection forces to allow chromosome segregation
75 in anaphase (Soeda et al., 2016). Although a reduction of polar ejection forces in anaphase is a
76 necessary step for proper anaphase chromosome segregation, it is not clear how this contributes
77 to a shift in force balance within the spindle at the metaphase to anaphase transition. Furthermore,
78 while several regions of the KIF22 tail are known to contribute to KIF22's inactivation as cells
79 transition to anaphase, how motor activity is downregulated has not been resolved.
80 Phosphoproteomic studies have identified sites of phosphorylation within KIF22's α2 helix
81 (Kettenbach et al., 2011; Olsen et al., 2010; Rigbolt et al., 2011), suggesting this region, in addition
82 to the tail, may also be important for the regulation of motor activity.

83 The study of pathogenic mutations can often provide insight into the regulation and
84 function of cellular proteins. Mutations in KIF22 cause the developmental disorder
85 spondyloepimetaphyseal dysplasia with joint laxity, leptodactylic type (SEMDJL2, also referred to
86 as Hall Type or lepto-SEMDJL) (Boyden et al., 2011; Min et al., 2011; Tüysüz, Yılmaz, Erener-
87 Ercan, Bilguvar, & Günel, 2014). Four point mutations in two amino acids have been reported in
88 SEMDJL2 patients (Boyden et al., 2011; Min et al., 2011; Tüysüz et al., 2014) **(Figure 1A)**. These
89 mutations occur in adjacent residues P148 and R149 in the α2 helix of the KIF22 motor domain
90 **(Figure 1B)**. P148 and R149 are conserved in kinesin-10 family members across species **(Figure**
91 **1C)** and in many human members of the kinesin superfamily **(Figure 1D)**. However, no
92 pathogenic mutations in the homologous proline or arginine residues have been recorded in
93 OMIM (Online Mendelian Inheritance in Man, https://omim.org/). All identified patients are
94 heterozygous for a single mutation in KIF22. Mutations in KIF22 dominantly cause SEMDJL2,
95 and patients with both *de novo* and inherited mutations have been identified (Boyden et al., 2011;
96 Min et al., 2011).

97 Although KIF22 mRNA is expressed throughout the body (Human Protein Atlas,
98 http://www.proteinatlas.org (Uhlen et al., 2015)), the effects of these mutations are largely tissue-
99 specific, and the development of the skeletal system is most affected in SEMDJL2 patients. A
100 primary symptom of SEMDJL2 is short stature, resulting from shortening of both the trunk and the
101 limbs. Additionally, patients presented with joint laxity, midface hypoplasia, scoliosis, and
102 leptodactyly, a narrowing of the fingers (Boyden et al., 2011; Min et al., 2011). In very young
103 children with SEMDJL2, the softness of the cartilage in the larynx and trachea caused respiratory
104 issues (Boyden et al., 2011). Growth plate radiology demonstrated delayed maturation of the
105 metaphyses and epiphyses in SEMDJL2 patients, and symptoms became more pronounced as

106 patients aged (Tüysüz et al., 2014). Leptodactyly, specifically, was only observed in older (young
107 adult) patients (Boyden et al., 2011).
108 Pathogenic mutations in the KIF22 motor domain were predicted to be loss of function
109 mutations (Min et al., 2011). However, KIF22 knockout in mice did not affect skeletal
110 development. Loss of KIF22 was lethal early in embryogenesis for approximately 50% of
111 embryos, but mice that survived past this point developed to adulthood and demonstrated no
112 gross abnormalities or pathologies (Ohsugi et al., 2003). As such, the cellular mechanism by
113 which mutations in KIF22 affect development is unknown.
114 Here we characterize an additional patient with a mutation in KIF22 and assess the effect
115 of previously reported and novel pathogenic mutations on the function of KIF22 in mitosis. We
116 demonstrate that mutations are not loss of function mutations, and do not alter the localization of
117 the motor or the generation of polar ejection forces in prometaphase. Instead, mutations disrupt
118 anaphase chromosome segregation, consistent with continued KIF22 activation and consequent
119 polar ejection force generation in anaphase. Defects in anaphase chromosome segregation affect
120 daughter cell nuclear morphology and, in a subset of cells, prevent cytokinesis. These findings
121 demonstrate that anaphase inactivation of KIF22 is critical for daughter cell fitness. As such,
122 mitotic defects may contribute to pathogenesis in patients with KIF22 mutations. Additionally, we
123 demonstrate that aberrant polar ejection force generation in anaphase primarily affects the
124 segregation of chromosomes by limiting chromosome arm movements in anaphase A and spindle
125 pole separation in anaphase B, offering insight into the balance of forces required for accurate
126 chromosome segregation in anaphase. Finally, we demonstrate that mimicking phosphorylation
127 of T158 in the α2 helix disrupts anaphase chromosome segregation, confirming that the region of
128 the motor domain affected by SEMDJL2 mutations also contributes to the mechanism by which
129 KIF22 is inactivated in anaphase.
130
131 **RESULTS**
132 **A novel mutation in KIF22 affects development**
133 We report the identification and characterization of a patient with a novel mutation in KIF22
134 **(Figure 1E)**. The patient is a 15-year-old male with a history of short stature, cryptorchidism and
135 shawl scrotum, minimal scoliosis, secondary enuresis, and skin hyperpigmentation. He presented
136 for evaluation at 9 years of age. At that time, his height was just below 3% for age, weight was at
137 40% for age, and BMI was 82% for age. He was noted to have relative macrocephaly, with a head
138 circumference at 93% for age. He had a broad forehead and hypertelorism, round face, flaring of
139 eyebrows, and ankyloglossia. He also had mild brachydactyly **(Figure 1F)**. He had a history of

140 short stature since infancy, but followed a trajectory close to the third percentile. Growth hormone
141 and thyroid function were normal. Bone age showed a normal, age-appropriate bone maturation
142 with normal epiphyseal ossification centers. However, skeletal survey at age 11 years disclosed
143 mild foreshortening of both 4th metacarpals **(Figure 1F)**, mild scoliosis of 14 degrees, as well as
144 mild increase of the central anteroposterior diameter of several lower thoracic vertebrae with mild
145 "bullet-shaped" appearance, and mild posterior scalloping of the lumbar vertebrae **(Figure 1G)**.
146 Genetic testing was performed to determine the cause of these developmental
147 differences. Clinical whole exome sequencing revealed two variants of uncertain significance: a
148 maternally inherited heterozygous *SLC26A2* variant [NM_000112.3(SLC26A2): c.1046T>A
149 (p.F349Y)] (SCV000782516.1), as well as a *de novo* heterozygous *KIF22* variant
150 [NM_007317.3(KIF22):c.1424T>G (p.V475G)] (SCV000782515.1) **(Figure 1E)**. The *SLC26A2*
151 gene encodes the diastrophic dysplasia sulfate transporter (Haila et al., 2001; Rossi & Superti-
152 Furga, 2001). However, results of carbohydrate deficient transferrin testing were not consistent
153 with a congenital disorder of glycosylation (transferrin tri-sialo/di-oligo ratio 0.07).
154 The c.1424T>G, p.(V475G) *KIF22* variant has not been observed previously in the
155 Genome Aggregation Database (gnomAD). This missense variant has mixed *in silico* predictions
156 of significance **(Supplemental Table 1)**. According to American College of Medical Genetics
157 2015 criteria, the variant was classified as a variant of uncertain significance (VUS). V475 is
158 located in the coiled-coil domain in the tail of KIF22 **(Figure 1A)**. This residue is conserved in
159 most kinesin-10 family members across species **(Figure 1C)**. However, the tail domains of kinesin
160 motors diverge in both structure and function, and as such meaningful alignments to assess the
161 conservation of V475 across the human kinesin superfamily were not possible.

Figure 1

A

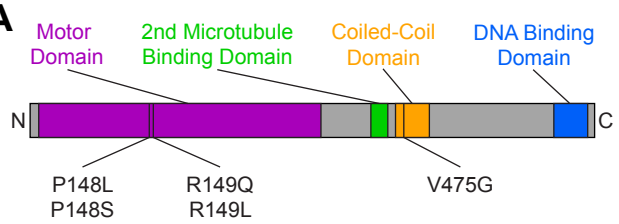

B

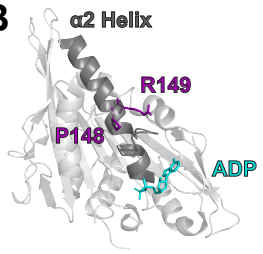

C

Homo sapiens	141	PEQPGVIPRALMDLLQLTREE	161	468	RMVLMKTVEEKDLEI	482
Mus musculus	136	PEQPGVIPRALMDLLQLAREE	156	463	RMVLMKTVEEKNLEI	477
Xenopus laevis	130	PNQPGVIPRAVRDLLQMSRTA	150	450	RMALLKKWEESQMEI	464
Danio rerio	117	QEQPGVIPRAVKEVFNLVGAQ	137	426	RLNLLKTVAQSRKEI	440
Bos taurus	136	PEQPGVIPRALMDLLQLTREE	156	463	RMVLMKTVEEKDLEI	477
Drosophila melanogaster	107	PEHLGILPRALGDIFERVTAR	127	445	NSTLMGIVEETEPK-	459

D

KIF22	141	PEQPGVIPRALMDLLQLTREE	161
KIF5A	122	PQLMGIIPRIARDIFNHIYSM	142
KIF5B	121	PEGMGIIPRIVQDIFNYIYSM	141
KIF5C	122	PQLMGIIPRIAHDIFDHIYSM	142
KIF3A	116	PELRGIIPNSFAHIFGHIAKA	136
KIF3B	112	PEKRGVIPNSFDHIFTHISRS	132
KIF3C	113	PELRGVIPNAFEHIFTHISRS	133
KIF17	107	PSQRGIIPRAFEHVFESVQCA	127
KIF1A	112	KDQQGIIPQLCEDLFSRINDT	132
KIF1B	112	ESQAGIIPQLCEELFEKINDN	132
KIF1C	112	PGQQGIVPQLCEDLFSRVSEN	132
KIF13A	116	-EQLGLIPRLCCALFKRISLE	135
KIF13B	117	-DQPGLIPRLCSGLFERTQKE	136
KIF4B	108	EPTVGIIPRVIQLLFKEIDKK	128
KIF7	114	EDEQGIVPRAMAEAFKLIDEN	135
KIF21A	108	EEELGIISRAVKHLFKSIEEK	128
KIF21B	107	EEEQGIIPRAIAHLFGGIAER	127
KIF11	128	DPLAGIIPRTLHQIFEKLTD-	147
KIF20A	176	--DGGILPRSLALIFNSLQGQ	194
KIF20B	168	--NIGILPRTLNVLFDSLQER	196
KIF23	128	--EGGLLPRCLDMIFNSIGSF	146
KIF10	101	--HLGVIPRAIHDIFQKIKKF	119
KIF18A	125	ADEPGVMYLTMLHLYKCMDEI	145
KIF18B	121	EGDPGIMYLTTVELYRRLEAR	141
KIF19	116	DQEPGIYVQTLNDLFRAIEET	136
KIF6	113	YSDRGIIPRTLSYIFEQLQKD	133
KIF9	109	YKHRGILPRALQQVFRMIEER	129
KIF12	128	PSLAGIMQRTFAWL---LDRV	145
KIF15	130	HNLRGVIPRSFEYLFSLIDRE	130

E

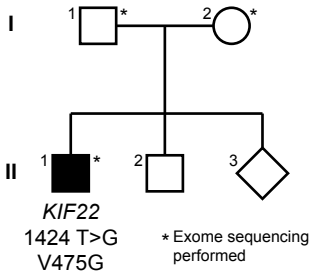

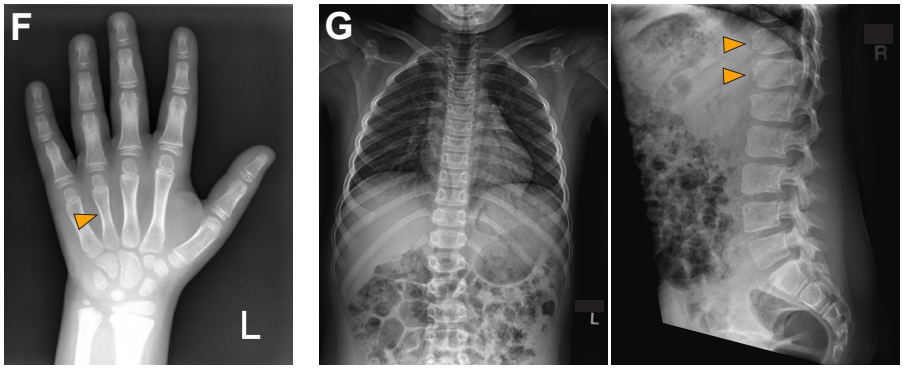

Figure 1. Identification of a novel pathogenic mutation in the tail of KIF22.

(A) Schematic of the domains of KIF22 with pathogenic mutations in the motor domain (magenta) and coiled-coil domain (yellow) indicated. **(B)** Location of amino acids P148 and R149 in the α2 helix of the KIF22 motor domain (PDB 6NJE). **(C)** Alignment of amino acid sequences of kinesin-10 family members to assess conservation of motor domain (P148 and R149, left) and coiled-coil domain (V475G, right) residues across species. **(D)** Alignment of amino acid sequences of human kinesin motors to assess conservation of motor domain residues across the kinesin superfamily. For C and D, alignments were performed using Clustal Omega. **(E)** Pedigree identifying the *de novo* V475G (1424 T>G) mutation. **(F)** Radiograph of the patient's hand, posteroanterior view. Arrowhead indicates mild foreshortening of the 4th metacarpal. **(G)** Radiographs of the patient's spine. Left: anteroposterior view, right: lateral view. Arrowheads indicate "bullet-shaped" lower thoracic vertebrae.

174 **Supplemental Table 1**

Algorithm	Prediction
Sorting Intolerant from Tolerant (SIFT) (Vaser, Adusumalli, Leng, Sikic, & Ng, 2015)	Deleterious: score 0.01 with scores ranging from 0 to 1 and scores below 0.05 considered deleterious
Polymorphism Phenotyping (PolyPhen-2) (Adzhubei et al., 2010)	Benign: score 0.437
MutationTaster (Schwarz, Rödelsperger, Schuelke, & Seelow, 2010)	Deleterious
Combined Annotation Dependent Depletion (CADD) (Rentzsch, Witten, Cooper, Shendure, & Kircher, 2018)	Deleterious: scaled C-score 15.3800, with a score of greater than or equal to 10 indicating a deleterious substitution
Deleterious Annotation of Genetic Variants Using Neural Networks (DANN) (Quang, Chen, & Xie, 2015)	Deleterious: score 0.99 with scores ranging from 0 to 1 and higher values indicating a variant is more likely to be deleterious
Rare Exome Variant Ensemble Learner (REVEL) (Ioannidis et al., 2016)	Benign: score 0.28 with scores ranging from 0 to 1 and scores >0.803 classified as pathogenic

175 **Pathogenic mutations in KIF22 do not disrupt the localization of the motor**

176 To assess the effect of published pathogenic mutations in the motor domain and the novel
177 pathogenic mutation in the tail on the function of KIF22 in mitosis, we generated human cervical
178 adenocarcinoma (HeLa-Kyoto) cell lines with inducible expression of KIF22-GFP. Treatment of
179 these cells with doxycycline induced KIF22-GFP expression at a level approximately two- to three-
180 fold higher than the level of expression of endogenous KIF22 as measured by
181 immunofluorescence **(Figure S1A-C)**. To facilitate both overexpression of and rescue with KIF22-
182 GFP constructs, siRNA-resistant silent mutations were introduced into exogenous KIF22 **(Figure**
183 **S1D-E)**. siRNA knockdown reduced levels of endogenous KIF22 by 87% (mean knockdown
184 efficiency across HeLa-Kyoto cell lines) **(Figure S1D)**. Initial experiments were performed using
185 HeLa-Kyoto cell lines expressing each known pathogenic mutation in KIF22 (P148L, P148S,
186 R149L, R149Q, and V475G), and a subset of experiments then focused on cells expressing one
187 representative motor domain mutation (R149Q) or the coiled-coil domain mutation in the tail
188 (V475G). Additionally, we generated inducible retinal pigmented epithelial (RPE-1) cell lines
189 expressing wild type and mutant KIF22-GFP to assess any differences between the
190 consequences of expressing mutant KIF22 in aneuploid cancer-derived cells (HeLa-Kyoto) and
191 genomically stable somatic cells. RPE-1 cells are human telomerase reverse transcriptase
192 (hTERT)-immortalized (Bodnar et al., 1998), and metaphase chromosome spreads demonstrated
193 that these cell lines are near-diploid, with a modal chromosome number of 46, even after selection
194 to generate stable cell lines **(Figure S1F-G)**. The expression level of siRNA-resistant KIF22-GFP
195 in RPE-1 cell lines was approximately four- to seven-fold higher than the level of expression of
196 endogenous KIF22 **(Figure S1H-K)**, and siRNA knockdown reduced levels of endogenous KIF22
197 by 67% (mean knockdown efficiency across RPE-1 cell lines measured using
198 immunofluorescence). As measurements of KIF22 depletion by immunofluorescence may include
199 non-specific signal, this estimate of knockdown efficiency may underestimate the depletion of
200 KIF22.

201 KIF22 localizes to the nucleus in interphase, and primarily localizes to chromosomes and
202 spindle microtubules during mitosis (Tokai et al., 1996). KIF22-GFP with pathogenic mutations
203 demonstrated the same localization pattern throughout the cell cycle as wild type motor (**Figure**
204 **2A)**. In all cell lines, KIF22-GFP was localized to the nucleus in interphase cells and was bound
205 to condensing chromosomes in prophase. In prometaphase, metaphase, and anaphase mutant
206 and wild type KIF22-GFP localized primarily to chromosome arms, with a smaller amount of motor
207 signal visible on the spindle microtubules. The same localization patterns were seen for mutant
208 and wild type KIF22-GFP expressed in RPE-1 cells **(Figure S2A)**.

209 Since mutations did not grossly disrupt localization of KIF22-GFP, fluorescence recovery
210 after photobleaching (FRAP) was used to compare the dynamics of mutant and wild type KIF22
211 localization. In interphase nuclei, KIF22-GFP signal recovered completely 220 seconds after
212 bleaching (97% ± 3% of intensity before bleaching, mean ± SEM), indicating a dynamic pool of
213 KIF22-GFP **(Figure 2B and S2B)**. Similar high recovery percentages were also measured in
214 interphase nuclei of cells expressing KIF22-GFP R149Q and KIF22-GFP V475G (100% ± 6% and
215 103% ± 7% at 220 seconds, respectively) **(Figure 2E and 2H)**. In contrast, KIF22-GFP recovery
216 was minimal in cells bleached during metaphase and anaphase. Immediately after bleaching
217 KIF22-GFP in metaphase cells, intensity was reduced to 18 ± 3% of initial intensity, and intensity
218 had recovered to only 25% ± 3% after 220 seconds **(Figure 2C and S2B).** In anaphase, KIF22-
219 GFP intensity immediately after bleaching was 17% ± 2% of initial intensity, and intensity
220 recovered to 35% ± 6% of initial intensity after 220 seconds **(Figure 2D and S2B)**. This limited
221 recovery indicates that KIF22 stably associates with mitotic chromosomes. Pathogenic mutations
222 did not change these localization dynamics; recovery percentages in mitosis were also low in cells
223 expressing KIF22-GFP R149Q (32 ± 3% of initial intensity in metaphase 220 seconds after
224 bleaching, 39 ± 6% in anaphase) **(Figure 2F and 2G)** and KIF22-GFP V475G (29 ± 2% of initial
225 intensity in metaphase, 35 ± 6% in anaphase) **(Figure 2I and 2J)**. These data indicate that
226 pathogenic mutations do not alter the localization of KIF22 to chromosomes and spindle
227 microtubules, and do not alter KIF22 localization dynamics in interphase, metaphase, or
228 anaphase.

Supplemental Figure 1

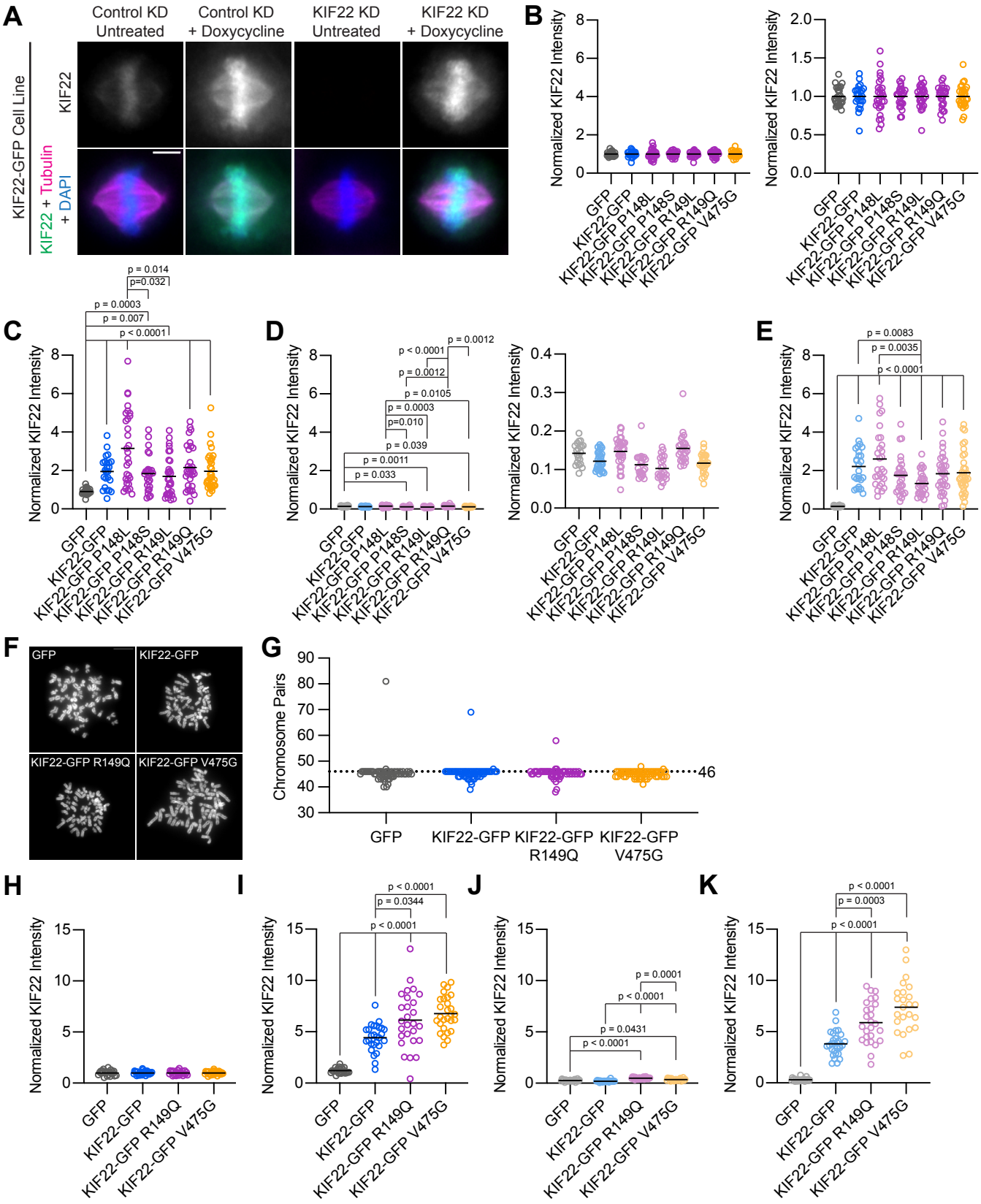

229 **Supplemental Figure 1. HeLa-Kyoto and RPE-1 stable cell lines express mutant KIF22.**
230 **(A**) Immunofluorescence images of HeLa-Kyoto cells expressing KIF22-GFP under the control of
231 a doxycycline inducible promoter. Images are maximum intensity projections in z of five frames
232 at the center of the spindle. Fixed approximately 24 hours after siRNA transfection and treatment
233 with doxycycline to induce expression. Scale bar 5 μm. KD: knockdown. **(B-E)** Quantification of
234 KIF22 fluorescence intensity in untreated HeLa-Kyoto cells transfected with control siRNA (B),
235 cells treated with doxycycline to induce expression and transfected with control siRNA (C),
236 untreated cells transfected with KIF22 siRNA (D), and cells treated with doxycycline and
237 transfected with KIF22 siRNA (E) normalized to the mean intensity of uninduced, control
238 knockdown cells (endogenous KIF22 expression level) for each cell line (B). Data in B and D are
239 presented with the same y-axis scale as data in C and E for comparison (left), and with
240 independently scaled y-axes to show data variability (right). 27 GFP, 24 KIF22-GFP, 27 KIF22-
241 GFP R149Q, 28 KIF22-GFP P148L, 25 KIF22-GFP P148S, 27 KIF22-GFP R149L, and 30 KIF22-
242 GFP V475G untreated cells transfected with control siRNA (B), 24 GFP, 24 KIF22-GFP, 31 KIF22-
243 GFP R149Q, 30 KIF22-GFP P148L, 27 KIF22-GFP P148S, 30 KIF22-GFP R149L, and 33 KIF22-
244 GFP V475G doxycycline-treated cells transfected with control siRNA (C), 21 GFP, 31 KIF22-GFP,
245 27 KIF22-GFP R149Q, 32 KIF22-GFP P148L, 22 KIF22-GFP P148S, 22 KIF22-GFP R149L, and
246 25 KIF22-GFP V475G untreated cells transfected with KIF22 siRNA (D), 26 GFP, 26 KIF22-GFP,
247 32 KIF22-GFP R149Q, 28 KIF22-GFP P148L, 28 KIF22-GFP P148S, 27 KIF22-GFP R149L, and
248 33 KIF22-GFP V475G doxycycline-treated cells transfected with KIF22 siRNA (E) from 3
249 experiments. **(F)** DAPI-stained metaphase chromosome spreads from uninduced RPE-1 cell lines
250 with inducible expression of GFP, KIF22-GFP, KIF22-GFP R149Q, or KIF22-GFP V475G. Scale
251 bar 10 μm. Images are representative of 3 experiments. **(G)** Numbers of chromosome pairs
252 counted in metaphase spreads prepared from RPE-1 stable cell lines. Dashed line indicates the
253 expected chromosome number for diploid human cells (46). The mode for each cell line is 46. 55
254 GFP, 58 KIF22-GFP, 53 KIF22-GFP R149Q, and 57 KIF22-GFP V475G spreads from 3
255 experiments. **(H-K)** Quantification of KIF22 fluorescence intensity in untreated RPE-1 cells
256 transfected with control siRNA (H), cells treated with doxycycline to induce expression and
257 transfected with control siRNA (I), untreated cells transfected with KIF22 siRNA (J), and cells
258 treated with doxycycline and transfected with KIF22 siRNA (K) normalized to the mean intensity
259 of uninduced, control knockdown cells for each cell line (H). 23 GFP, 27 KIF22-GFP, 25 KIF22-
260 GFP R149Q, and 27 KIF22-GFP V475G untreated cells transfected with control siRNA (H), 24
261 GFP, 27 KIF22-GFP, 27 KIF22-GFP R149Q, and 28 KIF22-GFP V475G doxycycline-treated cells
262 transfected with control siRNA (I), 21 GFP, 24 KIF22-GFP, 24 KIF22-GFP R149Q, and 21 KIF22-

263 GFP V475G untreated cells transfected with KIF22 siRNA (J), 24 GFP, 29 KIF22-GFP, 26 KIF22-
264 GFP R149Q, and 24 KIF22-GFP V475G doxycycline-treated cells transfected with KIF22 siRNA
265 (K) from 3 experiments. For B-E and H-K, bars indicate means. p values from Brown-Forsythe
266 and Welch ANOVA with Dunnett's T3 multiple comparisons test. p values are greater than 0.05
267 for comparisons without a marked p value.

Figure 2

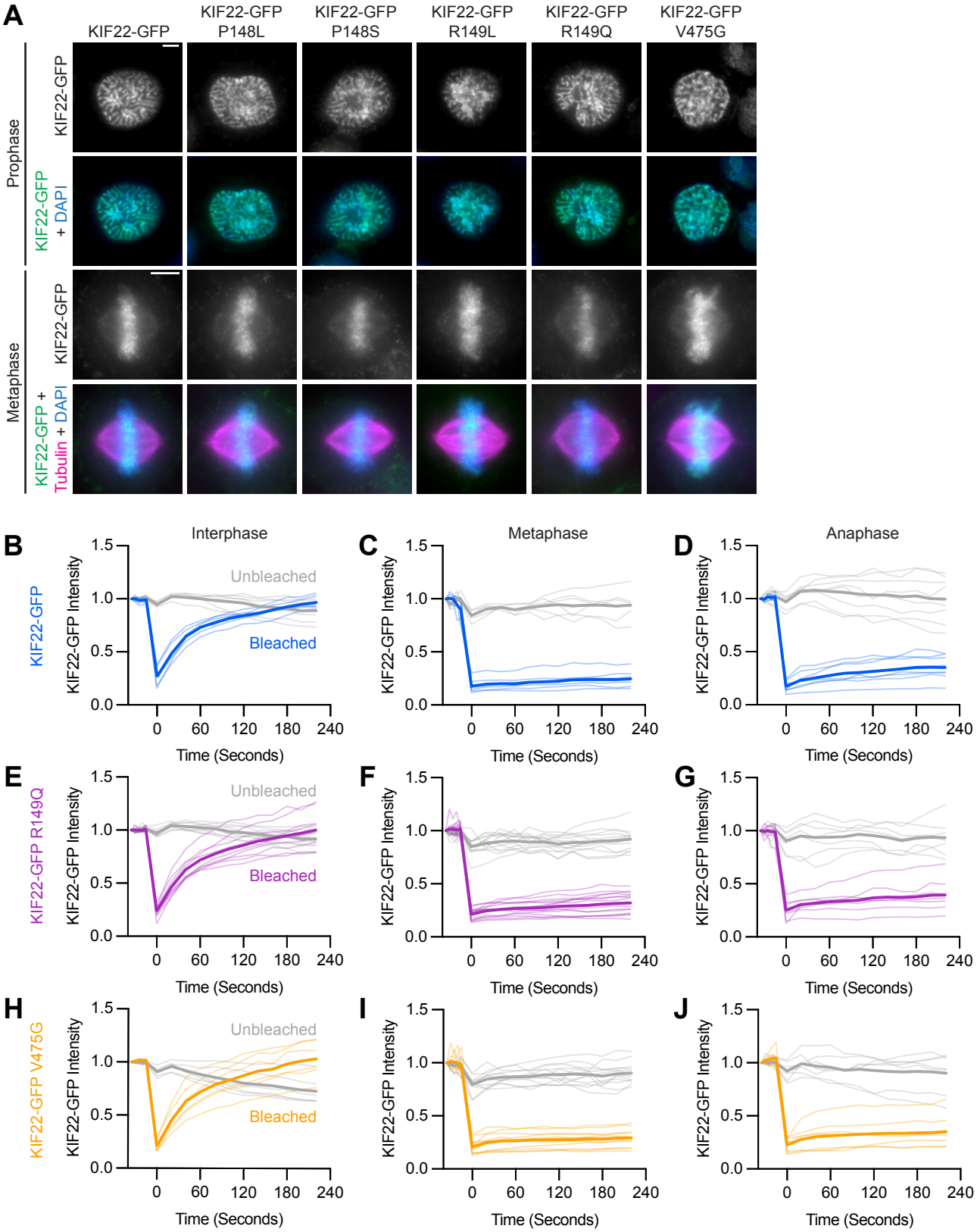
A
KIF22-GFP
KIF22-GFP P148L
KIF22-GFP P148S
KIF22-GFP R149L
KIF22-GFP R149Q
KIF22-GFP V475G
Prophase
Metaphase
KIF22-GFP
KIF22-GFP + DAPI
KIF22-GFP + Tubulin + DAPI
B
C
D
E
F
G
H
I
J
Interphase
Metaphase
Anaphase
KIF22-GFP
KIF22-GFP R149Q
KIF22-GFP V475G
Unbleached
Bleached
KIF22-GFP Intensity
Time (Seconds)
0.0
0.5
1.0
1.5
0
60
120
180
240

268 **Figure 2. Pathogenic mutations in KIF22 do not disrupt the localization of the motor.**
269 **(A)** Immunofluorescence images of HeLa-Kyoto cells expressing KIF22-GFP constructs in
270 prophase (top two rows) and metaphase (bottom two rows). KIF22-GFP was visualized using an
271 anti-GFP antibody. Images are maximum intensity projections in z of five frames at the center of
272 the spindle (metaphase cells) or maximum intensity projections in z of two frames (prophase
273 cells). Fixed approximately 24 hours after treatment with doxycycline to induce expression. Scale
274 bars 5 μm. **(B-J)** Fluorescence recovery after photobleaching (FRAP) of KIF22-GFP (B-D), KIF22-
275 GFP R149Q (E-G), and KIF22-GFP V475G (H-J) in interphase nuclei (B, E, H) or on metaphase
276 (C, F, I) or anaphase (D, G, J) chromosomes. Bleaching occurred at time zero. Thin lines are
277 traces from individual cells and thick lines represent means. Intensity values are normalized to
278 the KIF22-GFP intensity in the first imaged frame before bleaching. Interphase measurements (B,
279 E, H) obtained from 6 KIF22-GFP cells from 4 experiments, 9 KIF22-GFP R149Q cells from 5
280 experiments, and 6 KIF22-GFP V475G cells from 4 experiments. Metaphase measurements (C,
281 F, I) obtained from 6 KIF22-GFP cells from 4 experiments, 14 KIF22-GFP R149Q cells from 5
282 experiments, and 12 KIF22-GFP V475G cells from 4 experiments. Anaphase measurements (D,
283 G, J) obtained from 8 KIF22-GFP cells from 4 experiments, 7 KIF22-GFP R149Q cells from 5
284 experiments, and 7 KIF22-GFP V475G cells from 3 experiments.

Supplemental Figure 2

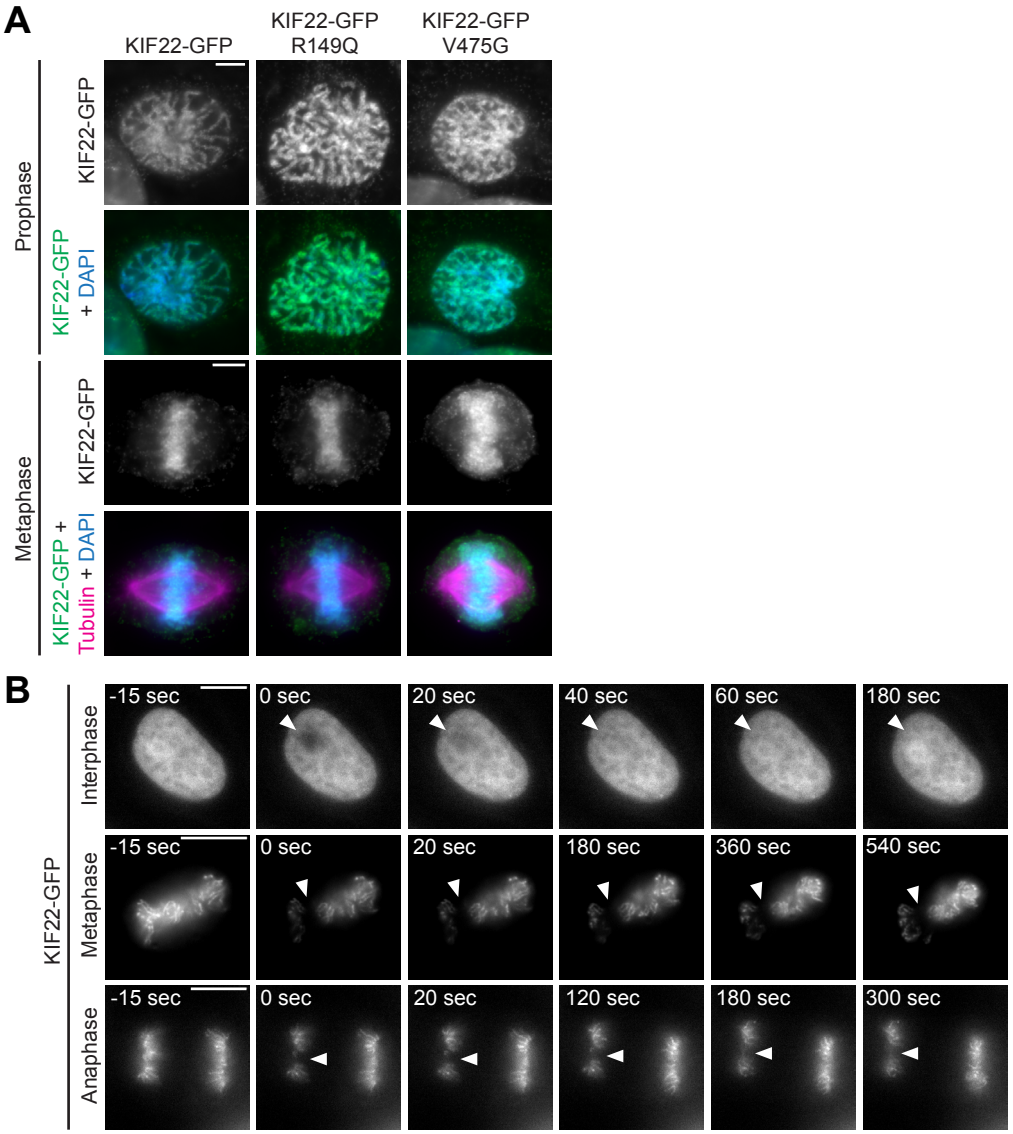

285 **Supplemental Figure 2. Pathogenic mutations in KIF22 do not disrupt the localization of**
286 **the motor in RPE-1 cells.**
287 **(A)** Immunofluorescence images of RPE-1 cells expressing KIF22-GFP constructs in prophase
288 (top two rows) and metaphase (bottom two rows). KIF22-GFP was visualized using an anti-GFP
289 antibody. Images are maximum intensity projections in z of five frames at the center of the spindle
290 (metaphase cells) or maximum intensity projections in z of three frames (prophase cells). Fixed
291 approximately 18 hours after treatment with doxycycline to induce expression. Scale bars 5 μm.
292 **(B)** Time-lapse images of fluorescence recovery after photobleaching (FRAP) in HeLa-Kyoto cells
293 expressing KIF22-GFP. Bleaching occurred at time zero, and arrowheads indicate bleached area.
294 Scale bars 10 μm. Images are representative of 3 or more experiments.

295 **Mutations do not reduce polar ejection forces**

296 In prometaphase and metaphase, KIF22 contributes to chromosome congression and
297 alignment by generating polar ejection forces (Brouhard & Hunt, 2005; Levesque & Compton,
298 2001; Stumpff et al., 2012; Wandke et al., 2012). In cells treated with monastrol to inhibit
299 Eg5/KIF11 and generate monopolar spindles, polar ejection forces push chromosomes away from
300 a single central spindle pole (Levesque & Compton, 2001) **(Figure 3A)**. A loss of KIF22 function
301 causes chromosomes to collapse in towards the pole in this system (Levesque & Compton, 2001)
302 **(Figure 3A)**. To determine whether overexpression of KIF22-GFP with pathogenic mutations has
303 a dominant effect on polar ejection force generation, wild type or mutant KIF22-GFP-expressing
304 HeLa-Kyoto cells were treated with monastrol to induce mitotic arrest with monopolar spindles.
305 Relative polar ejection forces were compared by measuring the distance from the spindle pole to
306 the maximum DAPI signal **(Figure 3A)**. Expression of mutant motor did not reduce polar ejection
307 forces **(Figure 3B and 3C)**. Rather, expression of KIF22-GFP R149L and R149Q significantly
308 increased the distance from the pole to the maximum DAPI signal (R149L 4.6 $\pm$ 0.13 μm, R149Q
309 4.3 $\pm$ 0.11 μm, GFP control 3.7 $\pm$ 0.04 μm, mean $\pm$ SEM), indicating higher levels of polar ejection
310 forces in these cells.

311 The same assay was used to test whether mutant KIF22 could rescue polar ejection force
312 generation in cells depleted of endogenous KIF22. In control cells expressing GFP, depletion of
313 endogenous KIF22 resulted in the collapse of chromosomes towards the pole **(Figure 3B)**, and
314 the distance from the pole to the maximum DAPI signal was reduced to 1.6 $\pm$ 0.11 μm, indicating
315 a loss of polar ejection forces **(Figure 3D)**. This reduction was not observed in cells expressing
316 wild type or mutant KIF22-GFP, demonstrating that KIF22-GFP with pathogenic mutations is
317 capable of generating polar ejection forces **(Figure 3B and 3D)**. In cells transfected with control
318 siRNA and cells depleted of endogenous KIF22, polar ejection force levels did not depend on
319 KIF22-GFP expression levels **(Figure 3E and 3F)**.

320 Together, the localization of mutant KIF22 and the ability of mutant KIF22 to generate
321 polar ejection forces indicate that pathogenic mutations P148L, P148S, R149L, R149Q, and
322 V475G do not result in a loss of KIF22 function during early mitosis.

Figure 3

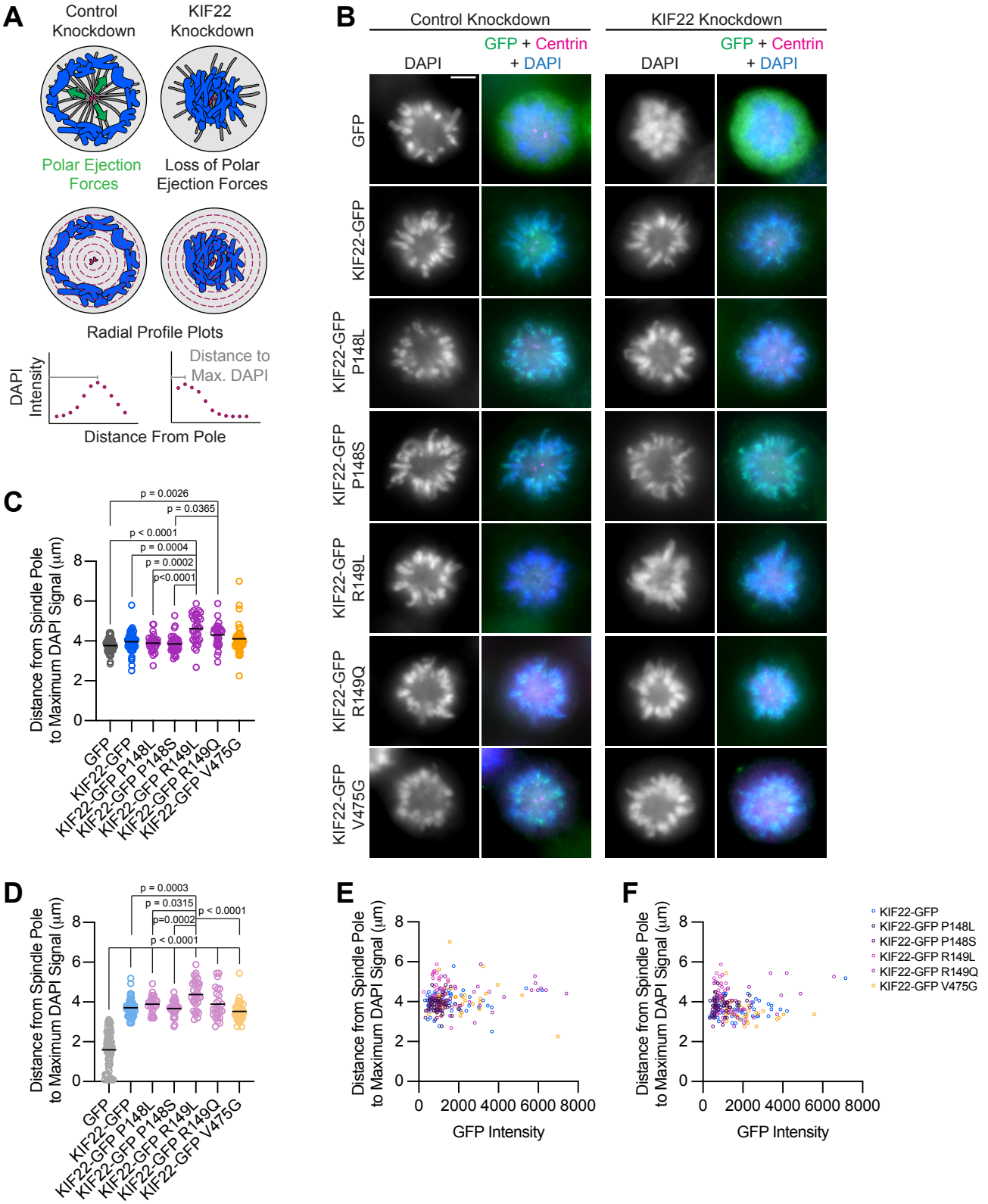
A
Control Knockdown
KIF22 Knockdown
Polar Ejection Forces
Loss of Polar Ejection Forces
Radial Profile Plots
DAPI Intensity
Distance to Max. DAPI
Distance From Pole
B
Control Knockdown
KIF22 Knockdown
DAPI
GFP + Centrin + DAPI
GFP
KIF22-GFP
KIF22-GFP P148L
KIF22-GFP P148S
KIF22-GFP R149L
KIF22-GFP R149Q
KIF22-GFP V475G
C
Distance from Spindle Pole to Maximum DAPI Signal (µm)
p = 0.0026
p = 0.0365
p < 0.0001
p = 0.0004
p = 0.0002
p<0.0001
GFP
KIF22-GFP
KIF22-GFP P148L
KIF22-GFP P148S
KIF22-GFP R149L
KIF22-GFP R149Q
KIF22-GFP V475G
D
Distance from Spindle Pole to Maximum DAPI Signal (µm)
p = 0.0003
p = 0.0315
p=0.0002
p < 0.0001
p < 0.0001
E
Distance from Spindle Pole to Maximum DAPI Signal (µm)
GFP Intensity
F
Distance from Spindle Pole to Maximum DAPI Signal (µm)
GFP Intensity
KIF22-GFP
KIF22-GFP P148L
KIF22-GFP P148S
KIF22-GFP R149L
KIF22-GFP R149Q
KIF22-GFP V475G

323 **Figure 3. Pathogenic mutations in KIF22 do not reduce polar ejection forces.**
324 **(A)** Schematic of changes in chromosome positions resulting from loss of polar ejection forces.
325 In cells with monopolar spindles, both spindle poles (magenta) are positioned together and
326 chromosomes (blue) are pushed toward the cell periphery by polar ejection forces (green) (left).
327 In cells depleted of KIF22, polar ejection forces are reduced and chromosomes collapse in toward
328 the center of the cell (right). Relative polar ejection forces were quantified using radial profile plots
329 to measure the distance from the spindle pole to the maximum DAPI signal intensity. **(B)**
330 Immunofluorescence images of monopolar HeLa-Kyoto cells. KIF22-GFP was visualized using
331 an anti-GFP antibody. Fixed approximately 2-3 hours after treatment with monastrol and 24 hours
332 after siRNA transfection and treatment with doxycycline to induce expression. Scale bar 5 μm.
333 Images are representative of 3 or more experiments. **(C)** Distance from the spindle pole to the
334 maximum DAPI signal, a measure of relative polar ejection force level, in cells transfected with
335 control siRNA. 59 GFP cells from 7 experiments, 69 KIF22-GFP cells from 6 experiments, 31
336 KIF22-GFP P148L cells from 3 experiments, 37 KIF22-GFP P148S cells from 3 experiments, 33
337 KIF22-GFP R149L cells from 3 experiments, 28 KIF22-GFP R149Q cells from 3 experiments, and
338 45 KIF22-GFP V475G cells from 3 experiments. **(D)** Distance from the spindle pole to the
339 maximum DAPI signal in cells transfected with KIF22 siRNA. 75 GFP cells from 7 experiments,
340 57 KIF22-GFP from 6 experiments, 28 KIF22-GFP P148L cells from 3 experiments, 30 KIF22-
341 GFP P148S cells from 3 experiments, 33 KIF22-GFP R149L cells from 3 experiments, 26 KIF22-
342 GFP R149Q cells from 3 experiments, and 34 KIF22-GFP V475G cells. For C-D, bars indicate
343 means. p values from Brown-Forsythe and Welch ANOVA with Dunnett's T3 multiple comparisons
344 test. p values are greater than 0.05 for comparisons without a marked p value. **(E-F)** Background-
345 subtracted GFP intensity plotted against the distance from the spindle pole to the maximum DAPI
346 signal to assess dependence of polar ejection force generation on expression levels in cells
347 transfected with control siRNA (E) (Pearson correlation coefficient 0.105, two-tailed p value
348 0.1031) or KIF22 siRNA (F) (Pearson correlation coefficient -0.005, two-tailed p value 0.9427).

349 **KIF22 mutations disrupt anaphase chromosome segregation**

350 While pathogenic mutations did not disrupt the function of KIF22 in prometa- or
351 metaphase, HeLa-Kyoto cells expressing mutant KIF22-GFP exhibited defects in anaphase
352 chromosome segregation. In these cells, chromosomes did not move persistently towards the
353 spindle poles. Instead, chromosomes began to segregate, but then reversed direction and moved
354 back towards the center of the spindle or remained in the center of the spindle until
355 decondensation **(Figure 4A).** This phenotype was dominant and occurred in the presence of
356 endogenous KIF22. Recongression was quantified by measuring the distance between
357 separating chromosome masses as anaphase progressed. In cells expressing wild type KIF22-
358 GFP, this value increases steadily and then plateaus. Expression of mutant KIF22-GFP causes
359 the distance between chromosome masses to increase, then decrease as chromosomes
360 recongress, and then increase again as segregation continues **(Figure 4B)**. Recongression
361 reduces the distance between chromosome masses 7 minutes after anaphase onset in cells
362 expressing KIF22-GFP with pathogenic mutations (median distance 2.0 – 7.2 μm) compared to
363 cells expressing wild type KIF22-GFP (median distance 12.9 μm) **(Figure 4C)**. Defects in
364 anaphase chromosome segregation were also observed in RPE-1 cells expressing KIF22-GFP
365 R149Q or V475G **(Figure S3D, S3E, S3F)**. This gain of function phenotype is consistent with a
366 lack of KIF22 inactivation in anaphase, resulting in a failure to suspend polar ejection force
367 generation.

368 If recongression is the result of increased KIF22 activity in anaphase, we would predict
369 that increased levels of KIF22-GFP expression would cause more severe anaphase chromosome
370 segregation defects. Indeed, plotting the distance between chromosome masses 7 minutes after
371 anaphase onset against mean GFP intensity for each HeLa-Kyoto cell demonstrated that these
372 two values were correlated (Spearman correlation coefficient -0.6246, one-tailed p value <
373 0.0001) **(Figure S3A)**. Considering only cells expressing lower levels of KIF22-GFP (mean
374 background subtracted intensity <100 arbitrary units) emphasized the differences in the distance
375 between chromosome masses as anaphase progressed between cells expressing wild type and
376 mutant motor **(Figure S3B, S3C)**.

377 In a subset of HeLa-Kyoto cells, expression of KIF22-GFP with pathogenic mutations
378 caused cytokinesis failure **(Figure 4D)**. This result is consistent with the published observation
379 that causing chromosome recongression by preventing cyclin B1 degradation can result in
380 cytokinesis failure (Wolf et al., 2006). In cells expressing KIF22-GFP with pathogenic mutations,
381 cleavage furrow ingression began, but did not complete, resulting in a single daughter cell. The
382 percentage of cells failing to complete cytokinesis was approximately ten-fold higher in cells

383 expressing mutant KIF22-GFP (R149Q 36%, V475G 25%) than in cells expressing wild type
384 KIF22-GFP (3%). Additionally, the distance between chromosome masses at the time of cleavage
385 furrow ingression was reduced in cells expressing KIF22-GFP R149Q or V475G, suggesting that
386 the position of the chromosome masses may be physically obstructing cytokinesis **(Figure 4E)**.
387 Consistent with this hypothesis, cells that failed to complete cytokinesis tended to have lower
388 distances between chromosome masses than the distances measured in cells in which
389 cytokinesis completed despite expression of mutant KIF22-GFP **(Figure 4E)**.

Figure 4

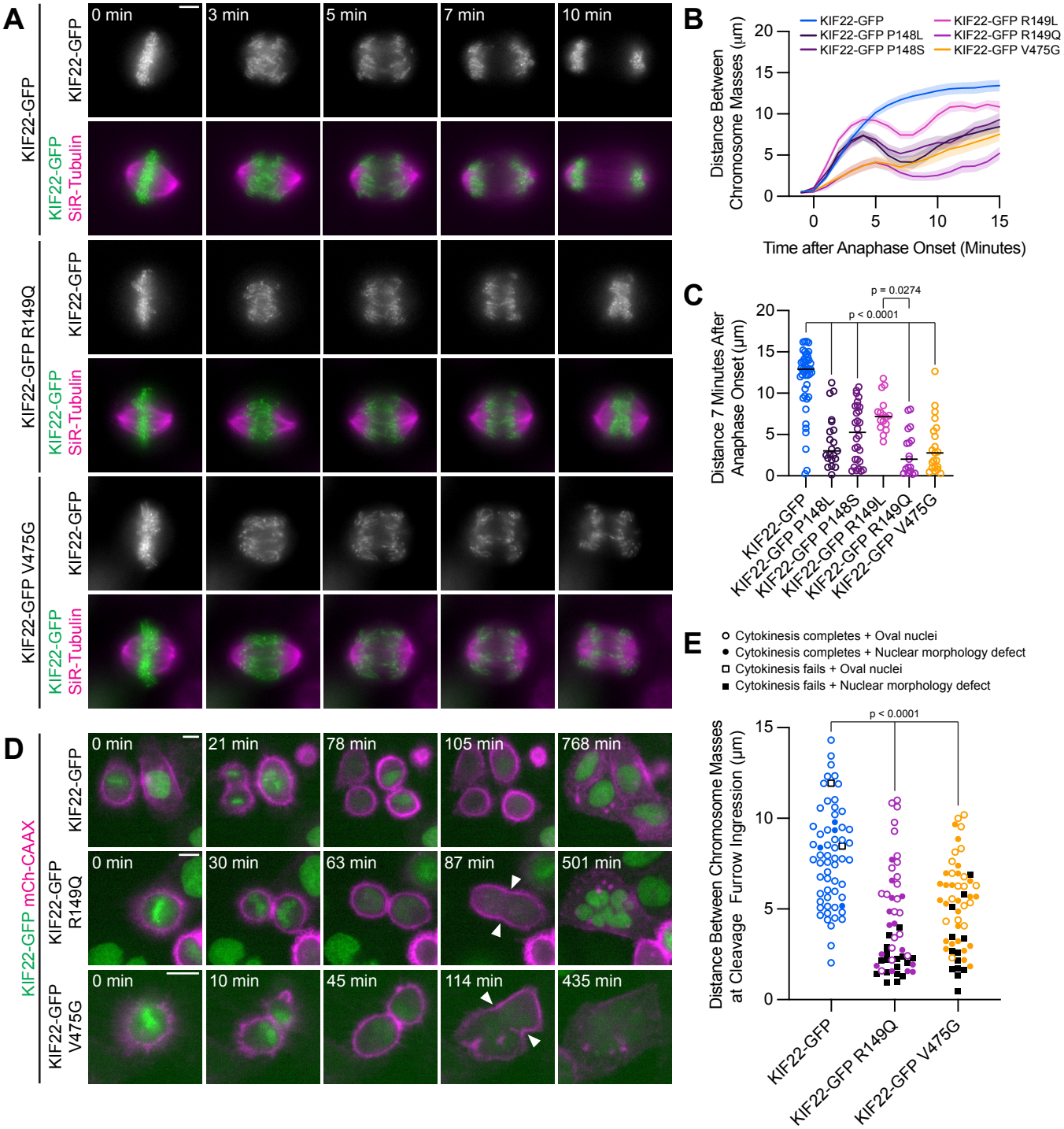
A
KIF22-GFP
KIF22-GFP R149Q
KIF22-GFP V475G
KIF22-GFP
KIF22-GFP
SiR-Tubulin
0 min
3 min
5 min
7 min
10 min
B
KIF22-GFP
KIF22-GFP P148L
KIF22-GFP P148S
KIF22-GFP R149L
KIF22-GFP R149Q
KIF22-GFP V475G
Distance Between Chromosome Masses (µm)
Time after Anaphase Onset (Minutes)
C
p = 0.0274
p < 0.0001
Distance 7 Minutes After Anaphase Onset (µm)
KIF22-GFP
KIF22-GFP P148L
KIF22-GFP P148S
KIF22-GFP R149L
KIF22-GFP R149Q
KIF22-GFP V475G
D
KIF22-GFP mCh-CAAX
KIF22-GFP
KIF22-GFP R149Q
KIF22-GFP V475G
0 min
21 min
78 min
105 min
768 min
30 min
63 min
87 min
501 min
10 min
45 min
114 min
435 min
E
Cytokinesis completes + Oval nuclei
Cytokinesis completes + Nuclear morphology defect
Cytokinesis fails + Oval nuclei
Cytokinesis fails + Nuclear morphology defect
p < 0.0001
Distance Between Chromosome Masses at Cleavage Furrow Ingression (µm)
KIF22-GFP
KIF22-GFP R149Q
KIF22-GFP V475G

390 **Figure 4. Pathogenic mutations in KIF22 disrupt anaphase chromosome segregation.**
391 **(A)** Time-lapse images of dividing HeLa-Kyoto cells expressing KIF22-GFP R149Q or KIF22-GFP
392 V475G. Times indicate minutes after anaphase onset. Images are maximum intensity projections
393 in z through the entirety of the spindle. Imaged approximately 18 hours after treatment with
394 doxycycline to induce expression. Scale bar 5 μm. Images are representative of 3 or more
395 experiments. **(B)** Distance between separating chromosome masses throughout anaphase in
396 HeLa-Kyoto cells. Lines represent the mean and the shaded area denotes SEM. 43 KIF22-GFP
397 cells from 10 experiments, 21 KIF22-GFP P148L cells from 6 experiments, 28 KIF22-GFP P148S
398 cells from 7 experiments, 16 KIF22-GFP R149L cells from 6 experiments, 17 KIF22-GFP R149Q
399 cells from 4 experiments, and 21 KIF22-GFP V475G cells from 21 experiments. **(C)** Distance
400 between separating chromosome masses 7 minutes after anaphase onset. Bars indicate
401 medians. p values from Kruskal-Wallis test. p values are greater than 0.05 for comparisons
402 without a marked p value. Data represent the same cell populations presented in (B). **(D)** Time-
403 lapse images of dividing HeLa-Kyoto cells expressing mCherry (mCh)-CAAX to visualize cell
404 boundaries. Times indicate minutes after anaphase onset. Arrowheads indicate cytokinesis
405 failure. Imaged approximately 8 hours after treatment with doxycycline to induce expression and
406 24-32 hours after transfection with mCh-CAAX. Scale bars 20 μm. Images are representative of
407 3 or more experiments. **(E)** Distance between chromosome masses at the time of cleavage furrow
408 ingression. p values from Kruskal-Wallis test. p values are greater than 0.05 for comparisons
409 without a marked p value. 62 KIF22-GFP cells from 10 experiments, 52 KIF22-GFP R149Q cells
410 from 9 experiments, and 55 KIF22-GFP V475G cells from 9 experiments.

Supplemental Figure 3

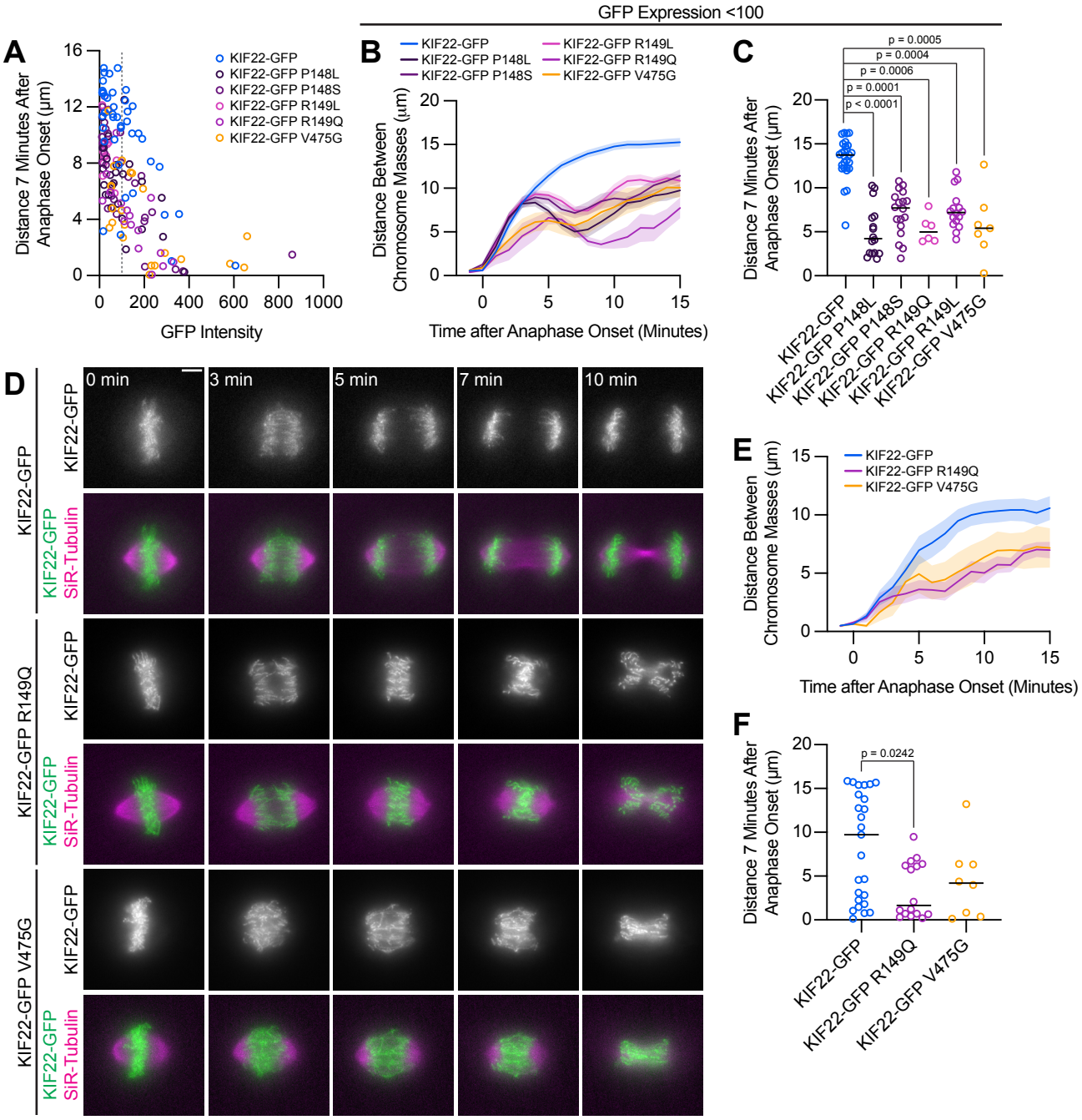

411 **Supplemental Figure 3. Anaphase recongression defects are KIF22-GFP expression level**
412 **dependent and disrupt chromosome segregation in RPE1 cells.**
413 **(A)** Background-subtracted GFP intensity plotted against the distance between separating
414 chromosome masses at 7 minutes to assess dependence of recongression on expression level
415 (Spearman correlation coefficient -0.6246, one-tailed p value < 0.0001). Grey dashed line
416 indicates mean background subtracted GFP intensity of 100. 43 KIF22-GFP cells from 10
417 experiments, 21 KIF22-GFP P148L cells from 6 experiments, 28 KIF22-GFP P148S cells from 7
418 experiments, 16 KIF22-GFP R149L cells from 6 experiments, 17 KIF22-GFP R149Q cells from 4
419 experiments, and 21 KIF22-GFP V475G cells from 21 experiments. **(B)** Distance between
420 separating chromosome masses of cells expressing lower levels of KIF22-GFP (mean
421 background subtracted GFP intensity less than 100). Lines represent the mean and the shaded
422 area denotes SEM. 27 KIF22-GFP cells from 9 experiments, 16 KIF22-GFP P148L cells from 6
423 experiments, 18 KIF22-GFP P148S cells from 6 experiments, 16 KIF22-GFP R149L cells from 6
424 experiments, 6 KIF22-GFP R149Q cells from 3 experiments, and 7 KIF22-GFP V475G cells from
425 3 experiments. **(C)** Distance between separating chromosome masses 7 minutes after anaphase
426 onset of cells expressing lower levels of KIF22-GFP (mean background subtracted GFP intensity
427 less than 100). Bars indicate medians. p values from Kruskal-Wallis test. p values are greater
428 than 0.05 for comparisons without a marked p value. Data represent the same cell populations
429 presented in (B). **(D)** Time-lapse images of dividing RPE-1 cells expressing KIF22-GFP R149Q
430 or KIF22-GFP V475G. Imaged approximately 12-18 hours after treatment with doxycycline to
431 induce expression. Times indicate minutes after anaphase onset. Images are maximum intensity
432 projections in z through the entirety of the spindle. Scale bar 5 μm. Images are representative of
433 3 or more experiments. **(E)** Distance between separating chromosome masses throughout
434 anaphase in RPE-1 cells. Lines represent the mean and the shaded area denotes SEM. 25 KIF22-
435 GFP cells from 7 experiments, 16 KIF22-GFP R149Q cells from 6 experiments, and 8 KIF22-GFP
436 V475G cells from 6 experiments. **(F)** Distance between separating chromosome masses 7
437 minutes after anaphase onset in RPE-1 cells. Bars indicate medians. p value from Kruskal-Wallis
438 test. p values are greater than 0.05 for comparisons without a marked p value. Data represent
439 the same cell populations presented in (E).

440 **Mutations disrupt the separation of the spindle poles in anaphase**

441 Anaphase chromosome segregation requires both that chromosome arms and
442 centromeres move towards the spindle poles (anaphase A) (Asbury, 2017) and that the spindle
443 poles move away from one another (anaphase B) (Ris, 1949). To test whether the activity of
444 mutant KIF22 in anaphase affects one or both of these processes, anaphase was imaged in HeLa-
445 Kyoto cells expressing fluorescent markers for the poles (pericentrin-RFP) and centromeres
446 (CENPB-mCh) **(Figure 5A)**. The reduced distance between separating chromosome masses
447 seen in these cells **(Figure 5B, 5C)** was compared to the distances between the centromeres
448 **(Figure 5D, 5E)** and the distances between the poles **(Figure 5F, 5G)** as anaphase progressed.
449 The distances between all three structures showed the same trend: in cells expressing wild type
450 KIF22-GFP, the distance between chromosome masses, between centromeres, and between the
451 spindle poles increased throughout the measured time interval in anaphase. Pathogenic
452 mutations altered the movements of all three structures **(Figure 5B, 5D, 5F)**. The distance
453 between chromosome masses, between centromeres, and between the spindle poles 10 minutes
454 after anaphase onset was significantly reduced in cells expressing KIF22-GFP R149Q or KIF22-
455 GFP V475G **(Figure 5C, 5E, 5G)**. Comparing the distance between chromosome masses and
456 the spindle pole within each half spindle **(Figure 5H)** with the distance between centromeres and
457 the spindle pole in the same half spindles **(Figure 5I)** demonstrated that expression of mutant
458 KIF22 more potently reduced the segregation of chromosome arms than centromeres, consistent
459 with continued generation of polar ejection forces in anaphase. This suggests that pathogenic
460 mutations in KIF22 affect anaphase A by altering the movement of chromosome arms, but not
461 the shortening of the k-fibers, and affect anaphase B by altering spindle pole separation.

Figure 5

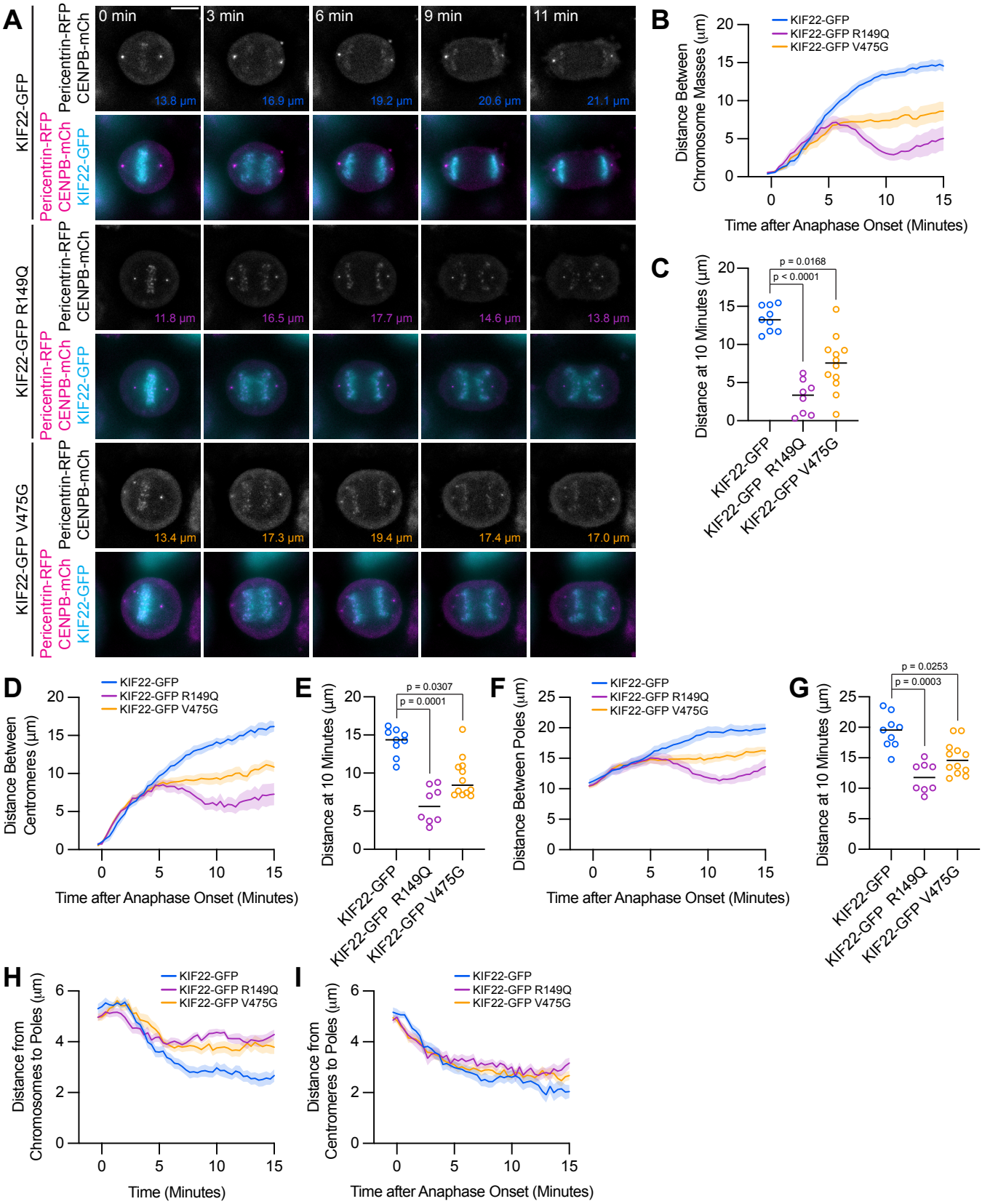
A
KIF22-GFP
KIF22-GFP R149Q
KIF22-GFP V475G
Pericentrin-RFP
CENPB-mCh
KIF22-GFP
0 min
3 min
6 min
9 min
11 min
13.8 µm
16.9 µm
19.2 µm
20.6 µm
21.1 µm
11.8 µm
16.5 µm
17.7 µm
14.6 µm
13.8 µm
13.4 µm
17.3 µm
19.4 µm
17.4 µm
17.0 µm
B
Distance Between Chromosome Masses (µm)
Time after Anaphase Onset (Minutes)
C
Distance at 10 Minutes (µm)
p = 0.0168
p < 0.0001
D
Distance Between Centromeres (µm)
E
p = 0.0307
p = 0.0001
F
Distance Between Poles (µm)
G
p = 0.0253
p = 0.0003
H
Distance from Chromosomes to Poles (µm)
Time (Minutes)
I
Distance from Centromeres to Poles (µm)

462 **Figure 5. Mutations disrupt the separation of spindle poles in anaphase.**
463 **(A)** Time-lapse images of dividing HeLa-Kyoto cells expressing pericentrin-RFP to mark the
464 spindle poles and CENPB-mCh to mark centromeres. Times indicate minutes after anaphase
465 onset. Colored distances in the bottom right of each greyscale image indicate the distance
466 between the spindle poles in the image. Images are maximum intensity projections in z through
467 the entirety of the spindle. Imaged approximately 24 hours after transfection and 12-18 hours after
468 treatment with doxycycline to induce expression. Images depicting pericentrin-RFP and CENPB-
469 mCh signal were background subtracted by duplicating each frame, applying a gaussian blur
470 (sigma 30 pixels), and subtracting this blurred image from the original. Scale bar 10 μm. Images
471 are representative of 3 or more experiments. **(B)** Distance between separating chromosome
472 masses throughout anaphase in HeLa-Kyoto cells. Lines represent the mean and the shaded
473 area denotes SEM. **(C)** Distance between separating chromosome masses 10 minutes after
474 anaphase onset in HeLa-Kyoto cells. Bars indicate medians. **(D)** Distance between centromeres
475 (CENPB-mCh) throughout anaphase in HeLa-Kyoto cells. Lines represent the mean and the
476 shaded area denotes SEM. **(E)** Distance between centromeres 10 minutes after anaphase onset
477 in HeLa-Kyoto cells. Bars indicate medians. **(F)** Distance between spindle poles (pericentrin-RFP)
478 throughout anaphase in HeLa-Kyoto cells. Lines represent the mean and the shaded area
479 denotes SEM. **(G)** Distance between spindle poles 10 minutes after anaphase onset in HeLa-
480 Kyoto cells. Bars indicate medians. Measurements from the same cells (9 KIF22-GFP cells from
481 5 experiments, 8 KIF22-GFP R149Q cells from 4 experiments, and 12 KIF22-GFP V475G cells
482 from 6 experiments) are shown in B-G. For C, E, and G, p values from Kruskal-Wallis test. **(H)**
483 Distance between chromosome masses and spindle poles throughout anaphase in HeLa-Kyoto
484 cells. Lines represent the mean and the shaded area denotes SEM. **(I)** Distance between
485 centromeres and spindle poles throughout anaphase in HeLa-Kyoto cells. Lines represent the
486 mean and the shaded area denotes SEM. Measurements from the same cells (18 KIF22-GFP,
487 16 KIF22-GFP R149Q, and 24 KIF22-GFP V475G half-spindles) as in B-G are shown in H and I.

488 **Division of cells expressing KIF22 with pathogenic mutations results in daughter cells with**
489 **abnormally shaped nuclei**

490 To understand the consequences of the observed defects in anaphase chromosome
491 segregation, we examined the daughter cells produced by the division of cells expressing KIF22-
492 GFP with pathogenic mutations. In these cells, the nuclei are lobed and fragmented **(Figure 6A)**.
493 The percentage of divisions resulting in nuclear morphology defects was approximately ten-fold
494 higher than in control cells (KIF22-GFP 6%, KIF22-GFP R149Q 64%, KIF22-GFP V475G 68%)
495 when live divisions were observed **(Figure 4E)**. To further quantify this phenotype, the solidity of
496 fixed cell nuclei (the ratio of the area of each nucleus to the area of the convex shape that would
497 enclose it) was measured. A perfectly oval nucleus would have a solidity value of one. Solidity
498 values were reduced in cells expressing KIF22-GFP with pathogenic mutations **(Figure 6B)**,
499 indicating that these cells had more irregularly shaped nuclei. This reduction in solidity was
500 dominant and occurred both in the presence of endogenous KIF22 and when endogenous KIF22
501 was depleted via siRNA knockdown. Using the fifth percentile solidity of control cells (control
502 knockdown, GFP expression) as a cut-off, 44-63% of cells expressing mutant KIF22-GFP had
503 abnormally shaped nuclei 24 hours after treatment with doxycycline to induce expression of
504 KIF22-GFP **(Figure 6C)**. Expression of wild type KIF22-GFP also resulted in a small increase in
505 the percentage of cells with abnormally shaped nuclei (12%). This percentage was reduced when
506 endogenous KIF22 was depleted (7%), consistent with nuclear morphology defects resulting from
507 an increase in KIF22 activity.

508 Expression of KIF22-GFP with pathogenic mutations also caused abnormally shaped
509 nuclei in RPE-1 cells **(Figure S4A)**. The solidity of nuclei in cells expressing mutant KIF22-GFP
510 was reduced **(Figure S4B)**, and 40-49% of RPE-1 cells expressing mutant KIF22-GFP had
511 abnormally shaped nuclei, again defined as a solidity value less than the fifth percentile of control
512 cells **(Figure 4C)**. In RPE-1 cells, expression of wild type KIF22-GFP resulted in a higher
513 percentage of cells with abnormally shaped nuclei (18% in control knockdown cells, 15% with
514 KIF22 knockdown) than was seen in HeLa-Kyoto cells. This may be a result of the higher
515 expression level of KIF22-GFP in the RPE-1 inducible cell lines **(Figure S1I, S1K)**.

516 To determine whether these nuclear morphology defects depended on the ability of KIF22
517 to generate forces within the mitotic spindle, cells were treated with nocodazole to depolymerize
518 microtubules and reversine to silence the spindle assembly checkpoint, allowing cells to enter
519 and exit mitosis without assembling a spindle or segregating chromosomes (Samwer et al., 2017;
520 Serra-Marques et al., 2020) **(Figure 6D)**. The solidity of nuclei was measured before
521 chromosomes condensed **(Figure 6E)** and after mitotic exit **(Figure 6F)**. At both time points, there

522 was no difference in nuclear shape between control cells and cells expressing KIF22-GFP with
523 pathogenic mutations, indicating that the effects of mutations on nuclear structure are spindle-
524 dependent.

525 The effect of nuclear morphology defects on daughter cell fitness may partially depend on
526 whether the nuclear envelopes of abnormally shaped nuclei are intact. The expression of mCherry
527 (mCh) with a nuclear localization signal (NLS) indicated that even highly lobed and fragmented
528 nuclei in cells expressing mutant KIF22-GFP are capable of retaining nuclear-localized proteins
529 **(Figure 6G)**. This suggests that the nuclear envelopes of these abnormally shaped nuclei are still
530 intact enough to function as a permeability barrier (Hatch, Fischer, Deerinck, & Hetzer, 2013).

Figure 6

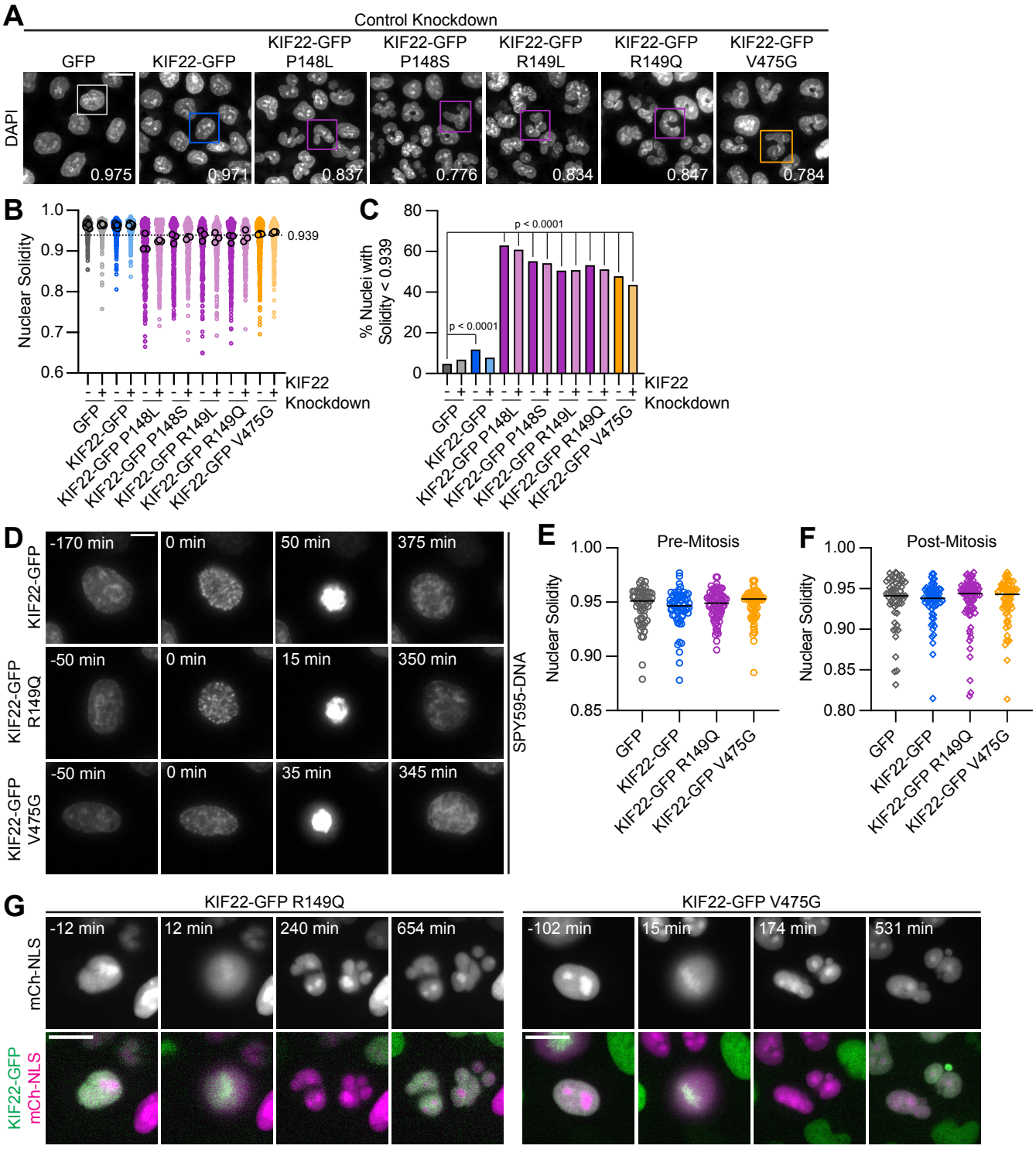
A
Control Knockdown
GFP
KIF22-GFP
KIF22-GFP P148L
KIF22-GFP P148S
KIF22-GFP R149L
KIF22-GFP R149Q
KIF22-GFP V475G
DAPI
0.975
0.971
0.837
0.776
0.834
0.847
0.784
B
Nuclear Solidity
1.0
0.9
0.8
0.7
0.6
0.939
KIF22
Knockdown
C
% Nuclei with Solidity < 0.939
80
60
40
20
0
p < 0.0001
p < 0.0001
D
KIF22-GFP
KIF22-GFP R149Q
KIF22-GFP V475G
-170 min
0 min
50 min
375 min
-50 min
0 min
15 min
350 min
-50 min
0 min
35 min
345 min
SPY595-DNA
E
Pre-Mitosis
Nuclear Solidity
1.00
0.95
0.90
0.85
F
Post-Mitosis
Nuclear Solidity
1.00
0.95
0.90
0.85
0.80
G
KIF22-GFP R149Q
KIF22-GFP V475G
mCh-NLS
KIF22-GFP
mCh-NLS
-12 min
12 min
240 min
654 min
-102 min
15 min
174 min
531 min

531 **Figure 6: Division of cells expressing KIF22 with pathogenic mutations results in daughter**
532 **cells with abnormally shaped nuclei.**
533 **(A)** DAPI stained nuclei of cells expressing KIF22 with pathogenic mutations. Values in the bottom
534 right of each image indicate the solidity of the boxed nucleus. Fixed approximately 24 hours after
535 treatment with doxycycline to induce expression. Scale bar 20 μm. Images are representative of
536 3 or more experiments. **(B)** Measured solidity of nuclei in HeLa-Kyoto cell lines. Small circles
537 represent the solidity of individual nuclei, and large circles with black outlines indicate the median
538 of each experiment. A dashed line marks a solidity value of 0.939, the fifth percentile of solidity
539 for control cells transfected with control siRNA and expressing GFP. **(C)** Percentage of nuclei with
540 abnormal shape, indicated by a solidity value less than 0.939, the fifth percentile of control (control
541 knockdown, GFP expression) cell solidity. A chi-square test of all data produced a p value <
542 0.0001. Plotted p values are from pairwise post-hoc chi-square tests comparing control (control
543 knockdown, GFP expression) cells to each other condition. Applying the Bonferroni correction for
544 multiple comparisons, a p value of less than 0.00385 was considered significant. p values are
545 greater than 0.00385 for comparisons without a marked p value. Data in (B) and (C) represent
546 1045 GFP cells transfected with control siRNA, 849 GFP cells transfected with KIF22 siRNA, 994
547 KIF22-GFP cells transfected with control siRNA, 980 KIF22-GFP cells transfected with KIF22
548 siRNA, 472 KIF22-GFP P148L cells transfected with control siRNA, 442 KIF22-GFP P148L cells
549 transfected with KIF22 siRNA, 382 KIF22-GFP P148S cells transfected with control siRNA, 411
550 KIF22-GFP P148S cells transfected with KIF22 siRNA, 336 KIF22-GFP R149L cells transfected
551 with control siRNA, 376 KIF22-GFP R149L cells transfected with KIF22 siRNA, 466 KIF22-GFP
552 R149Q cells transfected with control siRNA, 359 KIF22-GFP R149Q cells transfected with KIF22
553 siRNA, 605 KIF22-GFP V475G cells transfected with control siRNA, and 386 KIF22-GFP V475G
554 cells transfected with KIF22 siRNA. GFP and KIF22-GFP cells represent 6 experiments, data
555 from all other cell lines represent 3 experiments. **(D)** Time-lapse images of HeLa-Kyoto cells
556 treated with nocodazole and reversine and stained with SPY595-DNA to visualize chromosomes.
557 Time indicates the number of minutes before or after chromosome condensation. Images are
558 maximum intensity projections in z of two focal planes, one at the level of interphase nuclei and
559 one at the level of mitotic chromosomes. Imaged approximately 8 hours after treatment with
560 doxycycline to induce expression, 1.5-2 hours after treatment with SPY595-DNA, and 0.5-1 hour
561 after treatment with nocodazole and reversine. Scale bar 10 μm. Images are representative of 3
562 or more experiments. **(E)** Nuclear solidity of HeLa-Kyoto cells treated with nocodazole and
563 reversine. Measurements were made 15 minutes before chromosome condensation. **(F)** Nuclear
564 solidity of HeLa-Kyoto cells treated with nocodazole and reversine. Measurements were made

565 100 minutes after chromosome decondensation. Data in (E) and (F) represent 56 GFP, 60 KIF22-
566 GFP, 76 KIF22-GFP R149Q, and 67 KIF22-GFP V475G cells from 3 experiments per condition.
567 For (E) and (F), bars indicate medians, and the Kruskal-Wallis test indicated no significant
568 difference between groups. **(G)** Time-lapse images of HeLa-Kyoto cells expressing mCherry
569 (mCh)-NLS to assess nuclear envelope integrity. Times indicate minutes before or after
570 chromosome condensation. Imaged approximately 8 hours after treatment with doxycycline to
571 induce expression and 24 hours after transfection with mCh-CAAX. Scale bar 20 μm. Images are
572 representative of 3 or more experiments.

Supplemental Figure 4

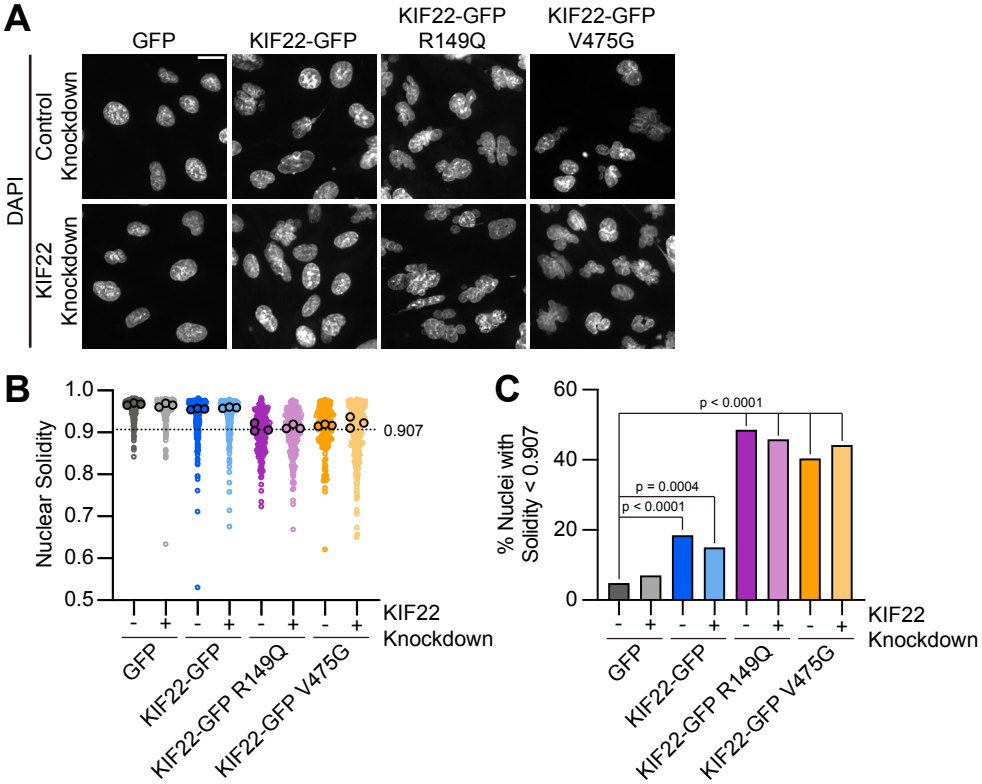

573 **Supplemental Figure 4: Mutations cause abnormally shaped nuclei in RPE1 cells.**
574 **(A)** DAPI-stained nuclei of RPE-1 cells expressing KIF22-GFP with pathogenic mutations. Fixed
575 approximately 24 hours after treatment with doxycycline to induce expression. Scale bar 20 μm.
576 Images are representative of 3 or more experiments. **(B)** Measured solidity of nuclei in RPE-1 cell
577 lines. Small circles represent the solidity of individual nuclei, and large circles with black outlines
578 indicate the median of each experiment. A dashed line marks a solidity value of 0.907, the fifth
579 percentile of solidity for control cells transfected with control siRNA and expressing GFP. **(C)**
580 Percentage of nuclei with abnormal shape, indicated by a solidity value less than 0.907, the fifth
581 percentile of control (control knockdown, GFP expression) cell solidity. A chi-square test of all
582 data produced a p value < 0.0001. Plotted p values are from pairwise post-hoc chi-square tests
583 comparing control (control knockdown, GFP expression) cells to each other condition. Applying
584 the Bonferroni correction for multiple comparisons, a p value of less than 0.00714 was considered
585 significant. p values are greater than 0.00714 for comparisons without a marked p value. Data in
586 (B) and (C) represent 206 GFP transfected with control siRNA, 200 GFP cells transfected with
587 KIF22 siRNA, 233 KIF22-GFP cells transfected with control siRNA, 240 KIF22-GFP cells
588 transfected with KIF22 siRNA, 214 KIF22-GFP R149Q cells transfected with control siRNA, 207
589 KIF22-GFP R149Q cells transfected with KIF22 siRNA, 146 KIF22-GFP V475G cells transfected
590 with control siRNA, and 244 KIF22-GFP V475G cells transfected with KIF22 siRNA from 3
591 experiments.

592 **Proliferation is reduced in cells expressing KIF22 with pathogenic mutations**

593 If defects in anaphase chromosome segregation and nuclear morphology affect cellular
594 function, they may impact the ability of cells to proliferate. To test this, HeLa-Kyoto cells
595 expressing KIF22-GFP with pathogenic mutations were imaged over 96 hours to count the
596 numbers of cells over time **(Figure 7A)**. The growth rates of cells expressing mutant KIF22 were
597 reduced **(Figure 7B)**. After 96 hours, the fold change in cell number was reduced by
598 approximately 30% for cells expressing KIF22-GFP with pathogenic mutations (GFP control
599 median 5.3, KIF22-GFP R149Q 3.7, KIF22-GFP V475G 3.8) **(Figure 7C)**.

600 To consider what might be limiting the proliferation rate of cells expressing mutant KIF22-
601 GFP, predictions for proliferation rate based on the observed rates of nuclear morphology defects
602 and cytokinesis failure were calculated. For these purposes, only data from the first 48 hours of
603 the proliferation assay were used, as cell growth rates plateaued after this timepoint. The doubling
604 time of control HeLa-Kyoto cells expressing GFP was calculated to be 20.72 hours in these
605 experiments, which is consistent with published data (Y. Liu et al., 2018). Using this doubling rate,
606 assuming exponential growth, and assuming every cell divides, the normalized cell count at 48
607 hours (normalized to a starting cell count of 1) was predicted to be 4.98. This is close to the
608 experimental 48-hour cell count for control cells (4.60), and higher than the experimental 48-hour
609 cell count for cells expressing KIF22-GFP R149Q (3.13) or V475G (3.60), as these cell lines have
610 reduced proliferation **(Figure 7B, square)**. If one assumed that cells with abnormally shaped
611 nuclei stop dividing, given that approximately 60% of mutant KIF22-GFP cell divisions result in
612 abnormally shaped nuclei **(Figure 4E),** the predicted cell count at 48 hours would be 2.18 **(Figure**
613 **7B, triangle)**. This is lower than the experimental cell count for cells expressing mutant KIF22-
614 GFP, suggesting that cells with abnormally shaped nuclei must be capable of additional divisions.
615 If, instead, one assumed that only cells that fail cytokinesis (30% of cells **(Figure 4E)**) stop
616 dividing, the predicted cell count would be 3.42 **(Figure 7B, diamond)**. This value is consistent
617 with the experimental 48-hour cell count for cells expressing KIF22-GFP with pathogenic
618 mutations (3.13 – 3.60), suggesting the rate of cytokinesis failure may limit the rate of proliferation
619 in these cells. Consistent with this possibility, an increased number of large cells that may have
620 failed cytokinesis are visible in proliferation assay images at 72 hours **(Figure 7A)**.

621 To test the prediction that cells with nuclear morphology defects are capable of division,
622 KIF22-GFP expression was induced approximately 24 hours before imaging to generate a
623 population of cells with abnormally shaped nuclei. Division of these cells was observed **(Figure**
624 **7D)**, demonstrating that nuclear morphology defects do not prevent subsequent divisions. The
625 percentage of cells that divided over the course of this experiment was not reduced in cells

626 expressing KIF22-GFP with pathogenic mutations despite the abnormal nuclear morphology of
627 cells in those populations **(Figure 7E)**.

Figure 7

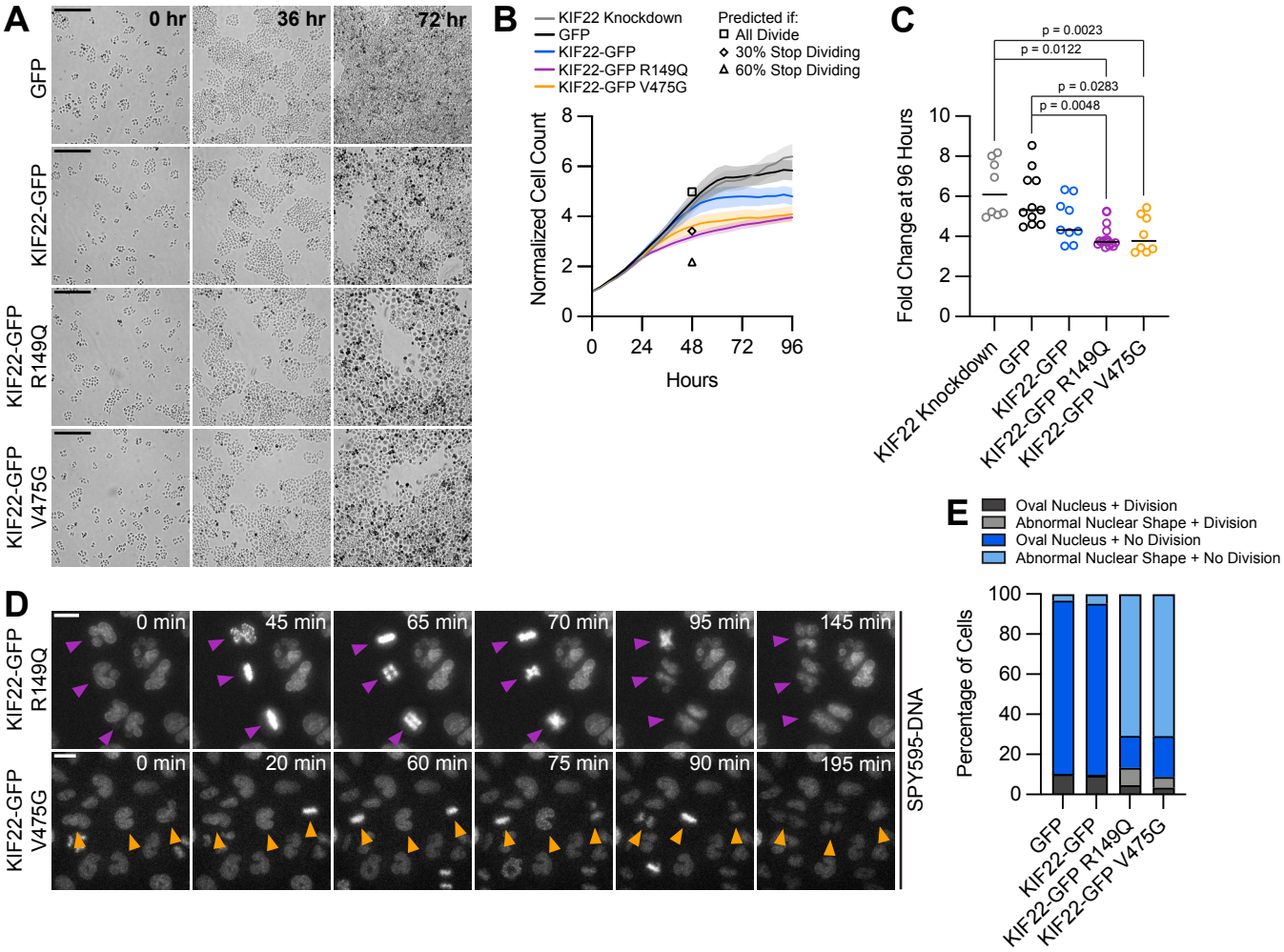
A
0 hr
36 hr
72 hr
GFP
KIF22-GFP
KIF22-GFP R149Q
KIF22-GFP V475G
B
KIF22 Knockdown
GFP
KIF22-GFP
KIF22-GFP R149Q
KIF22-GFP V475G
Predicted if:
All Divide
30% Stop Dividing
60% Stop Dividing
Normalized Cell Count
Hours
C
p = 0.0023
p = 0.0122
p = 0.0283
p = 0.0048
Fold Change at 96 Hours
KIF22 Knockdown
GFP
KIF22-GFP
KIF22-GFP R149Q
KIF22-GFP V475G
D
0 min
45 min
65 min
70 min
95 min
145 min
20 min
60 min
75 min
90 min
195 min
SPY595-DNA
E
Oval Nucleus + Division
Abnormal Nuclear Shape + Division
Oval Nucleus + No Division
Abnormal Nuclear Shape + No Division
Percentage of Cells

628 **Figure 7: Proliferation is reduced in cells expressing KIF22 with pathogenic mutations.**
629 **(A)** Time-lapse bright field images of HeLa-Kyoto cells to assess proliferation rate. Scale bar 500
630 μm. Images are representative of 3 or more experiments. **(B)** Proliferation rates measured using
631 automated bright field imaging. Lines represent the mean cell count, normalized to the number of
632 cells at 0 hours, and the shaded area denotes SEM. Black outlined shapes indicate the predicted
633 cell count for cell lines expressing pathogenic mutations at 48 hours if every cell doubled every
634 20.72 hours (the doubling time measured from 48 hours of control cell proliferation) (square), if
635 the rate of cytokinesis failure limited proliferation and 30% of cells did not divide (diamond), and
636 if the rate of nuclear morphology defects limited proliferation and 60% of cells did not divide
637 (triangle). **(C)** Fold change of normalized cell counts after 96 hours. Bars indicate medians. p
638 values from Kruskal-Wallis test. p values are greater than 0.05 for comparisons without a marked
639 p value. Data in (B) and (C) represent 8 KIF22 knockdown, 11 GFP, 9 KIF22-GFP, 16 KIF22-GFP
640 R149Q, and 8 KIF22-GFP V475G technical replicates from 4 experiments. **(D)** Time-lapse
641 imaging of HeLa-Kyoto cells treated with doxycycline for 24 hours to induce expression of KIF22-
642 GFP with pathogenic mutations and stained with SPY595-DNA. Arrowheads indicate cells with
643 abnormally shaped nuclei that divide. Images are maximum intensity projections in z of two focal
644 planes, one at the level of interphase nuclei and one at the level of mitotic chromosomes. Scale
645 bars 20 μm. Images are representative of 3 or more experiments. **(E)** Nuclear morphology at the
646 start of imaging (dark grey or blue, oval; light grey or blue; abnormal morphology) and outcome
647 (grey, cell divides during the experiment; blue, the cell does not divide). The total number of
648 dividing cells was compared between cell lines using the chi-square test ($p < 0.0001$ across all
649 conditions). Post-hoc chi-square tests comparing all conditions to one another indicated that the
650 proliferation rate of cells expressing KIF22-GFP R149Q is statistically different than that of cells
651 expressing GFP ($p = 0.0025$), KIF22-GFP ($p = 0.0003$), or KIF22-GFP V475G ($p < 0.0001$).
652 Applying the Bonferroni correction for multiple comparisons, a p value of less than 0.008 was
653 considered significant. p values are greater than 0.008 for all other comparisons. 2461 GFP, 2611
654 KIF22-GFP, 1890 KIF22-GFP R149Q, and 2346 KIF22-GFP V465G cells.

655 **Mimicking phosphorylation of T463 phenocopies pathogenic mutations**

656 The phenotypes observed in cells expressing KIF22-GFP with pathogenic mutations
657 suggest that mutations may prevent inactivation of KIF22 in anaphase, and that polar ejection
658 forces in anaphase disrupt chromosome segregation. If this is the case, then preventing KIF22
659 inactivation would be predicted to phenocopy the pathogenic mutations. One mechanism by
660 which KIF22 activity is controlled is phosphorylation of T463: phosphorylation of this tail residue
661 is necessary for polar ejection force generation, and dephosphorylation at anaphase onset
662 contributes to polar ejection force suppression (Soeda et al., 2016). Therefore, we generated
663 HeLa-Kyoto inducible cell lines expressing KIF22-GFP with phosphomimetic (T463D) and
664 phosphonull (T463A) mutations to test whether preventing KIF22 inactivation in anaphase by
665 expressing the constitutively active T463D construct phenocopies the expression of KIF22-GFP
666 with pathogenic mutations. When treated with doxycycline, these cells expressed
667 phosphomimetic and phosphonull KIF22-GFP at levels comparable to those seen in cell lines
668 expressing KIF22-GFP with pathogenic mutations, which was approximately two- to three-fold
669 higher than the level of expression of endogenous KIF22 **(Figure S5A-D)**.

670 To assess the activity of KIF22-GFP T463D and T463A in HeLa cells, polar ejection force
671 generation in monopolar spindles was measured **(Figure 8A)**. In cells with endogenous KIF22
672 present, expression of KIF22-GFP T463D increased the distance from the spindle pole to the
673 maximum DAPI signal (GFP control 3.7 ± 0.07 μm, KIF22-GFP T463D 4.4 ± 0.12, mean ± SEM),
674 indicating increased polar ejection forces, consistent with phosphorylation of T463 activating
675 KIF22 in prometaphase (Soeda et al., 2016) **(Figure 8B)**. Conversely, when endogenous KIF22
676 was depleted, expression of KIF22-GFP T463A was less able to rescue polar ejection force
677 generation (distance from the spindle pole to the maximum DAPI signal 3.0 ± 0.08 μm, mean ±
678 SEM) than expression of wild type KIF22-GFP (3.6 ± 0.07 μm) or KIF22-GFP T463D (3.7 ± 0.10
679 μm) **(Figure 8C)**. Again, this is consistent with previous work demonstrating that KIF22
680 phosphorylation at T463 activates the motor for prometaphase polar ejection force generation
681 (Soeda et al., 2016), although the reduction in polar ejection forces seen with KIF22-GFP T463A
682 rescue is less severe in our system, possibly due to differences in cell type, level of depletion of
683 endogenous KIF22, or the method used to quantify polar ejection forces.

684 In anaphase, expression of phosphomimetic KIF22-GFP T463D, but not phosphonull
685 KIF22-GFP T463A, caused chromosome recongression **(Figure 8D, 8E)**. The distance between
686 chromosome masses at 7 minutes was reduced in cells expressing KIF22-GFP T463D (median
687 5.8 μm) compared to cells expressing wild type KIF22-GFP (12.5 μm) or KIF22-GFP T463A (10.8
688 μm) **(Figure 8F)**. As in cells expressing KIF22-GFP with pathogenic mutations, the severity of

689 anaphase chromosome recongression, indicated by the distance between chromosome masses
690 at 7 minutes, was dependent on GFP expression level (Spearman correlation coefficient -0.3964,
691 one-tailed p value 0.0004) **(Figure S5E)**. When only cells expressing lower levels of KIF22-GFP
692 (mean background subtracted intensity <100 arbitrary units) were considered, the same effect
693 (expression of KIF22-GFP T463D causes recongression) was still observed **(Figure S5F, S5G)**.
694 This recongression phenocopies the effect of pathogenic mutations on anaphase chromosome
695 segregation, consistent with pathogenic mutations preventing anaphase inactivation of KIF22.
696 In addition to causing the same defects in anaphase chromosome segregation, expression
697 of KIF22-GFP T463D also affects daughter cell nuclear morphology. Cells expressing KIF22-GFP
698 T463D have lobed and fragmented nuclei **(Figure S5H)** and correspondingly reduced nuclear
699 solidity measurements **(Figure 8G)**. An increased percentage of cells expressing KIF22-GFP
700 T463D in the presence of endogenous KIF22 (65%) or in cells depleted of endogenous KIF22
701 (72%) have abnormally shaped nuclei, as indicated by a solidity value below the fifth percentile
702 of control cell nuclear solidity **(Figure 8H)**.
703 Expression of KIF22-GFP T463A also resulted in a small increase in the percentage of
704 abnormally shaped nuclei (26% in control or KIF22 knockdown conditions) **(Figure 8H)**. Since
705 expression of KIF22-GFP T463A does not cause anaphase recongression **(Figure 8E)**, the level
706 of compaction of the segregating chromosome masses was explored as a possible explanation
707 for this modest increase in the percentage of cells with nuclear morphology defects. In KIF22
708 knockout mice, loss of KIF22 reduces chromosome compaction in anaphase, causing the
709 formation of multinucleated cells (Ohsugi et al., 2008). The phosphonull T463A mutation reduces
710 KIF22 activity and may therefore exhibit a KIF22 loss of function phenotype. Measurement of the
711 widths of separating chromosome masses in anaphase **(Figure S5I)** did demonstrate a modest
712 broadening of the chromosome masses in cells expressing KIF22-GFP T463A **(Figure S5J,**
713 **S5K)**, which may contribute to the modest defects in nuclear morphology seen in these cells.

Figure 8

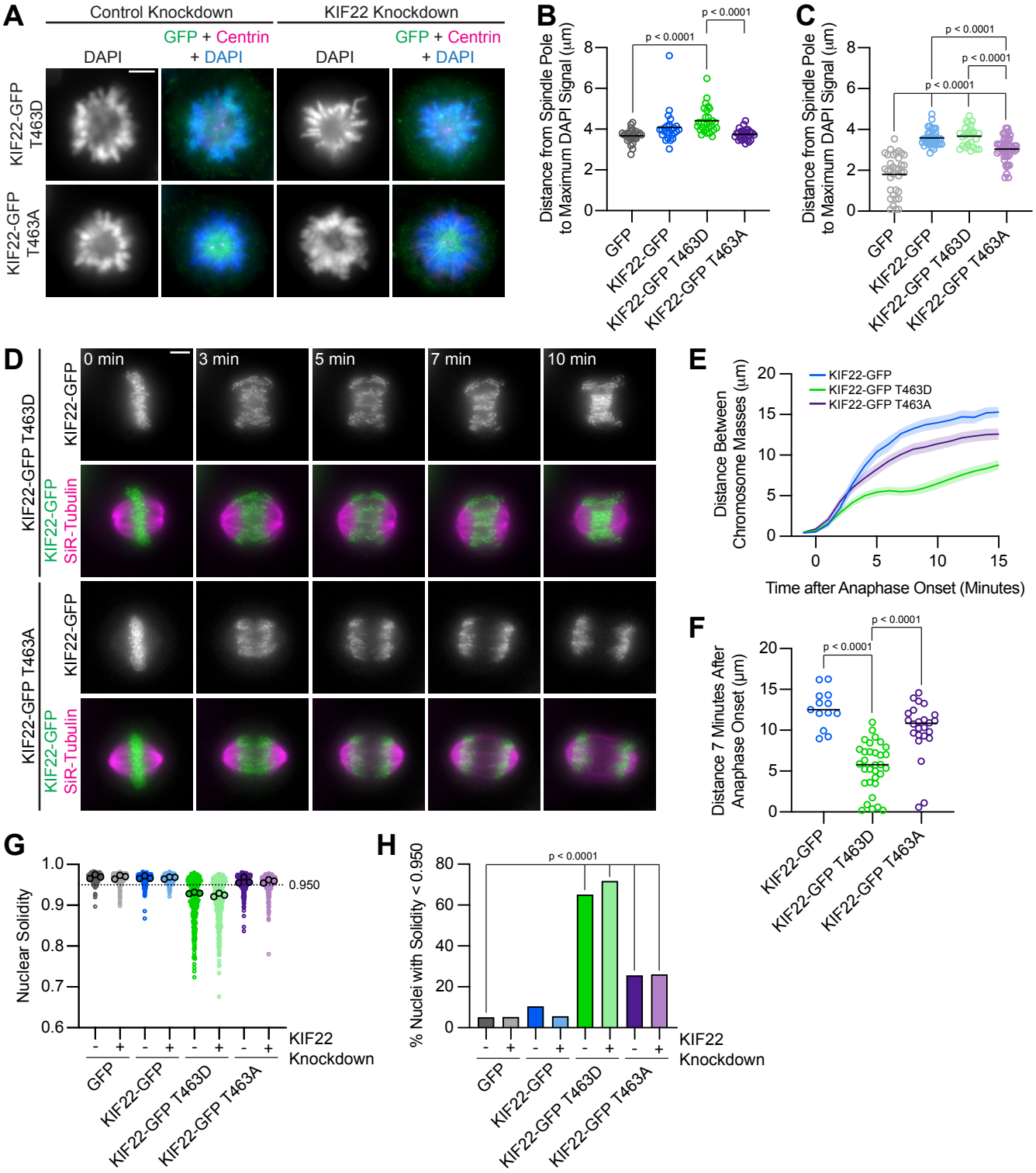
A
Control Knockdown
KIF22 Knockdown
DAPI
GFP + Centrin + DAPI
KIF22-GFP T463D
KIF22-GFP T463A
B
Distance from Spindle Pole to Maximum DAPI Signal (µm)
p < 0.0001
GFP
KIF22-GFP
KIF22-GFP T463D
KIF22-GFP T463A
C
Distance from Spindle Pole to Maximum DAPI Signal (µm)
p < 0.0001
D
0 min
3 min
5 min
7 min
10 min
KIF22-GFP T463D
KIF22-GFP T463A
KIF22-GFP
KIF22-GFP SiR-Tubulin
E
Distance Between Chromosome Masses (µm)
Time after Anaphase Onset (Minutes)
KIF22-GFP
KIF22-GFP T463D
KIF22-GFP T463A
F
Distance 7 Minutes After Anaphase Onset (µm)
p < 0.0001
G
Nuclear Solidity
0.950
KIF22 Knockdown
H
% Nuclei with Solidity < 0.950
p < 0.0001
KIF22 Knockdown

714 **Figure 8: Phosphomimetic mutation of T463 phenocopies pathogenic mutations in KIF22.**
715 **(A)** Immunofluorescence images of monopolar HeLa-Kyoto cells. KIF22-GFP was visualized
716 using an anti-GFP antibody. Fixed approximately 2-3 hours after treatment with monastrol and 24
717 hours after siRNA transfection and treatment with doxycycline to induce expression. Scale bar 5
718 μm. Images are representative of 3 or more experiments. **(B)** Distance from the spindle pole to
719 the maximum DAPI signal, a measure of relative polar ejection force level, between HeLa-Kyoto
720 cell lines expressing KIF22-GFP with phosphomimetic and phosphonull mutations at T463. 26
721 GFP cells from 3 experiments, 26 KIF22-GFP cells from 3 experiments, 29 KIF22-GFP T463D
722 cells from 3 experiments, and 29 KIF22-GFP T463A cells from 3 experiments. **(C)** Distance from
723 the spindle pole to the maximum DAPI signal in cells depleted of endogenous KIF22 and
724 expressing KIF22-GFP with phosphomimetic and phosphonull mutations at T463. 35 GFP cells
725 from 4 experiments, 36 KIF22-GFP cells from 4 experiments, 27 KIF22-GFP T463D cells from 3
726 experiments, and 47 KIF22-GFP T463A cells from 4 experiments. For B-C, bars indicate means.
727 p values from Brown-Forsythe and Welch ANOVA with Dunnett's T3 multiple comparisons test. p
728 values are greater than 0.05 for comparisons without a marked p value. **(D)** Time-lapse images
729 of dividing HeLa-Kyoto cells. Cells expressing KIF22-GFP T463D exhibit recongression of the
730 chromosomes during anaphase. Times indicate minutes after anaphase onset. Images are
731 maximum intensity projections in z through the entirety of the spindle. Imaged approximately 18
732 hours after treatment with doxycycline to induce expression. Scale bar 5 μm. Images are
733 representative of 3 or more experiments. **(E)** Distance between separating chromosome masses
734 throughout anaphase in HeLa-Kyoto cells. Lines represent the mean and the shaded area
735 denotes SEM. 13 KIF22-GFP, 32 KIF22-GFP T463D, and 24 KIF22-GFP T463A cells from 5
736 experiments. **(F)** Distance between separating chromosome masses 7 minutes after anaphase
737 onset. Bars indicate medians. p values from Kruskal-Wallis test. p values are greater than 0.05
738 for comparisons without a marked p value. 13 KIF22-GFP, 32 KIF22-GFP T463D, and 24 KIF22-
739 GFP T463A cells from 5 experiments per condition. **(G)** Measured solidity of nuclei in HeLa-Kyoto
740 cell lines. Small circles represent the solidity of individual nuclei, and large circles with black
741 outlines indicate the median of each experiment. A dashed line marks a solidity value of 0.950,
742 the fifth percentile of solidity for control cells transfected with control siRNA and expressing GFP.
743 **(H)** Percentage of nuclei with abnormal shape, indicated by a solidity value less than 0.950, the
744 fifth percentile of control (control knockdown, GFP expression) cell solidity. A chi-square test of
745 all data produced a p value < 0.0001. Plotted p values are from pairwise post-hoc chi-square tests
746 comparing control (control knockdown, GFP expression) cells to each other condition. Applying

747 the Bonferroni correction for multiple comparisons, a p value of less than 0.00714 was considered
748 significant. p values are greater than 0.00714 for comparisons without a marked p value. Data in
749 (G) and (H) represent 312 GFP cells transfected with control siRNA, 362 GFP cells transfected
750 with KIF22 siRNA, 314 KIF22-GFP cells transfected with control siRNA, 320 KIF22-GFP cells
751 transfected with KIF22 siRNA, 361 KIF22-GFP T463D cells transfected with control siRNA, 376
752 KIF22-GFP T463D cells transfected with KIF22 siRNA, 312 KIF22-GFP T463A cells transfected
753 with control siRNA, and 376 KIF22-GFP T463A cells transfected with KIF22 siRNA from 3
754 experiments.

Supplemental Figure 5

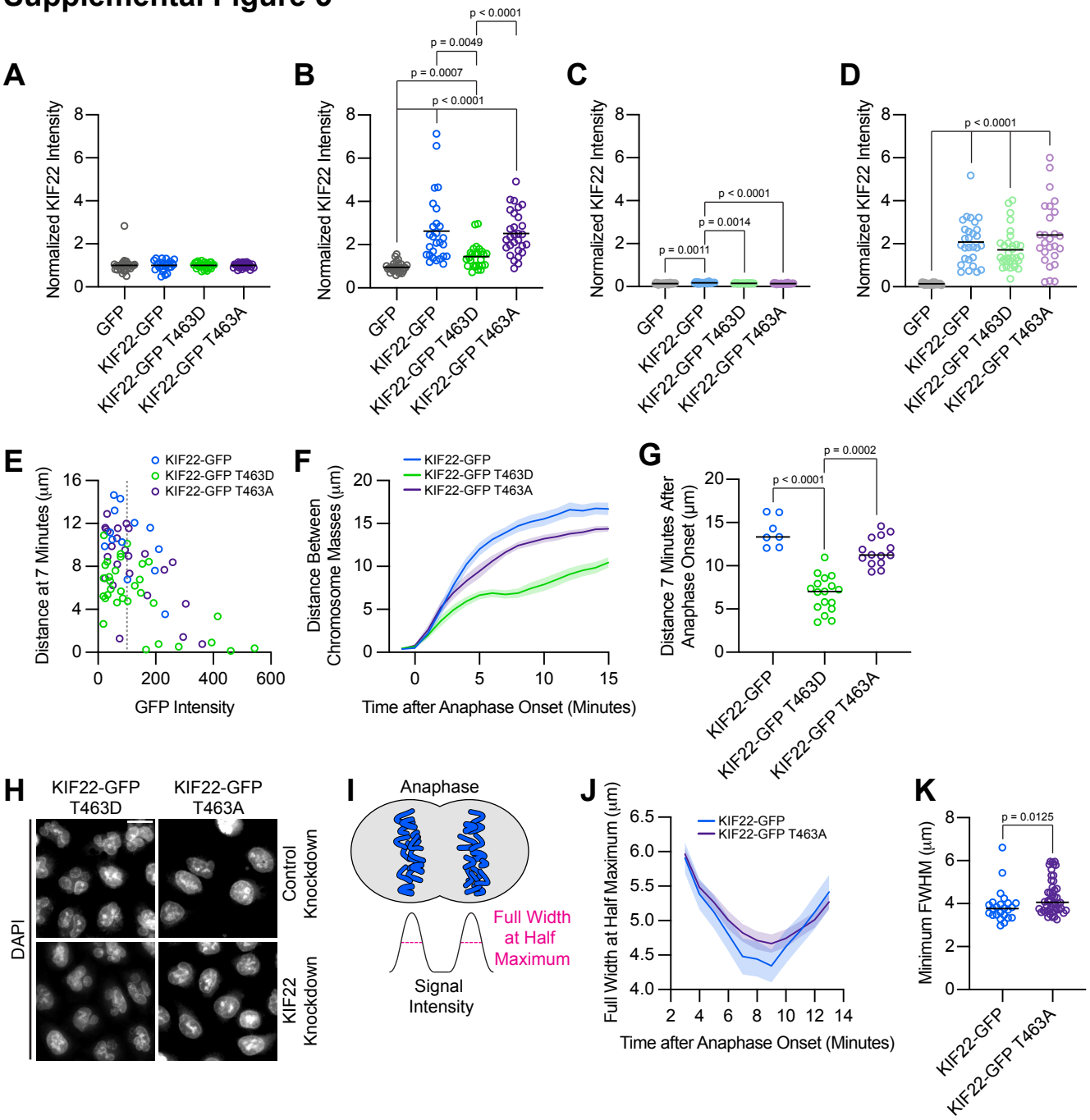

755 **Supplemental Figure 5: Cells expressing KIF22-GFP T463A have broader anaphase**
756 **chromosome masses.**
757 **(A-D)** Quantification of KIF22 fluorescence intensity in untreated HeLa-Kyoto cells transfected
758 with control siRNA (A), cells treated with doxycycline to induce expression and transfected with
759 control siRNA (B), untreated cells transfected with KIF22 siRNA (C), and cells treated with
760 doxycycline and transfected with KIF22 siRNA (D) normalized to the mean intensity of uninduced,
761 control knockdown cells (endogenous KIF22 expression level) for each cell line (A). 32 GFP, 25
762 KIF22-GFP,28 KIF22-GFP T463D, and 31 KIF22-GFP T463A untreated cells transfected with
763 control siRNA (A), 29 GFP, 27 KIF22-GFP, 27 KIF22-GFP T463D, and 29 KIF22-GFP T463A
764 doxycycline-treated cells transfected with control siRNA (B), 25 GFP, 26 KIF22-GFP, 23 KIF22-
765 GFP T463D, and 26 KIF22-GFP T463A untreated cells transfected with KIF22 siRNA (C), 28
766 GFP, 28 KIF22-GFP, 31 KIF22-GFP T463D, and 26 KIF22-GFP T463A doxycycline-treated cells
767 transfected with KIF22 siRNA (D), from 3 experiments. **(E)** Plotting background-subtracted GFP
768 intensity against the distance between separating chromosome masses at 7 minutes indicates
769 that this distance is dependent on expression level (Spearman correlation coefficient -0.3964,
770 one-tailed p value = 0.0004). Grey dashed line indicates mean background subtracted GFP
771 intensity of 100. 13 KIF22-GFP, 32 KIF22-GFP T463D, and 24 KIF22-GFP T463A cells from 5
772 experiments. **(F)** Distance between separating chromosome masses of cells expressing lower
773 levels of KIF22-GFP (mean background subtracted GFP intensity less than 100). Lines represent
774 the mean and the shaded area denotes SEM. 7 KIF22-GFP cells from 4 experiments, 17 KIF22-
775 GFP T463D cells from 5 experiments, and 14 KIF22-GFP T463A cells from 4 experiments. **(G)**
776 Distance between separating chromosome masses 7 minutes after anaphase onset of cells
777 expressing lower levels of KIF22-GFP (mean background subtracted GFP intensity less than
778 100). Bars indicate medians. p values from Kruskal-Wallis test. p values are greater than 0.05 for
779 comparisons without a marked p value. 7 KIF22-GFP cells from 4 experiments, 17 KIF22-GFP
780 T463D cells from 5 experiments, and 14 KIF22-GFP T463A cells from 4 experiments. **(H)** DAPI-
781 stained nuclei of Hela-Kyoto cells. Fixed approximately 24 hours after treatment with doxycycline
782 to induce expression. Scale bar 20 μm. Images are representative of 3 or more experiments. **(I)**
783 Schematic depicting the measurement of chromosome signal intensity in anaphase and the use
784 of the full width at half maximum (FWHM) as a measure of anaphase chromosome mass
785 broadness. **(J)** Full width at half maximum of the plotted intensities of separating chromosome
786 masses of HeLa-Kyoto cells expressing KIF22-GFP or KIF22-GFP T463A. Lines represent the
787 mean and the shaded area denotes SEM. **(K)** Minimum FWHM value, representing maximal
788 anaphase chromosome compaction, between cells expressing KIF22-GFP and KIF22-GFP

789 T463A. p value from Mann-Whitney test. Bars represent medians. Data in (J) and (K) represent
790 12 KIF22-GFP and 24 KIF22-GFP T463A cells (24 KIF22-GFP and 48 KIF22-GFP T463A
791 chromosome masses) from 5 experiments.

792 **Mimicking phosphorylation of T158 in the α2 helix phenocopies pathogenic mutations**

793 The effect of mutations in the α2 helix on KIF22 function suggests the involvement of this
794 region of the motor domain in KIF22 inactivation. If this was true, post-translational modification
795 of α2 may contribute to the regulation of KIF22 activity, analagous to the regulation of KIF22
796 inactivation via the dephosphorylation of T463 in the tail. Phosphorylation of amino acids T134 in
797 α2a (Kettenbach et al., 2011) and T158 in α2b (Olsen et al., 2010; Rigbolt et al., 2011) has been
798 documented in phosphoproteomic studies. HeLa-Kyoto cells expressing KIF22-GFP with
799 phosphomimetic and phosphonull mutations at T134 and T158 were generated to test whether
800 either site may contribute to the regulation of KIF22 inactivation.

801 T134 is located in α2a, near the catalytic site of KIF22 **(Figure S6A)**. Both phosphonull
802 (T134A) and phosphomimetic (T134D) mutations at this site disrupted the localization of KIF22.
803 KIF22-GFP T134D and T134A localize to spindle microtubules rather than to the chromosomes
804 **(Figure S6B)**. Expression of KIF22-GFP T134D and KIF22-GFP T134A also resulted in the
805 formation of multipolar spindles in a subset of cells **(Figure S6C)**. These phenotypes are
806 consistent with previous work that used T134N as a rigor mutation to test the necessity of KIF22
807 motor activity for spindle length maintenance (Tokai-Nishizumi et al., 2005). The phenotypes
808 observed in cells expressing KIF22-GFP T134D or KIF22-GFP T134A are not the same as those
809 observed in cells expressing KIF22-GFP T463D, suggesting that phosphoregulation of T134 is
810 not involved in the inactivation of KIF22.

811 T158 is located in α2b, the same region of the α2 helix containing amino acids P148 and
812 R149, which are mutated in patients with SEMDJL2 **(Figure 9A)**. Localization of KIF22 to
813 chromosomes is not disrupted by phosphomimetic (T158D) or phosphonull (T158A) mutations at
814 this site. To assess the activity of KIF22-GFP T158D and KIF22-GFP T158A, relative polar
815 ejection forces were measured in monopolar spindles **(Figure 9B)**. In the presence of
816 endogenous KIF22, expression of neither KIF22-GFP T158D nor KIF22-GFP T158A disrupted
817 the generation of polar ejection forces **(Figure 9C)**. In cells depleted of endogenous KIF22,
818 expression of KIF22-GFP, KIF22-GFP T158D, or KIF22-GFP T158A was sufficient to rescue polar
819 ejection force generation **(Figure 9D)**, indicating that KIF22 with mutations at T158 is active in
820 prometaphase and capable of generating polar ejection forces.

821 To test the effects of phosphomimetic and phosphonull mutations at T158 in anaphase,
822 distances between separating chromosome masses in cells expressing KIF22-GFP, KIF22-GFP
823 T158D, or KIF22-GFP T158A were measured. Expression of KIF22-GFP T158D caused
824 chromosome recongression, while expression of KIF22-GFP T158A did not affect chromosome
825 movements in anaphase **(Figure 9E, 9F)**. The distance between separating chromosome masses

826 7 minutes after anaphase onset was reduced in cells expressing KIF22-GFP T158D (median 6.4
827 μm) compared to cells expressing KIF22-GFP (12.4 μm) or KIF22-GFP T158A (13.6 μm) **(Figure**
828 **9G)**. Mimicking phosphorylation of T158 also affected daughter cell nuclear morphology. Nuclear
829 solidity was reduced in cells expressing KIF22-GFP T158D **(Figure 9H)**, and correspondingly the
830 percentage of cells with abnormally shaped nuclei, designated as a solidity value lower than the
831 5th percentile solidity of control cells expressing GFP, was increased in cells expressing KIF22-
832 GFP T158D in the presence (36%) or absence (32%) of endogenous KIF22 **(Figure 9I)**.
833 Expression of KIF22-GFP (10%) or KIF22-GFP T158A (11%) in the presence of endogenous
834 KIF22 also resulted in a small increase in the percentage of cells with abnormally shaped nuclei
835 compared to control cells expressing GFP (5%). The expression of KIF22-GFP T158D
836 phenocopies the expression of KIF22-GFP T463D or KIF22-GFP with pathogenic mutations,
837 suggesting that dephosphorylation of T158 contributes to KIF22 inactivation in anaphase.

Figure 9

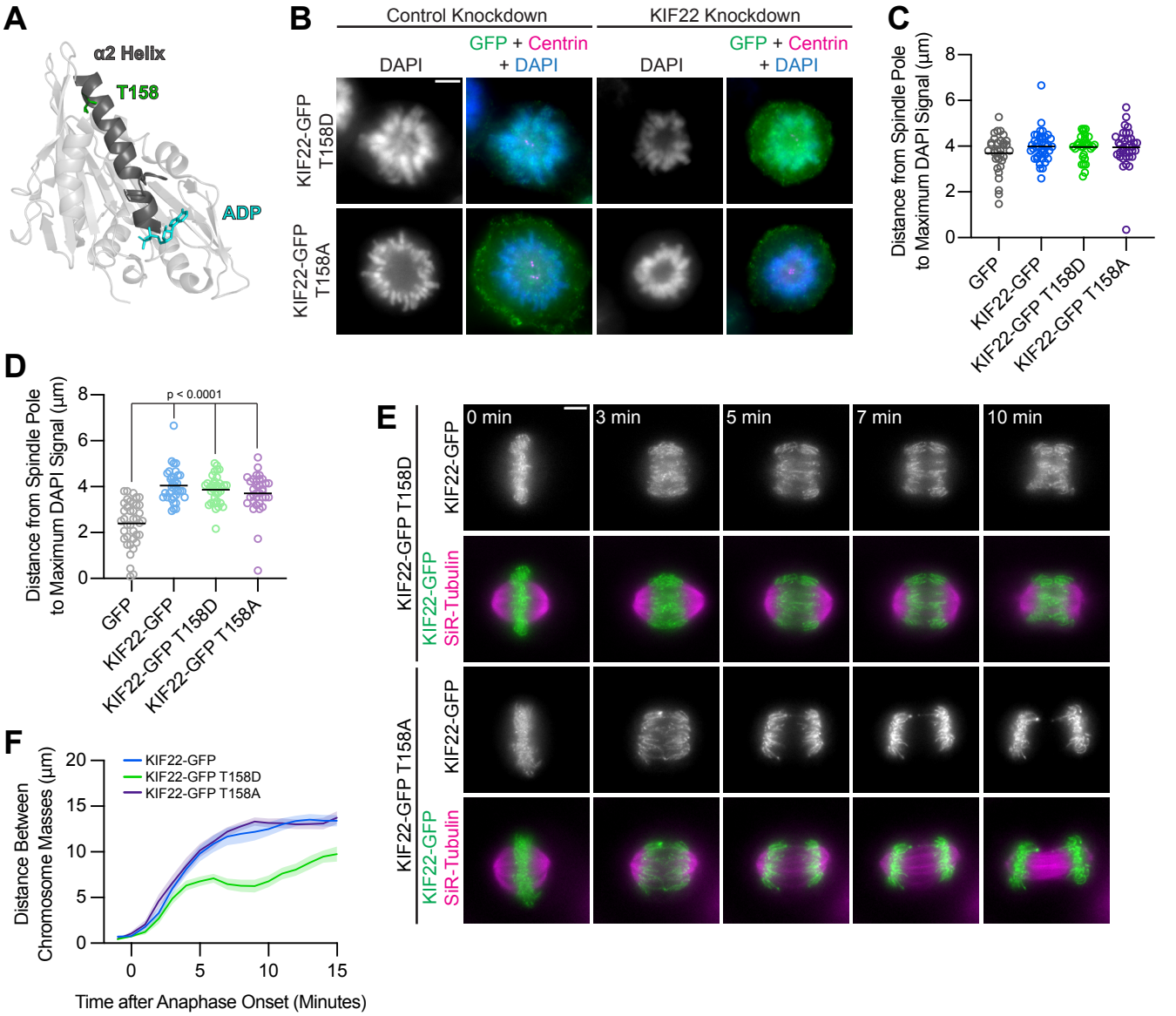
A
α2 Helix
T158
ADP
B
Control Knockdown
KIF22 Knockdown
DAPI
GFP + Centrin + DAPI
KIF22-GFP T158D
KIF22-GFP T158A
C
Distance from Spindle Pole to Maximum DAPI Signal (µm)
GFP
KIF22-GFP
KIF22-GFP T158D
KIF22-GFP T158A
D
p < 0.0001
E
0 min
3 min
5 min
7 min
10 min
KIF22-GFP
KIF22-GFP
SiR-Tubulin
F
KIF22-GFP
KIF22-GFP T158D
KIF22-GFP T158A
Distance Between Chromosome Masses (µm)
Time after Anaphase Onset (Minutes)
G
p = 0.0002
p < 0.0001
Distance at 7 Minutes (µm)
H
Nuclear Solidity
0.922
KIF22 Knockdown
I
p < 0.0001
p = 0.0009
p = 0.0029
% Nuclei with Solidity < 0.922

838 **Figure 9: Mimicking phosphorylation of T158 in the motor domain affects KIF22**
839 **inactivation.**
840 **A)** Location of amino acid T158 in the α2 helix of the KIF22 motor domain (PDB 6NJE). **(B)**
841 Immunofluorescence images of monopolar HeLa-Kyoto cells. KIF22-GFP was visualized using
842 an anti-GFP antibody. Fixed approximately 2-3 hours after treatment with monastrol and 24 hours
843 after siRNA transfection and treatment with doxycycline to induce expression. Scale bar 5 μm.
844 Images are representative of 3 or more experiments. **(C)** Distance from the spindle pole to the
845 maximum DAPI signal, a measure of relative polar ejection force level, in HeLa-Kyoto cell lines
846 expressing KIF22-GFP with phosphomimetic and phosphonull mutations at T158. 33 GFP, 40
847 KIF22-GFP, 31 KIF22-GFP T158D, and 36 KIF22-GFP T158A cells from 3 experiments. **(D)**
848 Distance from the spindle pole to the maximum DAPI signal in cells depleted of endogenous
849 KIF22 and expressing KIF22-GFP with phosphomimetic and phosphonull mutations at T158. 39
850 GFP, 35 KIF22-GFP, 34 KIF22-GFP T158D, and 34 KIF22-GFP T158A cells from 3 experiments.
851 For C-D, bars indicate means. p values from Brown-Forsythe and Welch ANOVA with Dunnett's
852 T3 multiple comparisons test. p values are greater than 0.05 for comparisons without a marked p
853 value. **(E)** Time-lapse images of dividing HeLa-Kyoto cells. Cells expressing KIF22-GFP T158D
854 exhibit recongression of the chromosomes during anaphase. Times indicate minutes after
855 anaphase onset. Images are maximum intensity projections in z through the entirety of the
856 spindle. Imaged approximately 18 hours after treatment with doxycycline to induce expression.
857 Scale bar 5 μm. Images are representative of 3 or more experiments. **(F)** Distance between
858 separating chromosome masses throughout anaphase in HeLa-Kyoto cells. Lines represent the
859 mean and the shaded area denotes SEM. 13 KIF22-GFP, 16 KIF22-GFP T158D, and 13 KIF22-
860 GFP T158A cells from 5 experiments. **(G)** Distance between separating chromosome masses 7
861 minutes after anaphase onset. Bars indicate medians. p values from Kruskal-Wallis test. p values
862 are greater than 0.05 for comparisons without a marked p value. 13 KIF22-GFP, 16 KIF22-GFP
863 T158D, and 13 KIF22-GFP T158A cells from 5 experiments. **(H)** Measured solidity of nuclei in
864 HeLa-Kyoto cell lines. Small circles represent the solidity of individual nuclei, and large circles
865 with black outlines indicate the median of each experiment. A dashed line marks a solidity value
866 of 0.922, the fifth percentile of solidity for control cells transfected with control siRNA and
867 expressing GFP. **(I)** Percentage of nuclei with abnormal shape, indicated by a solidity value less
868 than 0.922, the fifth percentile of control (control knockdown, GFP expression) cell solidity. A chi-
869 square test of all data produced a p value < 0.0001. Plotted p values are from pairwise post-hoc
870 chi-square tests comparing control (control knockdown, GFP expression) cells to each other

871 condition. Applying the Bonferroni correction for multiple comparisons, a p value of less than
872 0.00714 was considered significant. p values are greater than 0.00714 for comparisons without a
873 marked p value. Data in (H) and (I) represent 514 GFP control knockdown, 418 GFP KIF22
874 knockdown, 613 KIF22-GFP control knockdown, 584 KIF22-GFP KIF22 knockdown, 644 KIF22-
875 GFP T158D control knockdown, 432 KIF22-GFP T158D KIF22 knockdown, 477 KIF22-GFP
876 T158A control knockdown, and 427 KIF22-GFP T158A KIF22 knockdown cells from 3
877 experiments.

Supplemental Figure 6

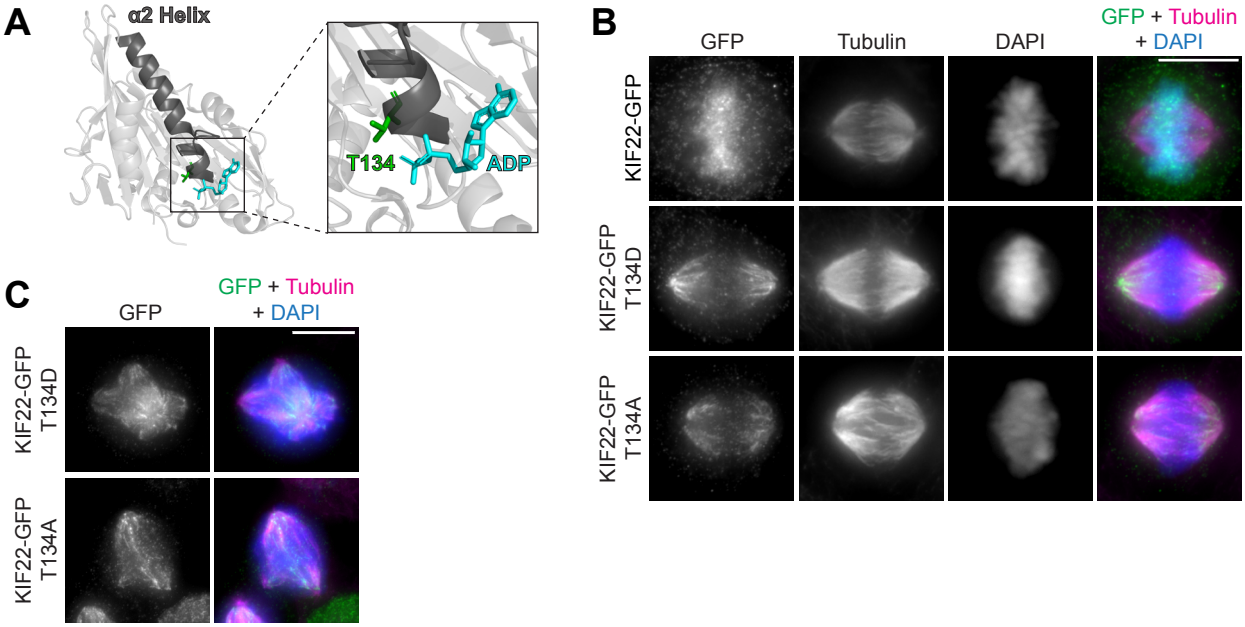

878 **Supplemental Figure 6: Mimicking phosphoregulation of T134 disrupts KIF22 localization.**
879 **(A)** Location of amino acid T134 in the α2 helix of the KIF22 motor domain (PDB 6NJE). **(B)**
880 Immunofluorescence images of HeLa-Kyoto cells expressing KIF22-GFP constructs in
881 metaphase. KIF22-GFP was visualized using an anti-GFP antibody. Images are maximum
882 intensity projections in z. Fixed approximately 24 hours after treatment with doxycycline to induce
883 expression. Scale bar 10 μm. **(C)** Immunofluorescence images of multipolar HeLa-Kyoto cells
884 expressing KIF22-GFP T134D or KIF22-GFP T134A. Images are maximum intensity projections
885 in z. Fixed approximately 24 hours after treatment with doxycycline to induce expression. Scale
886 bar 10 μm.

Figure 10

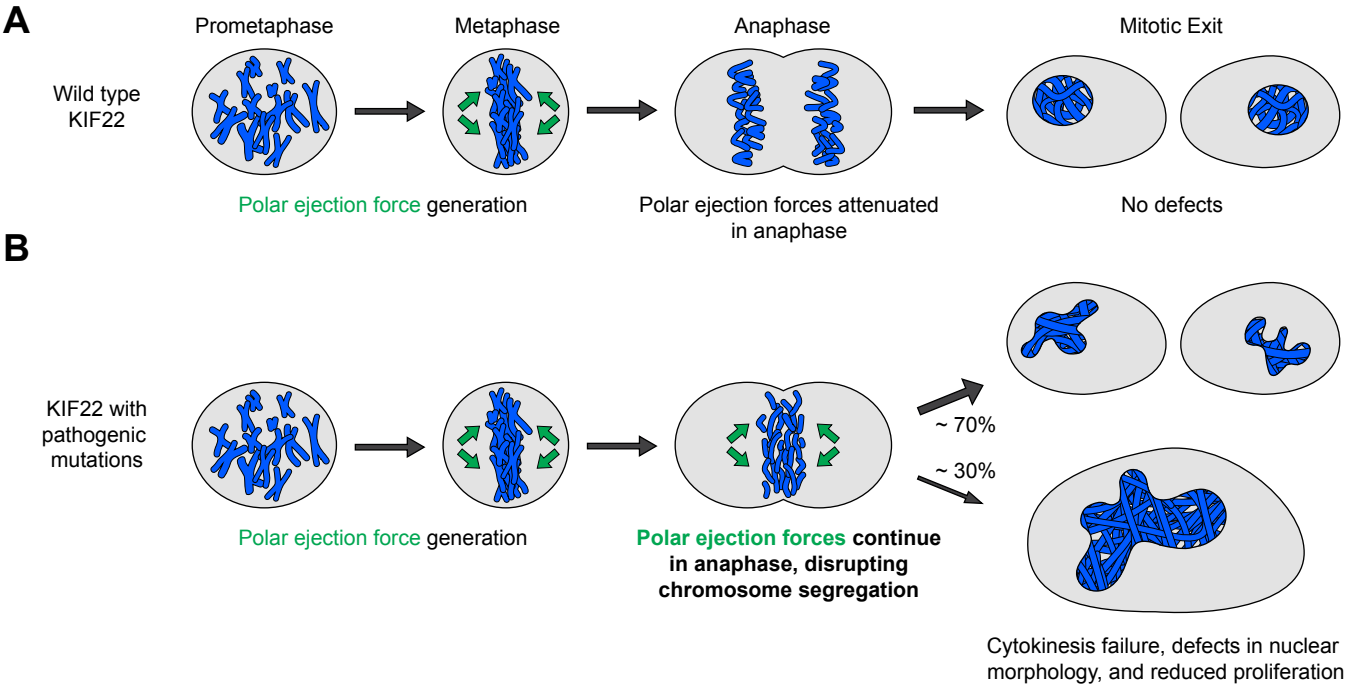
A
Prometaphase
Metaphase
Anaphase
Mitotic Exit
Wild type KIF22
Polar ejection force generation
Polar ejection forces attenuated in anaphase
No defects
B
KIF22 with pathogenic mutations
~ 70%
~ 30%
Polar ejection force generation
Polar ejection forces continue in anaphase, disrupting chromosome segregation
Cytokinesis failure, defects in nuclear morphology, and reduced proliferation

887 **Figure 10: Pathogenic mutations disrupt the anaphase, but not prometaphase, function of**
888 **KIF22.**
889 **(A)** Wild type KIF22 generates polar ejection forces to contribute to chromosome congression
890 and alignment in prometaphase. In anaphase, KIF22 inactivation results in the attenuation of polar
891 ejection forces (green arrows), allowing chromosomes to segregate toward the poles. Daughter
892 cells form regularly shaped nuclei and continue to proliferate. **(B)** In cells expressing KIF22 with
893 pathogenic (P148L, P148S, R149L, R149Q, V475G) or phosphomimetic (T158D, T463D)
894 mutations, prometaphase proceeds as in cells expressing wild type motor. Mutant KIF22 is
895 capable of polar ejection force generation. In anaphase, KIF22 fails to inactivate, resulting in
896 continued generation of polar ejection forces, which disrupts anaphase chromosome segregation.
897 Daughter cells exhibit nuclear morphology defects. In about 30% of cells expressing KIF22-GFP
898 R149Q or KIF22-GFP V475G, cytokinesis fails, and proliferation rates are reduced.

DISCUSSION

We have determined that pathogenic mutations in KIF22 disrupt anaphase chromosome segregation, causing chromosome recongression, nuclear morphology defects, reduced proliferation, and, in a subset of cells, cytokinesis failure. Wild type KIF22 is inactivated in anaphase (Soeda et al., 2016), resulting in an attenuation of polar ejection forces, which allows chromosomes to move towards the spindle poles **(Figure 9A)**. The phenotypes we observe in cells expressing KIF22-GFP with pathogenic mutations are consistent with KIF22 remaining active in anaphase **(Figure 9B)**. Polar ejection forces could cause recongression by continuing to push chromosomes away from the spindle poles during anaphase A and disrupting spindle elongation during anaphase B. These forces result in aberrant positioning of chromosomes during telophase and cytokinesis, which could cause the nuclear morphology defects and cytokinesis failure we observe in cells expressing mutant KIF22-GFP. Consistent with this model, mimicking phosphorylation of T463 to prevent KIF22 inactivation in anaphase phenocopies the effects of pathogenic mutations. Thus, we conclude that pathogenic mutations result in a gain of KIF22 function, which aligns with findings that KIF22 mutations are dominant in heterozygous patients (Boyden et al., 2011; Min et al., 2011; Tüysüz et al., 2014). The effects of pathogenic mutations on chromosome movements in anaphase are consistent with observations of chromosome recongression in cells with altered CDK1 activity (Su et al., 2016; Wolf et al., 2006) or altered tail structure (Soeda et al., 2016). Our work additionally demonstrates the involvement of the motor domain α2 helix in this process and the consequences of recongression on cytokinesis, daughter cell nuclear morphology, and proliferation.

Mutations in both the motor domain (P148L, P148S, R149L, and R149Q) and the coiled-coil domain (V475G) of KIF22 disrupt chromosome segregation in a manner consistent with a failure of KIF22 inactivation in anaphase. Additionally, mimicking phosphorylation of T158 in the motor domain or T463 in the tail also disrupts chromosome segregation. These findings demonstrate that the motor domain α2 helix participates in the process of KIF22 inactivation, adding to studies that demonstrate that deletion of the tail microtubule binding domain and deletion or disruption of the coiled-coil domain prevent the inactivation of KIF22 in anaphase (Soeda et al., 2016).

The physical mechanism of KIF22 inactivation is unknown, and our results can be interpreted in the context of several models, which are not mutually exclusive. Previous work has proposed that the tail of KIF22 may interact with microtubules to suspend polar ejection force generation (Soeda et al., 2016). In this framework, the mutation in the tail of KIF22 (V745G) could disrupt anaphase chromosome segregation by altering this interaction with microtubules. Whether

933 or how the α2 helix could contribute to this mechanism is less clear. The α2 helix faces away from
934 the surface of the microtubule, and we would not predict that mutations in this structure would
935 directly alter the association of the motor domain with the microtubule. It is possible that this region
936 of the motor domain could facilitate or strengthen an interaction between the tail and the
937 microtubule surface indirectly.

938 Alternatively, given that mutations in the tail and motor domain of KIF22 both disrupt
939 chromosome segregation, the tail and motor domain may interact to inactivate the motor. Head-
940 tail autoinhibition is a known regulatory mechanism of other members of the kinesin superfamily
941 (Blasius et al., 2021; Coy, Hancock, Wagenbach, & Howard, 1999; Espeut et al., 2008; Friedman
942 & Vale, 1999; Hammond, Blasius, Soppina, Cai, & Verhey, 2010; Hammond et al., 2009; Imanishi,
943 Endres, Gennerich, & Vale, 2006; Ren et al., 2018; Verhey & Hammond, 2009; Verhey et al.,
944 1998), and disruption of autoinhibition can be a mechanism of disease pathogenesis (Asselin et
945 al., 2020; Bianchi et al., 2016; Blasius et al., 2021; Cheng et al., 2014; Pant et al., 2022; van der
946 Vaart et al., 2013). Mutations in either the tail or motor domain could disrupt this interaction,
947 preventing KIF22 inactivation in anaphase. Dephosphorylation of both T463 in the tail and T158
948 in the motor domain could facilitate this interaction.

949 Rather than physically interacting with the motor domain, it is also possible that structural
950 changes in the tail of KIF22 could have allosteric effects on the motor domain. An allosteric
951 mechanism by which conformational changes are propagated down the stalk to the motor domain
952 has recently been proposed to contribute to the inactivation of kinesin-1 motors by kinesin light
953 chain, which binds the tail (Chiba, Ori-McKenney, Niwa, & McKenney, 2021). KIF22 inactivation
954 may be caused by altered motor domain mechanochemistry, which changes in the tail could affect
955 allosterically and modification of α2 could affect directly. This could explain the effect of tail and
956 motor domain mutations, as well as the effects of mimicking tail and motor domain
957 phosphorylation, on KIF22 activity.

958 An additional consideration is that pathogenic mutations may affect the inactivation of
959 KIF22 in anaphase by altering phosphoregulation of KIF22 activity. If mutations prevented the
960 dephosphorylation of T158 and T463 in anaphase this could cause anaphase recongression.
961 However, addition of a phosphonull T463A mutation to KIF22 with coiled-coil or microtubule
962 binding domain deletions does not rescue anaphase chromosome recongression defects (Soeda
963 et al., 2016), suggesting that the role of the KIF22 tail in motor inactivation is not only to facilitate
964 dephosphorylation of T463. Future studies using structural approaches will be required to
965 distinguish between these possible mechanisms.

966 The regulation of the motor domain α2 helix in KIF22 inactivation may inform our
967 understanding of additional kinesin motors, as amino acids P148 and R149 are conserved in a
968 number of members of the kinesin superfamily **(Figure 1D)**. Similarly, phosphorylation or
969 acetylation of amino acids in the α2 helix has been reported for members of the kinesin-3 (KIF13A
970 S134) (Dephoure et al., 2008), kinesin-5 (KIF11 Y125, K146) (Bickel et al., 2017; Choudhary et
971 al., 2009), kinesin-6 (KIF20B S182, KIF23 S125) (Hegemann et al., 2011; Sharma et al., 2014;
972 Shiromizu et al., 2013), and kinesin-14 (KIFC3 S557) (Sharma et al., 2014) families.
973 Phosphorylation of Y125 (Bickel et al., 2017) and acetylation of K146 (Muretta et al., 2018) in
974 KIF11 (Eg5) have been shown to modulate motor activity, and the functions of the remaining
975 reported post-translation modifications in the α2 helix are yet to be characterized. Acetylation of
976 KIF11 at K146 increases the stall force of the motor and slows anaphase spindle pole separation
977 (Muretta et al., 2018). This post-translational modification represents a mechanism by which the
978 activity of KIF11 could be regulated at the metaphase to anaphase transition to generate sliding
979 forces for spindle assembly in prometaphase and control spindle pole separation in anaphase,
980 analogous to how post-translational modifications of KIF22 regulate motor activity to ensure both
981 chromosome congression and alignment in prometaphase and chromosome segregation in
982 anaphase.
983 While chromosomes in some cells, particularly those expressing KIF22-GFP at high
984 levels, completely failed to segregate and decondensed in the center of the spindle, most cells
985 demonstrated chromosome recongression wherein poleward motion of chromosomes begins, but
986 then chromosomes switch direction and move anti-poleward. These dynamics may be due to
987 differences in microtubule density closer to the poles compared to the center of the spindle. This
988 model is consistent with work demonstrating that in monopolar spindles, poleward movement of
989 chromosomes is limited by chromosomes reaching a threshold density of microtubules at which
990 polar ejection forces are sufficient to cause chromosomes to switch to anti-poleward movement
991 (Cassimeris, Rieder, & Salmon, 1994). We observed that chromosomes on the periphery of the
992 spindle remain closer to the poles while central chromosomes are pushed further away from the
993 poles during recongression in cells expressing KIF22-GFP with pathogenic mutations. This could
994 also be explained by the central chromosomes encountering a higher density of microtubules,
995 and KIF22 bound to these chromosomes therefore generating higher levels of polar ejection
996 forces. In addition, this mechanism is consistent with observations that oscillations of peripheral
997 chromosomes are reduced compared to chromosomes at the center of the spindle (Cameron et
998 al., 2006; Cimini, Cameron, & Salmon, 2004; Civelekoglu-Scholey et al., 2013; Stumpff, Dassow,

Wagenbach, Asbury, & Wordeman, 2008), which could also be explained by reduced peripheral microtubule density limiting peripheral polar ejection force generation.

Our assessment of the relative trajectories of chromosomes, centromeres, and spindle poles offers insight into the relative magnitudes of polar ejection forces and other anaphase forces. Expression of KIF22-GFP with pathogenic mutations did not alter the distance between centromeres and spindle poles, indicating that while anaphase polar ejection forces altered the position of chromosome arms within the spindle, these forces were not sufficient to prevent the shortening of k-fibers. However, the expression of mutant KIF22-GFP did alter the movements of the spindle poles, allowing assessment of the relative magnitude of polar ejection forces compared to the forces generated by the sliding of antiparallel spindle microtubules to separate the spindle poles in anaphase (Brust-Mascher, Civelekoglu-Scholey, Kwon, Mogilner, & Scholey, 2004; Fu et al., 2009; Nislow, Lombillo, Kuriyama, & McIntosh, 1992; Sawin, LeGuellec, Philippe, & Mitchison, 1992; Straight, Sedat, & Murray, 1998; Tanenbaum et al., 2009; van Heesbeen, Tanenbaum, & Medema, 2014; Vukušić, Buđa, & Tolić, 2019; Vukušić, Ponjavić, Buđa, Risteski, & Tolić, 2021). In cells expressing mutant KIF22-GFP, spindle pole separation stalled, and poles moved closer to one another during anaphase chromosome recongression. This suggests that the polar ejection forces collectively generated by mutant KIF22 motors are of greater magnitude than the forces sliding the spindle poles apart during anaphase B. Although it is important to note that this phenotype was observed with moderate overexpression of mutant KIF22, the observed effects on spindle pole separation underscore the importance of KIF22 inactivation, and imply that reducing polar ejection forces is required for both anaphase A and anaphase B. This force balance may differ between cell types, as tail domain deletions that alter chromosome movements do not disrupt anaphase B in mouse oocyte meiosis (Soeda et al., 2016).

Patients with mutations in KIF22 exhibit defects in skeletal development. The pathology observed in the patient heterozygous for the V475G mutation differs from those seen in SEMDJL2 patients with motor domain mutations **(Figure 1E, 1F)** (Boyden et al., 2011; Min et al., 2011; Tüysüz et al., 2014). However, a meaningful comparison of pathologies between patients is limited both by the fact that only a single patient with a mutation in the tail of KIF22 has been identified, and by the considerable variation in clinical presentation between patients with motor domain mutations, even between patients with the same point mutation (Boyden et al., 2011; Min et al., 2011; Tüysüz et al., 2014). The defects in chromosome segregation we observed in cells expressing mutant KIF22-GFP may contribute to skeletal developmental pathogenesis. Mutations could cause reduced proliferation of growth plate chondrocytes, which in turn could limit bone growth. Disrupting cytokinesis in the growth plate causes shorter bones and stature in mice (Gan

1033 et al., 2019), and mutations in KIF22 could affect development via this mechanism. The presence
1034 of pathologies in other cartilaginous tissues, including the larynx and trachea, in patients with
1035 mutations in the motor domain of KIF22 (Boyden et al., 2011) is also consistent with a disease
1036 etiology based in aberrant chondrocyte proliferation. Defects in mitosis could result in tissue-
1037 specific patient pathology based on differences in force balance within anaphase spindles in
1038 different cell types arising from different expression or activity levels of mitotic force generators or
1039 regulators. Growth plate chondrocytes, particularly, are organized into columns and must divide
1040 under geometric constraints (Dodds, 1930), which could increase sensitivity to anaphase force
1041 imbalances. Additionally, we cannot exclude the possibility that these mutations may affect the
1042 function of interphase cells, which could affect development via a mechanism independent from
1043 the effects of the mutations on mitosis. Future work will be required to distinguish among these
1044 possible explanations.
1045

1046 **MATERIALS AND METHODS**

1047 **Patient assessment**

1048 Clinical exome sequencing was performed by the Department of Laboratory Medicine and
1049 Pathology at Mayo Clinic in Rochester, Minnesota, USA as previously described (Cousin et al.,
1050 2019). Carbohydrate deficient transferrin testing for congenital disorders of glycosylation was
1051 performed at Mayo Clinic Laboratories, Rochester, Minnesota, USA (Lefeber, Morava, & Jaeken,
1052 2011).
1053

1054 **Cell culture**

1055 HeLa-Kyoto and RPE-1 cell lines were grown in Minimum Essential Media α (Gibco
1056 #12561-056) supplemented with 10% fetal bovine serum (Gibco #16000-044) at 37°C with 5%
1057 CO_2. Cell lines were validated by short tandem repeat (STR) DNA typing using the Promega
1058 GenePrint 10 System according to the manufacturer's instructions (Promega #B9510). Cells were
1059 cryopreserved in Recovery Cell Culture Freezing Medium (Gibco #12648-010). HeLa-Kyoto and
1060 RPE-1 acceptor cell lines for recombination (both gifts from Ryoma Ohi, University of Michigan)
1061 were maintained in media supplemented with 10 μg/mL blasticidin (Thermo Fisher Scientific
1062 #R21001).
1063

1064 **Transfection**

1065 siRNA transfection was performed using Lipofectamine RNAiMax Transfection Reagent
1066 (Thermo Fisher Scientific #13778150) in Opti-MEM Reduced Serum Media (Gibco #31985-062).

1067 KIF22 was targeted for siRNA-mediated depletion using a Silencer Validated siRNA (Ambion
1068 #AM51331, sense sequence GCUGCUCUCUAGAGAUUGCTT). Control cells were transfected
1069 with Silencer Negative Control siRNA #2 (Ambion #AM4613). DNA transfections were performed
1070 using Lipofectamine LTX (Thermo Fisher Scientific #15338100) in Opti-MEM Reduced Serum
1071 Media (Gibco #31985-062).
1072
1073 **Plasmids**
1074 Plasmids related to the generation of inducible cell lines are described in Table 1. A C-
1075 terminally tagged KIF22-GFP plasmid was constructed by adding EcoRI and KpnI sites to the
1076 KIF22 open reading frame (from pJS2161 (Stumpff et al., 2012)), performing a restriction digest,
1077 and ligating the products into a digested pEGFP-N2 vector (Clontech) (pAT4206). Site-directed
1078 mutagenesis was performed to add silent mutations for siRNA resistance (pAT4226). The open
1079 reading frame from pAT4226 and the pEM791 vector (Khandelia, Yap, & Makeyev, 2011) were
1080 amplified and combined using Gibson Assembly (New England BioLabs) to generate a plasmid
1081 for recombination-mediated construction of inducible cell lines (pAT4250). Site-directed
1082 mutagenesis was performed on pAT4250 to generate plasmids encoding KIF22-GFP P148L,
1083 P148S, R149L, R149Q, V475G, T463D, T463A, T134D, T158D, and T158A for recombination. A
1084 plasmid encoding KIF22-GFP T134A for recombination was generated using Gibson Assembly
1085 of a synthesized DNA fragment (Thermo Fisher Scientific) and pAT4250. See Table 1 for primer
1086 sequences.
1087 The mCh-CAAX plasmid was a gift from Alan Howe (University of Vermont). The mCh-
1088 NLS plasmid was generated by Michael Davidson and obtained from Addgene (mCh-Nucleus-7,
1089 #55110). The pericentrin-RFP plasmid (Gillingham & Munro, 2000) was a gift from Sean Munro
1090 (MRC Laboratory of Molecular Biology). The CENPB-mCh plasmid (D. Liu et al., 2010) was
1091 generated by Michael Lampson and obtained from Addgene (#45219).
1092
1093 **Generation of inducible cell lines**
1094 Inducible cell lines were generated using recombination-mediated cassette exchange as
1095 previously described (Khandelia et al., 2011). Briefly, plasmids (see Table 1) encoding siRNA-
1096 resistant KIF22-GFP constructs were cotransfected with a plasmid encoding nuclear-localized
1097 Cre recombinase (pEM784) into HeLa-Kyoto (Sturgill, Norris, Guo, & Ohi, 2016) or RPE-1
1098 acceptor cells using Lipofectamine LTX transfection (Thermo Fisher Scientific #15338100). For
1099 HeLa-Kyoto cell lines, 24 hours after transfection cells were treated with 1 μg/mL puromycin
1100 (Thermo Fisher Scientific #A11139-03) for 48 hours, then 2 μg/mL puromycin for 48 hours for

1101 more stringent selection, and finally 1 μg/mL puromycin until puromycin-sensitive cells were
1102 eliminated. Selection of RPE-1 cells was accomplished via treatment with 5 μg/mL puromycin for
1103 48 hours beginning 24 hours after transfection, then 10 μg/mL puromycin for 48 hours, and finally
1104 5 μg/mL puromycin until puromycin-sensitive cells were eliminated. Inducible cell lines were
1105 maintained in puromycin (HeLa-Kyoto 1 μg/mL, RPE-1 5 μg/mL) for continued selection. To
1106 confirm the sequence of inserted DNA in the selected cell populations, genomic DNA was
1107 extracted using the QIAmp DNA Blood Mini Kit (Qiagen #51106) and subjected to sequencing
1108 (Eurofins). Expression of inserted DNA sequences was induced via treatment with 2 μg/mL
1109 doxycycline (Thermo Fisher Scientific #BP26531).
1110
1111 **Immunofluorescence**
1112 For fixed cell imaging, cells were grown on 12 mm glass coverslips in 24-well plates. Cells
1113 were fixed in 1% paraformaldehyde in ice-cold methanol for 10 minutes on ice. Cells were blocked
1114 for 1 hour using 20% goat serum (Gibco #16210-064) in antibody dilution buffer (AbDil, 1% bovine
1115 serum albumin (Sigma Aldrich #B4287), 0.1% Triton X-100 (Sigma Aldrich #93443), 0.02%
1116 sodium azide (Fisher Scientific #BP9221) in TBS) and incubated with the following primary
1117 antibodies for one hour at room temperature: mouse anti-α-tubulin (DM1α) 1:500 (Millipore Sigma
1118 #T6199), rat anti-tubulin clone YL1/2 1:1500 (Millipore Sigma #MAB1864), rabbit anti-KIF22 1:500
1119 (GeneTex #GTX112357), mouse anti-centrin 1:500 (Millipore Sigma #04-1624), or rabbit anti-
1120 GFP 1:1000 (Invitrogen #A11121). Cells were incubated with secondary antibodies conjugated to
1121 AlexaFluor 488, 594, or 647 (Invitrogen Molecular Probes #A11034, A11037, A21245, A11029,
1122 A11032, A21236, A11007) for one hour at room temperature. All incubations were performed on
1123 an orbital shaker. Coverslips were mounted on slides using Prolong Gold mounting medium with
1124 DAPI (Invitrogen Molecular Probes #P36935).
1125
1126 **Microscopy**
1127 Images were acquired using a Nikon Ti-E or Ti-2E inverted microscope driven by NIS
1128 Elements software (Nikon Instruments). Images were captured using a Clara cooled charge-
1129 coupled device (CCD) camera (Andor) or Prime BSI scientific complementary metal-oxide-
1130 semiconductor (sCMOS) camera (Teledyne Photometrics) with a Spectra-X light engine
1131 (Lumencore). Samples were imaged using Nikon objectives Plan Apo 40X 0.95 numerical
1132 aperture (NA), Plan Apo λ 60X 1.42 NA, and APO 100X 1.49 NA. For live imaging, cells were
1133 imaged in CO_2-independent media (Gibco #18045-088) supplemented with 10% fetal bovine

1134 serum (Gibco #16000-044) in a 37º C environmental chamber. Images were processed and
1135 analyzed using Image J/FIJI (Schindelin et al., 2012; Schneider, Rasband, & Eliceiri, 2012).
1136
1137 **KIF22-GFP expression level quantitation**
1138 HeLa-Kyoto or RPE-1 cells were treated with 2 μg/mL doxycycline to induce expression
1139 and transfected with control or KIF22 siRNA approximately 24 hours prior to fixation. Metaphase
1140 cells were imaged for measurement of KIF22 expression levels. Measurements of KIF22
1141 immunofluorescence intensity were made in a background region of interest (ROI) containing no
1142 cells and an ROI representing the chromosomes, identified by thresholding DAPI signal. The
1143 mean background subtracted KIF22 signal on the chromosomes was calculated by subtracting
1144 the product of the mean background intensity and the chromosome ROI area from the
1145 chromosome ROI integrated density and dividing by the area of the chromosome ROI. KIF22
1146 intensities were normalized to the mean KIF22 intensity in control cells (control knockdown,
1147 uninduced) in each experimental replicate.
1148
1149 **Metaphase chromosome spreads**
1150 RPE-1 cells were grown in 60 mm dishes for approximately 24 hours. Media was
1151 exchanged to fresh growth media for 2 hours to promote mitosis. Cells were arrested in 0.02
1152 μg/mL colcemid (Gibco KaryoMAX #15212012) for three hours at 37°C, then trypsinized, pelleted,
1153 and gently re-suspended in 500 μL media. 5 mL 0.56% KCl hypotonic solution was added
1154 dropwise to the cell suspension, which was then incubated for 15 minutes in a 37°C water bath.
1155 Cells were pelleted, gently resuspended, and fixed via the addition of 1 mL ice-cold 3:1
1156 methanol:glacial acetic acid. Cells were pelleted and resuspended in fixative an additional three
1157 times, then stored at -20°C. Metaphase chromosome spreads were prepared by humidifying the
1158 surface of glass slides by exposing them to the steam above a 50°C water bath, placing the slides
1159 at an angle relative to the work surface, and dropping approximately 100 μL of ice-cold cell
1160 suspension onto the slide from a height of approximately one foot. Slides were dried on a hot
1161 plate, then covered with Prolong Gold mounting medium with DAPI (Invitrogen Molecular Probes
1162 #P36935) and sealed.
1163
1164 **Fluorescence recovery after photobleaching**
1165 HeLa-Kyoto cells were seeded in glass-bottom 35 mm dishes (Greiner Bio-One #627975
1166 and #627965) and treated with 2 μg/mL doxycycline to induce expression 18-24 hours before

1167 imaging. Cells were imaged at 5 second intervals for 25 seconds before bleaching, photobleached
1168 using a point-focused 405 nm laser, and imaged at 20 second intervals for 10 minutes after
1169 bleaching. Fluorescence intensities in bleached, unbleached, and background regions of each
1170 frame were measured using a circular ROI, area 0.865 μm^2. For interphase and metaphase cells,
1171 unbleached measurements were made on the opposite side of the nucleus or chromosome mass
1172 as the bleached measurements. For anaphase cells, one segregating chromosome mass was
1173 bleached, and unbleached measurements were made on the opposite chromosome mass.
1174 Background intensities, measured in cell-free area, were subtracted from bleached and
1175 unbleached intensities. Background-subtracted intensities were normalized to the intensity of the
1176 first frame imaged.
1177
1178 **Polar ejection force assay**
1179 HeLa-Kyoto cells were treated with 2 μg/mL doxycycline to induce expression and
1180 transfected with control or KIF22 siRNA approximately 24 hours prior to fixation. Cells were
1181 arrested in 100 μM monastrol (Selleckchem #S8439) for 2-3 hours before fixation. Monopolar
1182 mitotic cells oriented perpendicular to the coverslip were imaged at the focal plane of the spindle
1183 pole for polar ejection force measurements. A circular ROI with a 12.5 μm radius was centered
1184 around the spindle pole of each cell, and the radial profile of DAPI signal intensity at distances
1185 from the pole was measured (Radial Profile Plot plugin, https://imagej.nih.gov/ij/plugins/radial-
1186 profile.html). The distance from the pole to the maximum DAPI signal was calculated for each cell
1187 as a measure of relative polar ejection forces (Thompson, Vandal, & Stumpff, 2022).
1188
1189 **Analyses of anaphase chromosome segregation**
1190 HeLa-Kyoto or RPE-1 cells were treated with 2 μg/mL doxycycline to induce expression
1191 approximately 18 hours before imaging. For HeLa-Kyoto cells, media was exchanged to CO_2-
1192 indpendent media containing 2 μg/mL doxycycline and 100 nM SiR-Tubulin (Spirochrome
1193 #SC002) approximately 1-1.5 hours before imaging. For RPE-1 cells, media was exchanged to
1194 CO_2-indpendent media containing 2 μg/mL doxycycline, 20-100 nM SiR-Tubulin (Spirochrome
1195 #SC002), and 10 μM verapamil (Spirochrome #SCV01) approximately 1.5-3 hours before
1196 imaging. Cells were imaged at 1 minute time intervals. Distances between segregating
1197 chromosome masses were measured by plotting the KIF22-GFP signal intensity along a line
1198 drawn through both spindle poles (macro available at https://github.com/StumpffLab/Image-
1199 Analysis). This data set was split at the center distance to generate two plots, each representing

1200 one half-spindle/segregating chromosome mass. The distance between the maximum of each
1201 intensity plot was calculated using MATLAB (Mathworks, Version R2018a) (script available at
1202 https://github.com/StumpffLab/Image-Analysis). To assess the broadness of segregating
1203 chromosome masses in cells expressing KIF22-GFP T463A, a Gaussian curve was fit to the same
1204 intensity plots and the full width at half maximum was calculated in MATLAB.

1205 To measure the movements of spindle poles and kinetochores in anaphase, HeLa-Kyoto
1206 cells were seeded in glass-bottom 24-well plates (Cellvis #P24-1.5H-N) and cotransfected with
1207 PCM-RFP and mCh-CENPB using Lipofectamine LTX (Thermo Fisher Scientific #15338100)
1208 approximately 24 hours before imaging. Cells were treated with 2 μg/mL doxycycline to induce
1209 expression approximately 12-18 hours before imaging. Cells were imaged at 20 second time
1210 intervals. To more clearly visualize spindle poles and kinetochores, images of PCM-RFP and
1211 mCh-CENPB signal were background subtracted by duplicating each frame, applying a gaussian
1212 blur (sigma 30 pixels), and subtracting this blurred image from the original. For each frame, a line
1213 was drawn between spindle poles (PCM-RFP signal) to measure the distance between them, and
1214 the intensity of KIF22-GFP and mCh-CENPB along this line was plotted. These data sets were
1215 split at the center distance to generate two plots, and the distance between plot maxima and the
1216 distance from maxima to the spindle poles were calculated using MATLAB (scripts available at
1217 https://github.com/StumpffLab/Image-Analysis).

1218

1219 **Assessment of cytokinesis failure**

1220 To visualize cell boundaries, HeLa-Kyoto cells were transfected with mCh-CAAX using
1221 Lipofectamine LTX approximately 24-32 hours before imaging and treated with 2 μg/mL
1222 doxycycline approximately 8 hours before imaging. Cells were imaged at 3-minute intervals. Cells
1223 were scored as failing cytokinesis if the product of mitosis was a single cell with a single boundary
1224 of mCh-CAAX signal.

1225

1226 **Nuclear morphology quantification**

1227 HeLa-Kyoto or RPE-1 cells were treated with 2 μg/mL doxycycline to induce expression
1228 approximately 24 hours before fixation. Nuclear solidity was measured for each interphase
1229 nucleus in each imaged field. The 5th percentile of solidity for control cells (transfected with control
1230 siRNA and expressing GFP) was used as a threshold below which nuclear solidity was considered
1231 abnormal.

1232 To assess the ability of nuclei to retain nuclear-localized proteins, cells were transfected
1233 with mCh-NLS using Lipofectamine LTX approximately 24-32 hours before imaging and treated

1234 with 2 μg/mL doxycycline approximately 8 hours before imaging. Cells were imaged at 3-minute
1235 intervals during and after division, and the presence of mCh-NLS signal in all nuclear structures
1236 (KIF22-GFP positive regions) was assessed.
1237
1238 **Assessment of spindle dependence of nuclear morphology defects**
1239 To assess whether nuclear morphology defects caused by KIF22 depend on force
1240 generation within the mitotic spindle, cells were treated with 2 μg/mL doxycycline approximately
1241 8 hours before imaging, SPY595-DNA (1X per manufacturer's instructions) (Spirochrome
1242 #SC301) approximately 1.5-2 hours before imaging, and 500 nM nocodazole (Selleckchem
1243 #S2775) and 900 nM reversine (Cayman Chemical #10004412) approximately 0.5-1 hour before
1244 imaging. Cells were imaged at 5-minute intervals. Nuclear solidity was measured 15 minutes
1245 before chromosome condensation and 100 minutes after chromosome decondensation.
1246
1247 **Proliferation assay**
1248 HeLa-Kyoto cells were seeded in a 96-well plate and treated with 2 μg/mL doxycycline to
1249 induce expression or transfected with KIF22 siRNA approximately eight hours before the first
1250 assay timepoint. Automated bright field imaging using a Cytation 5 Cell Imaging Multi-Mode
1251 Reader (Biotek) (4X Plan Fluorite 0.13 NA objective (Olympus)) driven by Gen5 software (Biotek)
1252 was used to measure cell proliferation (Marquis et al., 2021). Images were collected every 4 hours
1253 for 96 hours. Gen5 software was used to process images and count the number of cells in each
1254 imaged field. Cell counts were normalized to the cell count in the first image acquired at time 0.
1255 Only wells with first frame cell counts between 10,000 and 20,000 were analyzed to account for
1256 the effects of cell density. Fold change at 96 hours was calculated by dividing the cell count at 96
1257 hours by the cell count at time 0. Predicted cell counts at 48 hours were calculated using an
1258 experimentally determined doubling time of 20.72 hours for the control case where all cells divide
1259 ($Cells_T = 2^{(\frac{T}{20.72})}$), the case where nuclear morphology defects limit proliferation and 60% of cells
1260 do not divide ($Cells_T = 1.4^{(\frac{T}{20.72})}$), and the case where cytokinesis failure limits proliferation and
1261 30% of cells do not divide ($Cells_T = 1.7^{(\frac{T}{20.72})}$).
1262
1263 **Statistical analyses**
1264 Statistical tests were performed using GraphPad Prism software (GraphPad Software,
1265 Inc.), version 9.2.0. Specific statistical tests and n values for reported data are indicated in the
1266 figure legends. All data represent a minimum of three independent experiments.

1267 **Table 1**

Plasmid	Description	Primers (5' to 3', Fw: Forward, Rev: Reverse)	Source
pEM784	nlCre recombinase	NA	Khandelia 2011 PMID 21768390
pEM791	EGFP for recombination	NA	Khandelia 2011 PMID 21768390
pJS2161	GFP-KIF22	NA	Stumpff 2012 PMID 22595673
pAT4206	KIF22-GFP	Fw: TACGTGGAATTCCACCATGGCCGCGGGCGGCTCGA Rev: GTGACTGGTACCTGGAGGCGCCACAGCGCTGGC	This study
pAT4226	KIF22-GFP, siRNA resistant	Fw:pGGGCATGGACAGCTGCTCACTCGAAATCGCTAACTGGAGGA ACCAC Rev:pGTGGTTCCTCCAGTTAGCGATTTCGAGTGAGCAGCTGTCCA TGCCC	This study
pAT4250	KIF22-GFP, siRNA resistant, for recombination	Fragment Fw: CTGGGCACCACCATGGCCGCG Fragment Rev: GCTAGCTCGATTACTTGTACAGCTCGTCCATGCC Vector Fw: GTACAAGTAATCGAGCTAGCATATGGATCCATATAACT Vector Rev: CATGGTGGTGCCCAGTGCCTCACGACC	This study
pAT4251	KIF22-GFP R149Q	Fw: GGGGTGATCCCGCAGGCTCTCATGGAC Rev: GTCCATGAGAGCCTGCGGGATCACCCC	This study
pAT4258	KIF22-GFP V475G	Fw: TGCTAATGAAGACAGGAGAAGAGAAGGACCT Rev: AGGTCCTTCTCTTCTCCTGTCTTCATTAGCA	This study
pAT4260	KIF22-GFP T463D	Fw: CCCCTCTGTTGAGTGACCCAAAGCGAGAGC Rev: GCTCTCGCTTTGGGTCACTCAACAGAGGGG	This study
pAT4261	KIF22-GFP T463A	Fw: CCTCTGTTGAGTGCCCCAAAGCGAG Rev: CTCGCTTTGGGGCACTCAACAGAGG	This study
pAT4264	KIF22-GFP R149L	Fw: GGGTGATCCCGCTGGCTCTCATGGAC Rev: GTCCATGAGAGCCAGCGGGATCACCC	This study
pAT4269	KIF22-GFP P148L	Fw: CCTGGGGTGATCCTGCGGGCTCTCATG Rev: CATGAGAGCCCGCAGGATCACCCCAGG	This study
pAT4270	KIF22-GFP P148S	Fw: CTGGGGTGATCTCGCGGGCTCTCATG Rev: CATGAGAGCCCGCGAGATCACCCCAG	This study
pSS4279	KIF22-GFP T134A	Fragment Fw: AGCTGCTCACTCGAAATCGC Fragment Rev: AGTCTTTCTCGGATTACCAGG Vector Fw: CCTGGTAATCCGAGAAGACT Vector Rev: GCGATTTCGAGTGAGCAGCT	This study
pSS4281	KIF22-GFP T134D	Fw: CAGGAGCTGGGAAGGATCACACAATGCTGGGC Rev: GCCCAGCATTGTGTGATCCTTCCCAGCTCCTG	This study
pNA4285	KIF22-GFP T158A	Fw: AGCTCGCAAGGGAGGAGGGTG Rev: GAGTACCTGGAGGACGTCGA	This study
pNA4284	KIF22-GFP T158D	Fw: CCTCCTGCAGCTCAGGGAGGAGGGTG Rev: CACCCTCCTCCCTGAGCTGCAGGAGG	This study

1268 **ACKNOWLEDGEMENTS**

1269 This work was supported by NIH F31AR074887 to AFT, NIH R01GM130556 to JKS, NIH
1270 R01GM121491 to JKS, and the Ballenger Ventures Fund for Research Excellence. We thank the
1271 Mayo Clinic Center for Individualized Medicine (CIM) for supporting this research through the CIM
1272 Investigative and Functional Genomics program. We thank Alan Howe for the mCh-CAAX
1273 plasmid, and Ryoma Ohi for reagents and acceptor cells for recombination-mediated cassette
1274 exchange. We thank Rachel Stadler for technical assistance with data analysis and thank Laura
1275 Reinholdt and Matthew Warman for constructive discussions regarding this work.

1276

1277 **COMPETING INTERESTS**

1278 The authors declare no competing financial interests.

1279

1280 **VIDEO LEGENDS**

1281 **Video 1. Fluorescence recovery after photobleaching of KIF22-GFP.**

1282 Fluorescence recovery after photobleaching (FRAP) in HeLa-Kyoto cells expressing KIF22-GFP
1283 (top), KIF22-GFP R149Q (middle), or KIF22-GFP V475G (bottom). Cells represent interphase
1284 (left), metaphase (middle), or anaphase (right). Bleaching occurred at time zero. Scale bar 10 μm.
1285 Cells were imaged at 5 second intervals for 25 seconds before bleaching, photobleached, and
1286 imaged at 20 second intervals for 10 minutes after bleaching. Playback at 10 frames per second.

1287

1288 **Video 2. Anaphase in HeLa-Kyoto cells.**

1289 Anaphase chromosome segregation in HeLa-Kyoto cells expressing KIF22-GFP (left), KIF22-
1290 GFP R149Q (middle), or KIF22-GFP V475G (right). Magenta: SiR-Tubulin, green: KIF22-GFP.
1291 Times indicate minutes after anaphase onset. Scale bar 5 μm. Cells were imaged at 1 minute
1292 intervals. Playback at 10 frames per second (600X real time).

1293

1294 **Video 3. Anaphase in RPE-1 cells.**

1295 Anaphase chromosome segregation in RPE-1 cells expressing KIF22-GFP (left), KIF22-GFP
1296 R149Q (middle), or KIF22-GFP V475G (right). Magenta: SiR-Tubulin, green: KIF22-GFP. Times
1297 indicate minutes after anaphase onset. Scale bar 5 μm. Cells were imaged at 1 minute intervals.
1298 Playback at 10 frames per second (600X real time).

1299

1300 **Video 4. Anaphase spindle pole separation.**

1301 Anaphase in HeLa-Kyoto cells expressing pericentrin-RFP (magenta), CENPB-mCh (magenta),
1302 and KIF22-GFP (cyan). Times indicate seconds after anaphase onset. Scale bar 5 μm. Cells were
1303 imaged at 20 second intervals. Playback at 15 frames per second (300X real time).
1304
1305 **Video 5. Cytokinesis and cytokinesis failure.**
1306 Mitosis and cytokinesis in HeLa-Kyoto cells expressing KIF22-GFP (left), KIF22-GFP R149Q
1307 (middle), or KIF22-GFP V475G (right) (all KIF22-GFP represented in green) and mCh-CAAX
1308 (magenta). Scale bar 10 μm. Cells were imaged at 3 minute intervals. Playback at 25 frames per
1309 second (4500X real time).
1310
1311 **REFERENCES**

1312 Adzhubei, I. A., Schmidt, S., Peshkin, L., Ramensky, V. E., Gerasimova, A., Bork, P., et al.
1313 (2010). A method and server for predicting damaging missense mutations. *Nature Methods*,
1314 *7*(4), 248–249. http://doi.org/10.1038/nmeth0410-248
1315 Antonio, C., Ferby, I., Wilhelm, H., Jones, M., Karsenti, E., Nebreda, A. R., & Vernos, I. (2000).
1316 Xkid, a chromokinesin required for chromosome alignment on the metaphase plate. *Cell*,
1317 *102*(4), 425–435. http://doi.org/10.1016/s0092-8674(00)00048-9
1318 Asbury, C. L. (2017). Anaphase A: Disassembling Microtubules Move Chromosomes toward
1319 Spindle Poles. *Biology*, *6*(1), 15. http://doi.org/10.3390/biology6010015
1320 Asselin, L., Alvarez, J. R., Heide, S., Bonnet, C. S., Tilly, P., Vitet, H., et al. (2020). Mutations in
1321 the KIF21B kinesin gene cause neurodevelopmental disorders through imbalanced
1322 canonical motor activity. *Nature Communications*, 1–18. http://doi.org/10.1038/s41467-020-
1323 16294-6
1324 Bianchi, S., van Riel, W. E., Kraatz, S. H. W., Olieric, N., Frey, D., Katrukha, E. A., et al. (2016).
1325 Structural basis for misregulation of kinesin KIF21A autoinhibition by CFEOM1 disease
1326 mutations. *Scientific Reports*, *6*(1), 30668–16. http://doi.org/10.1038/srep30668
1327 Bickel, K. G., Mann, B. J., Waitzman, J. S., Poor, T. A., Rice, S. E., & Wadsworth, P. (2017). Src
1328 family kinase phosphorylation of the motor domain of the human kinesin-5, Eg5.
1329 *Cytoskeleton (Hoboken, N.J.)*, *74*(9), 317–330. http://doi.org/10.1002/cm.21380
1330 Bieling, P., Kronja, I., & Surrey, T. (2010). Microtubule Motility on Reconstituted Meiotic
1331 Chromatin. *Current Biology*, *20*(8), 763–769. http://doi.org/10.1016/j.cub.2010.02.067
1332 Blasius, T. L., Yue, Y., Prasad, R., Liu, X., Gennerich, A., & Verhey, K. J. (2021). Sequences in
1333 the stalk domain regulate auto-inhibition and ciliary tip localization of the immotile kinesin-4
1334 KIF7. *Journal of Cell Science*, *134*(13). http://doi.org/10.1242/jcs.258464
1335 Bodnar, A. G., Ouellette, M., Frolkis, M., Holt, S. E., Chiu, C. P., Morin, G. B., et al. (1998).
1336 Extension of life-span by introduction of telomerase into normal human cells. *Science (New*
1337 *York, N.Y.)*, *279*(5349), 349–352. http://doi.org/10.1126/science.279.5349.349
1338 Boyden, E. D., Campos-Xavier, A. B., Kalamajski, S., Cameron, T. L., Suarez, P., Tanackovic,
1339 G., et al. (2011). Recurrent dominant mutations affecting two adjacent residues in the motor
1340 domain of the monomeric kinesin KIF22 result in skeletal dysplasia and joint laxity.
1341 *American Journal of Human Genetics*, *89*(6), 767–772.
1342 http://doi.org/10.1016/j.ajhg.2011.10.016
1343 Brouhard, G. J., & Hunt, A. J. (2005). Microtubule movements on the arms of mitotic
1344 chromosomes: polar ejection forces quantified in vitro. *Proceedings of the National*
1345 *Academy of Sciences*, *102*(39), 13903–13908. http://doi.org/10.1073/pnas.0506017102

Brust-Mascher, I., Civelekoglu-Scholey, G., Kwon, M., Mogilner, A., & Scholey, J. M. (2004). Model for anaphase B: role of three mitotic motors in a switch from poleward flux to spindle elongation. *Proceedings of the National Academy of Sciences*, *101*(45), 15938–15943. http://doi.org/10.1073/pnas.0407044101

Cameron, L. A., Yang, G., Cimini, D., Canman, J. C., Kisurina-Evgenieva, O., Khodjakov, A., et al. (2006). Kinesin 5-independent poleward flux of kinetochore microtubules in PtK1 cells. *The Journal of Cell Biology*, *173*(2), 173–179. http://doi.org/10.1083/jcb.200601075

Cassimeris, L., Rieder, C. L., & Salmon, E. D. (1994). Microtubule Assembly and Kinetochore Directional Instability in Vertebrate Monopolar Spindles - Implications for the Mechanism of Chromosome Congression. *Journal of Cell Science*, *107*, 285–297.

Cheng, L., Desai, J., Miranda, C. J., Duncan, J. S., Qiu, W., Nugent, A. A., et al. (2014). Human CFEOM1 Mutations Attenuate KIF21A Autoinhibition and Cause Oculomotor Axon Stalling. *Neuron*, *82*(2), 334–349. http://doi.org/10.1016/j.neuron.2014.02.038

Chiba, K., Ori-McKenney, K. M., Niwa, S., & McKenney, R. J. (2021). Reconstitution of Kinesin-1 Activation. *Biorxiv.org*. http://doi.org/10.1101/2021.03.12.434960

Choudhary, C., Kumar, C., Gnad, F., Nielsen, M. L., Rehman, M., Walther, T. C., et al. (2009). Lysine acetylation targets protein complexes and co-regulates major cellular functions. *Science (New York, N.Y.)*, *325*(5942), 834–840. http://doi.org/10.1126/science.1175371

Cimini, D., Cameron, L. A., & Salmon, E. D. (2004). Anaphase spindle mechanics prevent mis-segregation of merotelically oriented chromosomes. *Current Biology*, *14*(23), 2149–2155. http://doi.org/10.1016/j.cub.2004.11.029

Civelekoglu-Scholey, G., He, B., Shen, M., Wan, X., Roscioli, E., Bowden, B., & Cimini, D. (2013). Dynamic bonds and polar ejection force distribution explain kinetochore oscillations in PtK1 cells. *The Journal of Cell Biology*, *201*(4), 577–593. http://doi.org/10.1083/jcb.201301022

Cousin, M. A., Conboy, E., Wang, J.-S., Lenz, D., Schwab, T. L., Williams, M., et al. (2019). RINT1 Bi-allelic Variations Cause Infantile-Onset Recurrent Acute Liver Failure and Skeletal Abnormalities. *American Journal of Human Genetics*, *105*(1), 108–121. http://doi.org/10.1016/j.ajhg.2019.05.011

Coy, D. L., Hancock, W. O., Wagenbach, M., & Howard, J. (1999). Kinesin's tail domain is an inhibitory regulator of the motor domain. *Nature Cell Biology*, *1*(5), 288–292. http://doi.org/10.1038/13001

Dephoure, N., Zhou, C., Villén, J., Beausoleil, S. A., Bakalarski, C. E., Elledge, S. J., & Gygi, S. P. (2008). A quantitative atlas of mitotic phosphorylation. *Proceedings of the National Academy of Sciences of the United States of America*, *105*(31), 10762–10767. http://doi.org/10.1073/pnas.0805139105

Dodds, G. S. (1930). Row formation and other types of arrangement of cartilage cells in endochondral ossification. *The Anatomical Record*, *46*(4), 385–399. http://doi.org/10.1002/ar.1090460409

Espeut, J., Gaussen, A., Bieling, P., Morin, V., Prieto, S., Fesquet, D., et al. (2008). Phosphorylation Relieves Autoinhibition of the Kinetochore Motor Cenp-E. *Molecular Cell*, *29*(5), 637–643. http://doi.org/10.1016/j.molcel.2008.01.004

Friedman, D. S., & Vale, R. D. (1999). Single-molecule analysis of kinesin motility reveals regulation by the cargo-binding tail domain. *Nature Cell Biology*, *1*(5), 293–297. http://doi.org/10.1038/13008

Fu, C., Ward, J. J., Loiodice, I., Velve-Casquillas, G., Nedelec, F. J., & Tran, P. T. (2009). Phospho-Regulated Interaction between Kinesin-6 Klp9p and Microtubule Bundler Ase1p Promotes Spindle Elongation. *Developmental Cell*, *17*(2), 257–267. http://doi.org/10.1016/j.devcel.2009.06.012

Funabiki, H., & Murray, A. W. (2000). The Xenopus chromokinesin Xkid is essential for metaphase chromosome alignment and must be degraded to allow anaphase chromosome movement. *Cell*, *102*(4), 411–424.

Gan, H., Xue, W., Gao, Y., Zhu, G., Chan, D., Cheah, K. S. E., & Huang, J. (2019). KIF5B modulates central spindle organization in late-stage cytokinesis in chondrocytes. *Cell & Bioscience*, 1–16. http://doi.org/10.1186/s13578-019-0344-5

Gillingham, A. K., & Munro, S. (2000). The PACT domain, a conserved centrosomal targeting motif in the coiled-coil proteins AKAP450 and pericentrin. *EMBO Reports*, *1*(6), 524–529. http://doi.org/10.1093/embo-reports/kvd105

Haila, S., Hästbacka, J., Böhling, T., Karjalainen-Lindsberg, M. L., Kere, J., & Saarialho-Kere, U. (2001). SLC26A2 (diastrophic dysplasia sulfate transporter) is expressed in developing and mature cartilage but also in other tissues and cell types. *The Journal of Histochemistry and Cytochemistry : Official Journal of the Histochemistry Society*, *49*(8), 973–982. http://doi.org/10.1177/002215540104900805

Hammond, J. W., Blasius, T. L., Soppina, V., Cai, D., & Verhey, K. J. (2010). Autoinhibition of the kinesin-2 motor KIF17 via dual intramolecular mechanisms. *The Journal of Cell Biology*, *189*(6), 1013–1025. http://doi.org/10.1083/jcb.201001057

Hammond, J. W., Cai, D., Blasius, T. L., Li, Z., Jiang, Y., Jih, G. T., et al. (2009). Mammalian Kinesin-3 Motors Are Dimeric In Vivo and Move by Processive Motility upon Release of Autoinhibition. *PLOS Biology*, *7*(3), e1000072–14. http://doi.org/10.1371/journal.pbio.1000072

Hatch, E. M., Fischer, A. H., Deerinck, T. J., & Hetzer, M. W. (2013). Catastrophic Nuclear Envelope Collapse in Cancer Cell Micronuclei. *Cell*, *154*(1), 47–60. http://doi.org/10.1016/j.cell.2013.06.007

Hegemann, B., Hutchins, J. R. A., Hudecz, O., Novatchkova, M., Rameseder, J., Sykora, M. M., et al. (2011). Systematic phosphorylation analysis of human mitotic protein complexes. *Science Signaling*, *4*(198), rs12. http://doi.org/10.1126/scisignal.2001993

Hershko, A. (1999). Mechanisms and regulation of the degradation of cyclin B. *Philosophical Transactions of the Royal Society of London. Series B, Biological Sciences*, *354*(1389), 1571–5– discussion 1575–6. http://doi.org/10.1098/rstb.1999.0500

Iemura, K., & Tanaka, K. (2015). Chromokinesin Kid and kinetochore kinesin CENP-E differentially support chromosome congression without end-on attachment to microtubules. *Nature Communications*, *6*, 1–11. http://doi.org/10.1038/ncomms7447

Imanishi, M., Endres, N. F., Gennerich, A., & Vale, R. D. (2006). Autoinhibition regulates the motility of the C. elegans intraflagellar transport motor OSM-3. *The Journal of Cell Biology*, *174*(7), 931–937. http://doi.org/10.1083/jcb.200605179

Ioannidis, N. M., Rothstein, J. H., Pejaver, V., Middha, S., McDonnell, S. K., Baheti, S., et al. (2016). REVEL: An Ensemble Method for Predicting the Pathogenicity of Rare Missense Variants. *The American Journal of Human Genetics*, *99*(4), 877–885. http://doi.org/10.1016/j.ajhg.2016.08.016

Kettenbach, A. N., Schweppe, D. K., Faherty, B. K., Pechenick, D., Pletnev, A. A., & Gerber, S. A. (2011). Quantitative phosphoproteomics identifies substrates and functional modules of Aurora and Polo-like kinase activities in mitotic cells. *Science Signaling*, *4*(179), rs5. http://doi.org/10.1126/scisignal.2001497

Khandelia, P., Yap, K., & Makeyev, E. V. (2011). Streamlined platform for short hairpin RNA interference and transgenesis in cultured mammalian cells. *Proceedings of the National Academy of Sciences of the United States of America*, *108*(31), 12799–12804. http://doi.org/10.1073/pnas.1103532108

Lefeber, D. J., Morava, E., & Jaeken, J. (2011). How to find and diagnose a CDG due to defective N-glycosylation. *Journal of Inherited Metabolic Disease*, *34*(4), 849–852. http://doi.org/10.1007/s10545-011-9370-0

Levesque, A. A., & Compton, D. A. (2001). The chromokinesin Kid is necessary for chromosome arm orientation and oscillation, but not congression, on mitotic spindles. *The Journal of Cell Biology*, *154*(6), 1135–1146. http://doi.org/10.1083/jcb.200106093

Levesque, A. A., Howard, L., Gordon, M. B., & Compton, D. A. (2003). A functional relationship between NuMA and kid is involved in both spindle organization and chromosome alignment in vertebrate cells. *Molecular Biology of the Cell*, *14*(9), 3541–3552. http://doi.org/10.1091/mbc.E03-02-0082

Liu, D., Vleugel, M., Backer, C. B., Hori, T., Fukagawa, T., Cheeseman, I. M., & Lampson, M. A. (2010). Regulated targeting of protein phosphatase 1 to the outer kinetochore by KNL1 opposes Aurora B kinase. *The Journal of Cell Biology*, *188*(6), 809–820. http://doi.org/10.1083/jcb.201001006

Liu, Y., Mi, Y., Mueller, T., Kreibich, S., Williams, E. G., Van Drogen, A., et al. (2018). Genomic, Proteomic and Phenotypic Heterogeneity in HeLa Cells across Laboratories: Implications for Reproducibility of Research Results. *bioRxiv*, 307421. http://doi.org/10.1101/307421

Marquis, C., Fonseca, C. L., Queen, K. A., Wood, L., Vandal, S. E., Malaby, H. L. H., et al. (2021). Chromosomally unstable tumor cells specifically require KIF18A for proliferation. *Nature Communications*, 1–14. http://doi.org/10.1038/s41467-021-21447-2

Marshall, W. F., Marko, J. F., Agard, D. A., & Sedat, J. W. (2001). Chromosome elasticity and mitotic polar ejection force measured in living Drosophila embryos by four-dimensional microscopy-based motion analysis. *Current Biology*, *11*(8), 569–578. http://doi.org/10.1016/s0960-9822(01)00180-4

Min, B.-J., Kim, N., Chung, T., Kim, O.-H., Nishimura, G., Chung, C. Y., et al. (2011). Whole-exome sequencing identifies mutations of KIF22 in spondyloepimetaphyseal dysplasia with joint laxity, leptodactylic type. *American Journal of Human Genetics*, *89*(6), 760–766. http://doi.org/10.1016/j.ajhg.2011.10.015

Morgan, D. O. (1995). Principles of CDK regulation. *Nature*, *374*(6518), 131–134. http://doi.org/10.1038/374131a0

Muretta, J. M., Reddy, B. J. N., Scarabelli, G., Thompson, A. F., Jariwala, S., Major, J., et al. (2018). A posttranslational modification of the mitotic kinesin Eg5 that enhances its mechanochemical coupling and alters its mitotic function. *Proceedings of the National Academy of Sciences*, *74*, 201718290–10. http://doi.org/10.1073/pnas.1718290115

Nislow, C., Lombillo, V. A., Kuriyama, R., & McIntosh, J. R. (1992). A plus-end-directed motor enzyme that moves antiparallel microtubules in vitro localizes to the interzone of mitotic spindles. *Nature*, *359*(6395), 543–547. http://doi.org/10.1038/359543a0

Ohsugi, M., Adachi, K., Horai, R., Kakuta, S., Sudo, K., Kotaki, H., et al. (2008). Kid-Mediated Chromosome Compaction Ensures Proper Nuclear Envelope Formation. *Cell*, *132*(5), 771–782. http://doi.org/10.1016/j.cell.2008.01.029

Ohsugi, M., Tokai-Nishizumi, N., Shiroguchi, K., Toyoshima, Y. Y., Inoue, J.-I., & Yamamoto, T. (2003). Cdc2-mediated phosphorylation of Kid controls its distribution to spindle and chromosomes. *The EMBO Journal*, *22*(9), 2091–2103. http://doi.org/10.1093/emboj/cdg208

Olsen, J. V., Vermeulen, M., Santamaria, A., Kumar, C., Miller, M. L., Jensen, L. J., et al. (2010). Quantitative phosphoproteomics reveals widespread full phosphorylation site occupancy during mitosis. *Science Signaling*, *3*(104), ra3. http://doi.org/10.1126/scisignal.2000475

Pant, D., Parameswaran, J., Rao, L., Shi, L., Chilukuri, G., McEachin, Z. T., et al. (2022). ALS-linked KIF5A ΔExon27 mutant causes neuronal toxicity through gain of function. *Biorxiv.org* . http://doi.org/10.1101/2022.03.05.483071

Quang, D., Chen, Y., & Xie, X. (2015). DANN: a deep learning approach for annotating the pathogenicity of genetic variants. *Bioinformatics (Oxford, England)*, *31*(5), 761–763. http://doi.org/10.1093/bioinformatics/btu703

Ren, J., Wang, S., Chen, H., Wang, W., Huo, L., & Feng, W. (2018). Coiled-coil 1-mediated fastening of the neck and motor domains for kinesin-3 autoinhibition. *Proceedings of the National Academy of Sciences of the United States of America*, *115*(51), E11933–E11942. http://doi.org/10.1073/pnas.1811209115

Rentzsch, P., Witten, D., Cooper, G. M., Shendure, J., & Kircher, M. (2018). CADD: predicting the deleteriousness of variants throughout the human genome, 1–9. http://doi.org/10.1093/nar/gky1016

Rieder, C. L., & Salmon, E. D. (1994). Motile kinetochores and polar ejection forces dictate chromosome position on the vertebrate mitotic spindle. *The Journal of Cell Biology*, *124*(3), 223–233. http://doi.org/10.1083/jcb.124.3.223

Rieder, C. L., Davison, E. A., Jensen, L. C., Cassimeris, L., & Salmon, E. D. (1986). Oscillatory movements of monooriented chromosomes and their position relative to the spindle pole result from the ejection properties of the aster and half-spindle. *The Journal of Cell Biology*, *103*(2), 581–591. http://doi.org/10.1083/jcb.103.2.581

Rigbolt, K. T. G., Prokhorova, T. A., Akimov, V., Henningsen, J., Johansen, P. T., Kratchmarova, I., et al. (2011). System-wide temporal characterization of the proteome and phosphoproteome of human embryonic stem cell differentiation. *Science Signaling*, *4*(164), rs3. http://doi.org/10.1126/scisignal.2001570

Ris, H. (1949). The anaphase movement of chromosomes in the spermatocytes of the grasshopper. *The Biological Bulletin*, *96*(1), 90–106.

Rossi, A., & Superti-Furga, A. (2001). Mutations in the diastrophic dysplasia sulfate transporter (DTDST) gene (SLC26A2): 22 novel mutations, mutation review, associated skeletal phenotypes, and diagnostic relevance. *Human Mutation*, *17*(3), 159–171. http://doi.org/10.1002/humu.1

Samwer, M., Schneider, M. W. G., Hoefler, R., Schmalhorst, P. S., Jude, J. G., Zuber, J., & Gerlich, D. W. (2017). DNA Cross-Bridging Shapes a Single Nucleus from a Set of Mitotic Chromosomes. *Cell*, *170*(5), 956–972.e23. http://doi.org/10.1016/j.cell.2017.07.038

Sawin, K. E., LeGuellec, K., Philippe, M., & Mitchison, T. J. (1992). Mitotic spindle organization by a plus-end-directed microtubule motor. *Nature*, *359*(6395), 540–543. http://doi.org/10.1038/359540a0

Schindelin, J., Arganda-Carreras, I., Frise, E., Kaynig, V., Longair, M., Pietzsch, T., et al. (2012). Fiji: an open-source platform for biological-image analysis. *Nature Methods*, *9*(7), 676–682. http://doi.org/10.1038/nmeth.2019

Schneider, C. A., Rasband, W. S., & Eliceiri, K. W. (2012). NIH Image to ImageJ: 25 years of image analysis. *Nature Methods*, 1–5. http://doi.org/10.1038/nmeth.2089

Schwarz, J. M., Rödelsperger, C., Schuelke, M., & Seelow, D. (2010). MutationTaster evaluates disease-causing potential of sequence alterations. *Nature Publishing Group*, 1–2. http://doi.org/10.1038/nmeth0810-575

Serra-Marques, A., Houtekamer, R., Hintzen, D., Canty, J. T., Yildiz, A., & Dumont, S. (2020). The mitotic protein NuMA plays a spindle-independent role in nuclear formation and mechanics. *The Journal of Cell Biology*, *219*(12), 348–23. http://doi.org/10.1083/jcb.202004202

Sharma, K., D'Souza, R. C. J., Tyanova, S., Schaab, C., Wisniewski, J. R., Cox, J., & Mann, M. (2014). Ultradeep Human Phosphoproteome Reveals a Distinct Regulatory Nature of Tyr and Ser/Thr-Based Signaling. *Cell Reports*, *8*(5), 1583–1594. http://doi.org/10.1016/j.celrep.2014.07.036

Shiroguchi, K., Ohsugi, M., Edamatsu, M., Yamamoto, T., & Toyoshima, Y. Y. (2003). The Second Microtubule-binding Site of Monomeric Kid Enhances the Microtubule Affinity. *The Journal of Biological Chemistry*, *278*(25), 22460–22465. http://doi.org/10.1074/jbc.M212274200

Shiromizu, T., Adachi, J., Watanabe, S., Murakami, T., Kuga, T., Muraoka, S., & Tomonaga, T. (2013). Identification of missing proteins in the neXtProt database and unregistered phosphopeptides in the PhosphoSitePlus database as part of the Chromosome-centric Human Proteome Project. *Journal of Proteome Research*, *12*(6), 2414–2421. http://doi.org/10.1021/pr300825v

Soeda, S., Yamada-Nomoto, K., & Ohsugi, M. (2016). The microtubule-binding and coiled-coil domains of Kid are required to turn off the polar ejection force at anaphase. *Journal of Cell Science*, *129*(19), 3609–3619. http://doi.org/10.1242/jcs.189969

Straight, A. F., Sedat, J. W., & Murray, A. W. (1998). Time-lapse microscopy reveals unique roles for kinesins during anaphase in budding yeast. *The Journal of Cell Biology*, *143*(3), 687–694. http://doi.org/10.1083/jcb.143.3.687

Stumpff, J., Dassow, von, G., Wagenbach, M., Asbury, C., & Wordeman, L. (2008). The Kinesin-8 Motor Kif18A Suppresses Kinetochore Movements to Control Mitotic Chromosome Alignment. *Developmental Cell*, *14*(2), 252–262. http://doi.org/10.1016/j.devcel.2007.11.014

Stumpff, J., Wagenbach, M., Franck, A., Asbury, C. L., & Wordeman, L. (2012). Kif18A and Chromokinesins Confine Centromere Movements via Microtubule Growth Suppression and Spatial Control of Kinetochore Tension. *Developmental Cell*, *22*(5), 1017–1029. http://doi.org/10.1016/j.devcel.2012.02.013

Sturgill, E. G., Norris, S. R., Guo, Y., & Ohi, R. (2016). Kinesin-5 inhibitor resistance is driven by kinesin-12. *The Journal of Cell Biology*, *213*(2), 213–227. http://doi.org/10.1083/jcb.201507036

Su, K.-C., Barry, Z., Schweizer, N., Maiato, H., Bathe, M., & Cheeseman, I. M. (2016). A Regulatory Switch Alters Chromosome Motions at the Metaphase-to-Anaphase Transition. *Cell Reports*, *17*(7), 1728–1738. http://doi.org/10.1016/j.celrep.2016.10.046

Takagi, J., Itabashi, T., Suzuki, K., & Ishiwata, S. (2013). Chromosome position at the spindle equator is regulated by chromokinesin and a bipolar microtubule array. *Scientific Reports*, *3*, 746–7. http://doi.org/10.1038/srep02808

Tanenbaum, M. E., Macůrek, L., Janssen, A., Geers, E. F., Alvarez-Fernández, M., & Medema, R. H. (2009). Kif15 Cooperates with Eg5 to Promote Bipolar Spindle Assembly. *Current Biology*, *19*(20), 1703–1711. http://doi.org/10.1016/j.cub.2009.08.027

Thompson, A. F., Vandal, S., & Stumpff, J. (2022). Quantifying Changes in Chromosome Position to Assess Chromokinesin Activity. *Methods in Molecular Biology (Clifton, N.J.)*, *2415*, 139–149. http://doi.org/10.1007/978-1-0716-1904-9_10

Tokai, N., Fujimoto-Nishiyama, A., Toyoshima, Y., Yonemura, S., Tsukita, S., Inoue, J., & Yamamoto, T. (1996). Kid, a novel kinesin-like DNA binding protein, is localized to chromosomes and the mitotic spindle. *The EMBO Journal*, *15*(3), 457–467.

Tokai-Nishizumi, N., Ohsugi, M., Suzuki, E., & Yamamoto, T. (2005). The chromokinesin kid is required for maintenance of proper metaphase spindle size. *Molecular Biology of the Cell*, *16*(11), 5455–5463. http://doi.org/10.1091/mbc.E05-03-0244

Tüysüz, B., Yılmaz, S., Erener-Ercan, T., Bilguvar, K., & Günel, M. (2014). Spondyloepimetaphyseal dysplasia with joint laxity, leptodactylic type: longitudinal observation of radiographic findings in a child heterozygous for a KIF22 mutation. *Pediatric Radiology*, *45*(5), 771–776. http://doi.org/10.1007/s00247-014-3159-x

Uhlen, M., Fagerberg, L., Hallström, B. M., Lindskog, C., Oksvold, P., Mardinoglu, A., et al. (2015). Tissue-based map of the human proteome. *Science (New York, N.Y.)*, *347*(6220), 1260419–1260419. http://doi.org/10.1126/science.1260419

van der Vaart, B., van Riel, W. E., Doodhi, H., Kevenaar, J. T., Katrukha, E. A., Gumy, L., et al. (2013). CFEOM1-Associated Kinesin KIF21A Is a Cortical Microtubule Growth Inhibitor. *Developmental Cell*, *27*(2), 145–160. http://doi.org/10.1016/j.devcel.2013.09.010

van Heesbeen, R. G. H. P., Tanenbaum, M. E., & Medema, R. H. (2014). Balanced Activity of Three Mitotic Motors Is Required for Bipolar Spindle Assembly and Chromosome Segregation. *Cell Reports*, *8*(4), 948–956. http://doi.org/10.1016/j.celrep.2014.07.015

Vaser, R., Adusumalli, S., Leng, S. N., Sikic, M., & Ng, P. C. (2015). SIFT missense predictions for genomes. *Nature Protocols*, *11*(1), 1–9. http://doi.org/10.1038/nprot.2015-123

Verhey, K. J., & Hammond, J. W. (2009). Cytoskeletal motors: Traffic control: regulation of kinesin motors, 1–13. http://doi.org/10.1038/nrm2782

Verhey, K. J., Lizotte, D. L., Abramson, T., Barenboim, L., Schnapp, B. J., & Rapoport, T. A. (1998). Light chain-dependent regulation of Kinesin's interaction with microtubules. *The Journal of Cell Biology*, *143*(4), 1053–1066. http://doi.org/10.1083/jcb.143.4.1053

Vukušić, K., Buđa, R., & Tolić, I. M. (2019). Force-generating mechanisms of anaphase in human cells. *Journal of Cell Science*, *132*(18), jcs231985–11. http://doi.org/10.1242/jcs.231985

Vukušić, K., Ponjavić, I., Buđa, R., Risteski, P., & Tolić, I. M. (2021). Microtubule-sliding modules based on kinesins EG5 and PRC1-dependent KIF4A drive human spindle elongation. *Developmental Cell*, 1–42. http://doi.org/10.1016/j.devcel.2021.04.005

Wandke, C., Barisic, M., Sigl, R., Rauch, V., Wolf, F., Amaro, A. C., et al. (2012). Human chromokinesins promote chromosome congression and spindle microtubule dynamics during mitosis. *The Journal of Cell Biology*, *198*(5), 847–863. http://doi.org/10.1083/jcb.201110060

Wolf, F., Wandke, C., Isenberg, N., & Geley, S. (2006). Dose-dependent effects of stable cyclin B1 on progression through mitosis in human cells. *The EMBO Journal*, *25*(12), 2802–2813. http://doi.org/10.1038/sj.emboj.7601163

Yajima, J., Edamatsu, M., Watai-Nishii, J., Tokai-Nishizumi, N., Yamamoto, T., & Toyoshima, Y. Y. (2003). The human chromokinesin Kid is a plus end-directed microtubule-based motor. *The EMBO Journal*, *22*(5), 1067–1074. http://doi.org/10.1093/emboj/cdg102

Zhang, P., Knowles, B. A., Goldstein, L. S., & Hawley, R. S. (1990). A kinesin-like protein required for distributive chromosome segregation in Drosophila. *Cell*, *62*(6), 1053–1062.